Probing and Preparing Novel States of Quantum Degenerate Rubidium Atoms in Optical Lattices

by

Hirokazu Miyake

Submitted to the Department of Physics
in partial fulfillment of the requirements for the degree of

Doctor of Philosophy

at the

MASSACHUSETTS INSTITUTE OF TECHNOLOGY

June 2013

Author . . . .
Department of Physics
May 20, 2013

Certified by . . . .
Wolfgang Ketterle
John D. MacArthur Professor of Physics
Thesis Supervisor

Certified by . . . .
David E. Pritchard
Cecil and Ida Green Professor of Physics
Thesis Supervisor

Accepted by . . . .
John W. Belcher
Class of '22 Professor of Physics
Associate Department Head for Education

Probing and Preparing Novel States of Quantum Degenerate Rubidium Atoms in Optical Lattices

by

Hirokazu Miyake

Submitted to the Department of Physics
on May 20, 2013, in partial fulfillment of the
requirements for the degree of
Doctor of Philosophy

Abstract

Ultracold atoms in optical lattices are promising systems to realize and study novel quantum mechanical phases of matter with the control and precision offered by atomic physics. Towards this goal, as important as engineering new states of matter is the need to develop new techniques to probe these systems.

I first describe our work on realizing Bragg scattering of infrared light from ultracold atoms in optical lattices. This is a detection technique which probes the spatial ordering of a crystalline system, and has led to our observation of Heisenberg-limited wavefunction dynamics. Furthermore, we have observed the superfluid to Mott insulator transition through the matter wave Talbot effect. This technique will be particularly powerful for studying antiferromagnetic phases of matter due to its sensitivity to the crystalline composition.

The second major component of this thesis describes a new scheme to realize the Harper Hamiltonian. The Harper Hamiltonian is a model system which effectively describes electrons in a solid immersed in a very high magnetic field. The effective magnetic field manifests itself as a position-dependent phase in the motion of the constituent particles, which can be related to gauge fields and has strong connections to topological properties of materials. We describe how we can engineer the Harper Hamiltonian in a two-dimensional optical lattice with neutral atoms by creating a linear potential tilt and inducing Raman transitions between localized states. *In situ* measurements provide evidence that we have successfully created the Harper Hamiltonian, but further evidence is needed to confirm the creation of the ground state of this Hamiltonian.

Thesis Supervisor: Wolfgang Ketterle
Title: John D. MacArthur Professor of Physics

Thesis Supervisor: David E. Pritchard
Title: Cecil and Ida Green Professor of Physics

Acknowledgments

My time at MIT has been tremendously valuable for me, both professionally as well as personally. I reckon there are very few institutions in the world where one is surrounded by so many people with brilliant minds, unwavering passion for what they do, and the kindest of hearts.

First of all, I thank my Ph.D. supervisors Professor Wolfgang Ketterle and Professor Dave Pritchard for their support throughout my time at MIT. I am amazed by and grateful for the degree of trust Wolfgang put in me from day one to be successful in lab. The freedom he gave me to thrive in the laboratory has been a very valuable experience for me. His physical intuition and ability to make connections between seemingly disparate facts is something I have strived to achieve. Dave has supported me both as research supervisor in the early years of my Ph.D. as well as an academic advisor throughout. His deep insight into almost any issue that could be of interest to the human mind is quite amazing.

Laboratory work can be exhilarating, but if I am completely honest, I have to admit that there are no shortages of disappointments in running experiments, especially when one is trying to push back the frontiers of human knowledge. I would not have been able to get through to the end of my Ph.D. without the help I recieved from my collaborators in the BEC4 lab. They have been a constant source of encouragement and support through the ups and downs that is laboratory work. I have also had an enormous amount of fun with them, day and night, rain or shine. They are a major reason why my time at MIT has been a fantastic experience.

David Weld was the postdoc when I joined the group, and despite my repeated questions about basic things, whether it be about atoms, vacuum, or lasers, he patiently and clearly explained all the questions I would throw at him. His ability to get things done was very impressive. Without any complaining or whining, he would get down on his hands and knees to do whatever it takes to make progress in our experiment. His perseverance and calmness is something which I have tried to emulate. I am very fortunate to have had him as an immediate superior during the beginning

of my Ph.D. Also he was one of very few people I could talk to about my interest in aviation, and I hope to one day fly on a A380 and brag to him about it.

Patrick Medley was the senior graduate student when I joined the group. I can say that I have never met a person with such a fast mind. Despite differences in information processing speed between the two of us, we were able to form a very good friendship, and shared many interests. I have to say that playing old school video games with him was one of the highlights of my time at MIT. I do not think I had as much fun with somebody since way, way back. And then all the various episodes we watched were also good times. In particular, I am proud to have witnessed with him a historic event as it happened, which was the end of 'Endless Eight.' Late nights in lab were made bearable by all that Patrick had to offer.

Georgios Siviloglou was the second postdoc that I interacted with, and he joined about midway through my Ph.D. We immediately became good friends. His understanding of and appreciation for the big picture, both in research and in life provided a lot of food for thought. In particular I was very impressed by his understanding and mastery of 'social engineering' and I am sure his influence shows through in the writing of this thesis. I will remember our stroll through the Toy District in Los Angeles at dusk as an interesting adventure. I will miss the coffee breaks at Area Four. I am looking forward to reading the Illiad upon graduation and hopefully I will have a chance to visit Mount Athos someday.

David Hucul was one year above me when I entered MIT. His command of electronics was nothing short of amazing to me, and his optimism and positive outlook helped to maintain good morale in the lab. I am also grateful to him for inviting me and my co-workers to my first ever commercial shoot, which was a fun experience. It taught me that I should work on my acting before I give it another try. Claire Leboutiller joined the BEC4 lab for a few months and worked on putting together Helmholtz coils for our science chamber. It was a pleasure working with her, and I admire her ability to get the job done with minimal supervision. Yichao Yu joined the BEC4 lab only when he was a sophomore, but his command of physics was evident from early on. His support on the Bragg results presented in this thesis was invaluable, and I am sure he will go on to do great things.

After I leave, Colin Kennedy will be the senior student on the BEC4 experiment. He is very lab smart, and only in a short time he has taken initiative numerous times and pushed forward many upgrades to our experiment for the better. With his willingness to take action, combined with his confidence, I am sure he will take the lab to new heights of success. Cody Burton is the youngest member in the BEC4 lab. Although he has been around for less than one year, it is clear that his calm and focus will be a valuable asset to the future operation of BEC4. I am looking forward to hearing great news from this lab as Colin and Cody 'take it to the next level.'

No acknowledgement will be complete without mentioning the other people in the Center for Ultracold Atoms. The collective knowledge they hold and the amount of supplies they provide in cases of emergencies have been an absolutely crucial part of our work. I am thankful for Christian Sanner for providing excellent technical help during the oddest hours, such as fixing puzzling problems with our magneic trap. Aviv Keshet is the unsung hero of the hallway, perhaps even the entire field of ultracold atoms. His Cicero experimental control program has provided us with a versatile and powerful platform to control our experiments and many other experiments throughout the world. Ed Su and I entered graduate school at the same time. His knowledge of ultracold atomic physics intimidated me at first, but he was also a great guy and his excitement for physics was contageous. Ralf Gommers had an excellent command of technical matters, and his soccer skills were also admirable. Jonathon Gillen deserves my thanks for reviewing our Bragg scattering paper before we sent it off for publication. I also appreciate him sharing his experience in the patent law field. Wujie Huang is a wonderfully nice person, and his insights about Raman-assisted tunneling helped to refine my understanding and helped make this thesis better. I want to thank Professor Martin Zwierlein for agreeing to serve on my thesis committee, as well as for his fighting spirit which kept the morale of our intramural soccer team high. Peyman Ahmadi deserves a profound thank you for many helpful technical discussions. His knowledge was truly valuable in solving our own problems, and he was always gracious with his time to help us. He was truly one of the kindest person in the hallway, in addition to being the greatest goal keeper the CUA has ever known. Cheng-Hsun Wu deserves my thanks for hosting me during the MIT Physics Department open house when I was choosing which graduate school to attend. Ivana Dimitrova, Niklas Jepsen and Jesse Amato-Grill also deserve a thank you for allowing us to borrow many of their equipments, and I am glad we shared an office for a brief time. Their joining the group definitely made the hallway a much more lively place. I appreciated the discussions I had with Haruka Tanji-Suzuki about our progress in graduate school and how every single time we talked, we could not belive so much time had elapsed since we talked last time. I thank all the people I met at conferences and summer schools, in particular at Les Houches in 2009. I will always remember the mountain hiking in the Alps, the breathtaking views, and that one pear in the lunch sack I ate after hiking for hours, which was the most delicious pear I ever had, or may ever have. I also want to thank everybody who played in the MIT intramural soccer team 'Balldrivers,' in particular Sebastian Hofferberth and Andrew Grier for helping me out as captain, and everybody who played in the CUA softball team against the JILA team at various DAMOP conferences. Joanna Keseberg deserves a profound thank you for all her help in dealing with administrative matters in a timely and professional way. She is what makes the CUA run as smoothly as it does.

There are also people outside of the lab which deserve special mention. Riccardo Abbate, Francesco D'Eramo and Thibault Peyronel have been good friends since the beginning of my time at MIT and we had fun times studying for our qualifying exams. I also want to thank Emily Florine, Michelle Sukup Jackson, Monica Sun and James Sun for fun times outside of physics during my first year here when I did not know too many people. Ariel Sommer and Matt Schram have been good roommates at Ashdown since the second year. I thank Steph Teo and Been Kim for good times in the later part of my studies. I want to thank Stephanie Houston for being a great pottery teacher. I also want to thank the students from all the seminar XL classes I have taught, as well as the staff at the Office of Minority Education for giving me the opportunity to teach undergraduates all throughout my time at MIT. I want to thank the wonderful friends I met at Cornell University who have continued to be good friends long after I have left Cornell, including Carol-Jean Wu, Linda Wu, Mark Wu, Jah Chaisangmongkon, Ava Wan, Joyce Lin, Thiti Taychatanapat, Will Cukierski, Jim Battista, Joe Calamia, Saúl Blanco Rodríguez and Nabil Iqbal.

I would also like to acknowledge the physicists I met during my undergraduate studies at Cornell University that convinced me to go to graduate school in physics. I am grateful to Professor Anders Ryd for taking me on as an undergraduate researcher during my sophomore year despite the fact that I knew nothing about research. He very patiently guided me through the research process of high energy experiments, in particular analysis of data from the CLEO-c detector located at Cornell University and helped me publish my first scientific paper. Needless to say, this gave me a lot of satisfaction and confidence in continuing in my physics research career. I had the good fortune of interacting with many knowledgeable and great people that were a part of the CLEO collaboration, and in particular I want to thank Werner Sun and Peter Onyisi for patiently guiding me through my data analysis. I am also grateful to Professor J. C. Séamus Davis for allowing me to join his research group. His very engaging lectures on introductory quantum mechanics got me interested in his work on quantum matter. The opportunity to work on measuring short-length-scale gravity with superconducting quantum interference devices was definitely a fantastic experience which taught me the excitement of doing research to probe the cutting-edge of what is possible. It was a joy interacting with the various members of the Davis group, and in particular I want to acknowledge Benjamin Hunt, Ethan Pratt, and Minoru Yamashita for introducing me to working with cryogenics and teaching me how to build things right, all the way from the design stage to the smallest details such as how to solder a wire onto a board in the best way possible. I learned a tremendous amount from all of these people.

I have also had the good fortune of being able to explore different aspects of science here at MIT. I was fortunate to be able to participate in Congressional Visits Day organized by the MIT Science Policy Initiative, which allowed me to experience first-hand how policy is made in the U.S. and how scientists can help the government make better decisions. I was also able to take courses on ‘Managing Nuclear Technology’ by Professor Richard Lester, ‘Law and Cutting-Edge Technologies’ by John Akula, and ‘Nuclear Forces and Missle Defenses’ by Professor Ted Postol. I learned a lot from all of these professors and they helped expand my understanding of how science and technology can affect society and vice versa. In particular, I want to acknowledge the advices Professor Postol gave me as I was considering my next position after graduate school. His lectures inspired me to make use of the technical understanding that I had developed through my studies of physics towards the betterment of society.

I want to thank my family, Itsuo, Kazuko, Maria, Lisa, and Julia who have supported me throughout my life and allowed me to pursue the path I wanted to take. I could not have asked for better parents and sisters.

Finally, I want to thank Nicole Lim and the entire Lim and Sy family for embracing me as part of their family. Our adventure is only beginning.

Contents

List of Figures

Chapter 1

Introduction

The realization of Bose-Einstein condensates (BECs) in ultracold atomic systems [7, 23] opened a new direction in the study of macroscopic quantum phenomena. These include the observation of matter wave interference [8], spinor dynamics [99], and vortex lattices [1], significantly deepening our understanding of quantum matter. It was clear from early on in the experimental exploration of BECs that there were deep connections between these atomic systems and those studied in condensed matter systems [62]. These include superfluidity as observed in liquid helium and superconductivity in various materials. At a fundamental level, many systems that were only accessible in condensed matter systems were now also open for investigation in atomic systems, but with different control parameters.

Some of the relevant properties and techniques that are unique to atomic systems include the existence of Feshbach resonances which allow experimentalists to tune the interaction energy between atoms [55], optical dipole traps to trap and manipulate atoms [95], and the ability to control the dimensionality of the system between three dimensions, two dimensions, and one dimensions [41]. Such controls allowed the exploration of quantum matter in systems which were complementary to what had been studied in condensed matter. The creation of quantum degenerate Fermi gases further diversified the type of systems realizable [27], allowing atomic physicists to study both bosonic as well as fermionic particles.

One major addition to the controllability and flexibility already discussed is the ability to genereate an optical lattice potential to create a crystalline structure analoglous to condensed matter systems [70, 13]. This has allowed the field to move in the direction of creating systems directly analogous to novel solid state materials such as high-temperature superconductors and magnetic phases of matter.

1.1 Quantum Simulation

Quantum simulation was first articulated by Richard Feynman [32], and the idea is that you can create a quantum system with exactly the same parameters as another one that is more controllable, and study what would have happened to the other system. Groundbreaking work on the superfluid to Mott insulator transition with a three-dimensional optical lattice [42] was an early success of how ultracold atoms in optical lattices can realize interesting many body physics as those found in condensed matter, where interactions between constituent particles in a lattice can be important.

Another example is the Fermi-Hubbard Hamiltonian [53], which in condensed matter describes electrons in a crystal which can undergo a transition from a conducting state to an insulating state and is of particular interest because of the belief of its strong connection to high-temperature superconductors in condensed matter [69]. The exact same Hamiltonian has been realized in ultracold atomic physics, where a fermionic atom resides in a three-dimensional crystal structure created by interfering light beams [88, 61]. Thus the idea is that by studying the Fermi-Hubbard Hamiltonian in atomic systems, physicists can gain a better understanding of the mechanisms behind high-temperature superconductors in condensed matter. Note the fact that the atoms must be fermionic in this case to more accurately simulate a condensed matter system made of electrons.

Fermions have a direct analogy to electrons in real condensed matter systems, whereas fundamentally bosonic particles do not exist in condensed matter. However, many interesting quasiparticles in condensed matter are bosonic in nature, including Cooper pairs in superconductors [20], excitons in semiconductors [119], and magnons in magnetic materials [14]. Thus although the constitutive particles in condensed matter are not bosons, understanding bosonic particles in ultracold atomic systems can significantly add to our understanding of quantum matter. From a theoretical point of view, bosonic systems are typically easier to calculate, so a precise comparison between theory and experiment can be possible [106]. Also, validating experimental techniques with bosonic systems where more experimental tools and understanding are available is invaluable to exploring fermionic systems [11, 90, 77]. Finally, the non-existence of fundamentally bosonic particles in condensed matter makes ultracold bosonic systems unique in that systems which were previously only of theoretical importance can now be studied experimentally [29].

1.2 Motivations and Outline

The rubidium lab at MIT which I belong to and where the work described in this thesis was done uses ultracold ^{87}Rb atoms [100], which are bosonic, and has been focusing on studying these atoms in optical lattices which closely mimic crystal structure in condensed matter. In particular our major goal has been to realize new magnetic forms of matter in its various guises.

One direction has been to realize and observe phase transitions to ferromagnetic and antiferromagnetic phases [85]. The fermionic antiferromagnet is expected to have deep connections with high-temperature superconductors, but the bosonic antiferromagnet is also expected to be interesting in its own right [39]. Towards that goal this lab has developed the technique of spin gradient thermometry and spin gradient demagnetization cooling, which has allowed us to measure and cool our system down to 300 pK, putting us in striking range of these magnetic states [115, 116, 76]. I was involved in the thermometry and cooling experiments in the first half of my Ph.D. studies, and the published papers are presented in appendices D, E, and F. In this thesis I describe our work on Bragg scattering applied to ultracold atoms, which will allow us to study the antiferromagnetic state once it is created.

Another direction has been to realize Hamiltonians which can be described by gauge fields [22]. These are analoglous to electrons in a magnetic field in condensed matter which gives rise to such phenomena as the quantum hall effect [107, 68, 120]. One important parameter for such systems is the magnetic flux enclosed per area, where the area is determined by the relevant length scale of the system. In condensed matter, the necessary magnetic fields to realize magnetic fluxes of order the magnetic flux quanta where interesting effects are expected to occur are at around a billion gauss due to the very small length scales involved of order ångstrom [52], which is unachievable in the laboratory. However, with cold atoms it may be possible to realize such effectively high magnetic fluxes [59, 37]. Much experimental progress has been made towards realizing and studying artificial gauge fields in ultracold atomic systems [72, 3, 101], but simple and robust schemes to achieve high magnetic fluxes have not yet been realized. In this thesis I describe a setup to realize very high magnetic fields which can give rise to such fascinating features as the Hofstadter butterfly, which is a fractal band structure.

This thesis is organized as follows. In chapter 2, I describe some of the basics of optical lattices, as well as the behavior of particles in a sinusoidal potential. The chapter also discusses the Bose-Hubbard Hamiltonian, Heisenberg Hamiltonian, and the Harper Hamiltonian. In chapter 3, I describe our work on Bragg scattering to study the Bose-Hubbard Hamiltonian and atomic dynamics. In chapter 4, I describe the scheme we have developed to realize artificial magnetic fields as well as experimental results to realize the Harper Hamiltonian. Then chapter 5 offers conclusions and outlooks.

Chapter 2

Ultracold Atoms in Optical Lattices

A coherent laser beam is a particularly versatile tool to control dilute, ultracold atomic systems due to their spectral purity as well as the controlability in spatial and temporal structure. In particular laser beams are standard tools used to trap and manipulate atoms to create new states of matter.

In this chapter I describe the principles behind optical lattices, as well as some of the properties of atoms in an optical lattice potential and the different types of Hamiltonians one can realize, including the Bose-Hubbard Hamiltonian, one of the simplest ultracold lattice systems which exhibit strong interaction effects, the Heisenberg Hamiltonian, which describes magnetic phases of matter including ferromagnets and antiferromagnets, and the Harper Hamiltonian, which exhibits topological properties of matter.

2.1 Optical Lattice Potential

Atoms that are sufficiently cold can by trapped at the focus of a Gaussian laser beam which induces a light shift if red-detuned to an atomic transition, thereby creating a potential minimum, which corresponds to an intensity maximum for the cold atoms to sit in [19, 96].

For an atom in an oscillating electric field $\mathbf{E}(t) = E\hat{\mathbf{e}}\cos\omega t$, the perturbing Hamiltonian $H'(t)$ can be written

$$H'(t) = -\mathbf{d}\cdot\mathbf{E}(t). \tag{2.1}$$

The energy shift due to an oscillating electric field is given by

$$\begin{aligned} U &= \frac{1}{2}\overline{\langle H'(t)\rangle} & (2.2)\\ &= -\sum_k \frac{E^2|D_{\mathrm{kg}}|^2}{4\hbar}\left(-\frac{1}{\delta_{kg}} + \frac{1}{\omega_{kg}+\omega}\right) & (2.3)\end{aligned}$$

where $D_{\mathrm{kg}} \equiv e\langle k|z|g\rangle$, $\delta_{\mathrm{kg}} \equiv \omega - \omega_{kg}$, and $I = c\epsilon_0 E^2/2$.

So far we have only considered a single coherent laser beam, but if we have two such beams, they can interfere and create a standing wave intensity pattern. The resulting sinusoidal potential which the atoms see is called an optical lattice.

Consider two plane electromagnetic waves $\mathbf{E}_1(\mathbf{r},t)$ and $\mathbf{E}_2(\mathbf{r},t)$ that are propagating in arbitrary directions $\hat{\mathbf{k}}_1$ and $\hat{\mathbf{k}}_2$ respectively, where $\mathbf{E}_1(\mathbf{r},t) = E_0\boldsymbol{\epsilon}_1 e^{i(\mathbf{k}_1\cdot\mathbf{r}-\omega t)}$ and $\mathbf{E}_2(\mathbf{r},t) = E_0\boldsymbol{\epsilon}_2 e^{i(\mathbf{k}_2\cdot\mathbf{r}-\omega t+\phi)}$, where $\boldsymbol{\epsilon}_{1,2}$ are polarization vectors, E_0 is the electric field magnitude, $\mathbf{k}_{1,2}$ are the wavevectors, and ϕ is an arbitrary constant phase. The total electric field is given by $\mathbf{E}_{\mathrm{tot}}(\mathbf{r},t) = \mathbf{E}_1(\mathbf{r},t) + \mathbf{E}_2(\mathbf{r},t)$. Then we have

$$\begin{aligned} |\mathbf{E}_{\mathrm{tot}}(\mathbf{r},t)|^2 &= E_0^2|\boldsymbol{\epsilon}_1 e^{i\mathbf{k}_1\cdot\mathbf{r}} + \boldsymbol{\epsilon}_2 e^{i(\mathbf{k}_2\cdot\mathbf{r}+\phi)}|^2 & (2.4)\\ &= E_0^2(2 + \boldsymbol{\epsilon}_1\cdot\boldsymbol{\epsilon}_2^* e^{i(\mathbf{k}_1\cdot\mathbf{r}-\mathbf{k}_2\cdot\mathbf{r}-\phi)} + \boldsymbol{\epsilon}_1^*\cdot\boldsymbol{\epsilon}_2 e^{-i(\mathbf{k}_1\cdot\mathbf{r}-\mathbf{k}_2\cdot\mathbf{r}-\phi)}) & (2.5)\\ &= 2E_0^2(1 + \boldsymbol{\epsilon}_1\cdot\boldsymbol{\epsilon}_2\cos((\mathbf{k}_1-\mathbf{k}_2)\cdot\mathbf{r}-\phi)), & (2.6)\end{aligned}$$

where we assumed the polarization vectors to be real. Now consider the case when the polarization vectors are parallel so that $\boldsymbol{\epsilon}_1\cdot\boldsymbol{\epsilon}_2 = 1$. Then, from $\cos^2\theta = (1+\cos 2\theta)/2$, we get

$$|\mathbf{E}_{\text{tot}}(\mathbf{r},t)|^2 = 4E_0^2\cos^2\left(\frac{(\mathbf{k}_1-\mathbf{k}_2)\cdot\mathbf{r}-\phi}{2}\right) \tag{2.7}$$

$$= 4E_0^2\cos^2\left(\mathbf{k}_{\text{eff}}\cdot\mathbf{r}-\frac{\phi}{2}\right) \tag{2.8}$$

where we define $\mathbf{k}_{\text{eff}} \equiv (\mathbf{k}_1-\mathbf{k}_2)/2$. If we define θ such that $\hat{\mathbf{k}}_1\cdot\hat{\mathbf{k}}_2 = \cos\theta$ and using $k = 2\pi/\lambda$, we get

$$\lambda_{\text{eff}} = \frac{1}{\sin(\theta/2)}\lambda, \tag{2.9}$$

where $k_{\text{eff}} \equiv 2\pi/\lambda_{\text{eff}}$. Thus, by intersecting laser beams at various angles, one can create an optical lattice with lattice spacings much greater than the wavelength of the laser beam itself. Also, note that the direction of the optical lattice will be modulated in the direction $\hat{\mathbf{k}}_1-\hat{\mathbf{k}}_2$.

In the work described in this thesis $\theta = \pi$, so $\lambda_{\text{eff}} = \lambda$ and we have

$$|\mathbf{E}_{\text{tot}}(\mathbf{r},t)|^2 = 4E_0^2\cos^2\left(\mathbf{k}\cdot\mathbf{r}-\frac{\phi}{2}\right). \tag{2.10}$$

Thus this periodic modulation in the intensity pattern creates an optical lattice, which the atoms reside in. The next section describes the properties of atoms in such a sinusoidal potential. Typically the lattice laser beams are significantly bigger than the optical dipole trap beams, so the spatial curvature due to the Gaussian envelope of the lattice beams can be neglected.

2.2 Atoms in a Periodic Potential

In 1D, a single atom in a standing wave is described by the Hamiltonian

$$H = \frac{p^2}{2m} + V_0\sin^2(k_l x), \tag{2.11}$$

where m is the mass of the particle, and $k_l = 2\pi/\lambda$ for an optical lattice with laser wavelength λ.

2.2.1 Bloch's Theorem and Bloch Functions

Bloch's theorem [9] tells us that if the Hamiltonian is invariant under translation by one lattice period a, the Hamiltonian commutes with the translation operator T, where

$$T = e^{ipa/\hbar} \text{ and } T\phi_q(x) = \phi_q(x+a). \tag{2.12}$$

Since T is unitary, it has eigenvalues such that

$$T\phi_q(x) = e^{iqa}\phi_q(x), \tag{2.13}$$

where $q \in [-\pi/a, \pi/a]$. Since

$$\phi_q(x+a) = e^{iqa}\phi_q(x), \tag{2.14}$$

we can write

$$\phi_q(x) = e^{iqx}u_q(x), \tag{2.15}$$

where $u_q(x)$ is a periodic function in x with period a i.e. $u_q(x) = u_q(x+a)$. Because the Hamiltonian and the translation operator commute, we can find simultaneous eigenstates of H and T such that

$$H\phi_q^{(n)}(x) = E_q^{(n)}\phi_q^{(n)}(x) \text{ and} \tag{2.16}$$

$$T\phi_q^{(n)}(x) = e^{iqa}\phi_q^{(n)}(x). \tag{2.17}$$

$\phi_q^n(x)$ are called Bloch eigenstates, and $u_q^n(x)$ are eigenstates of the Hamiltonian

$$H_q = \frac{(p+q)^2}{2m} + V_0 \sin^2(k_l x). \tag{2.18}$$

This follows from using the fact that

$$e^{-iqx} p e^{iqx} = p + q. \tag{2.19}$$

We would now like to determine the Bloch functions, which are normalized so that

$$\frac{2\pi}{a} \int_0^a |\phi_q^{(n)}(x)|^2 dx = 1. \tag{2.20}$$

The analytical solutions are of the form of Mathieu functions. However, numerically it is nicer to expand the Bloch functions in a Fourier expansion, where

$$u_q^n(x) = \frac{1}{\sqrt{2\pi}} \sum_{j=-\infty}^{\infty} c_j^{(n,q)} e^{-ik_l x j}. \tag{2.21}$$

This allows us to reduce the problem to a linear eigenvalue equation in the complex coefficients c_j. To do this, take Schrödinger's equation and use

$$\frac{1}{\sqrt{2\pi}} \int_{-\infty}^{\infty} dx e^{-ikx} = \sqrt{2\pi}\delta(k) \text{ and } \delta(ax) = \frac{1}{|a|}\delta(x). \tag{2.22}$$

By doing so we get

$$\sum_{j'=-l}^{l} H_{j,j'} c_{j'}^{(n,q)} = E_q^{(n)} c_j^{(n,q)}, \tag{2.23}$$

where

$$H_{j,j'} = \begin{cases} (2j + q/k_l)^2 E_{\mathrm{R}} + V_0/2, & \text{if } j = j'; \\ -V_0/4, & \text{if } |j - j'| = 1; \\ 0 & \text{if } |j - j'| > 1. \end{cases} \tag{2.24}$$

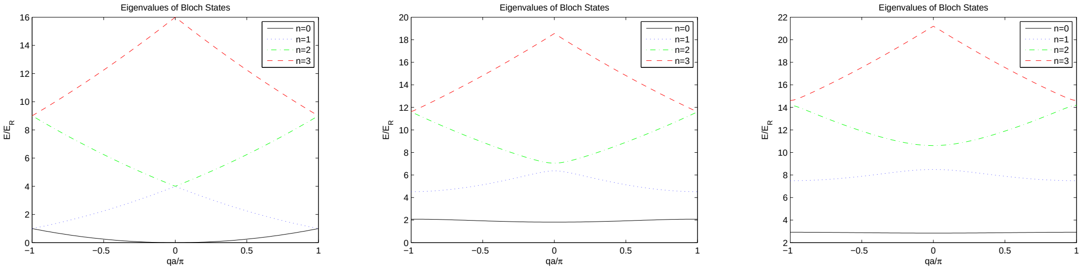

Figure 2-1: Band structure for an atom in an optical lattice. From left to right are the eigenvalues for an atom in a lattice for lattice depths $V_0 = 0E_{\mathrm{R}}$, $V_0 = 5E_{\mathrm{R}}$, and $V_0 = 10E_{\mathrm{R}}$ as a function of the quasimomentum q.

This problem can be diagonalized numerically using $j \in \{-l, \ldots, -l\}$ and for the lowest few bands, good results are obtained for relatively small l, i.e. $l \sim 10$. The numerically determined eigenvalues for the first few energy bands are given in Fig. 2-1.

2.2.2 Wannier Functions

It is often very convenient to write the Bloch functions in terms of Wannier functions, which also form a complete set of orthogonal basis states. The Wannier functions in 1D are given by

$$w_n(x - x_i) = \sqrt{\frac{a}{2\pi}} \int_{-\pi/a}^{\pi/a} dq u_q^{(n)}(x) e^{-iqx_i}, \tag{2.25}$$

where x_i are the minima of the potential. Each set of Wannier functions for a given n can be used to express the Bloch functions in that band as

$$u_q^{(n)}(x) = \sqrt{\frac{a}{2\pi}} \sum_{x_i} w_n(x - x_i) e^{iqx_i}. \tag{2.26}$$

This can be checked by plugging Eq. 2.26 into Eq. 2.25. Wannier functions have the advantage of being localized on particular sites, which makes them useful for describing local interactions between particles. The Wannier functions are not uniquely defined by the integral over Bloch functions since each wavefunction $\phi_q^{(n)}(x)$ is arbitrary up to a complex phase. However, it has been shown [65] that there exists for each band only one real Wannier function $w_n(x)$ that is

- either symmetric or anti-symmetric about either $x = 0$ or $x = a/2$ and
- falls off exponentially i.e. $|w_n(x)| \sim \exp(-h_n x)$ for some $h_n > 0$ as $x \to \infty$.

These Wannier functions are known as maximally localized Wannier functions, and are the ones frequently used. If $u_q^{(n)}(x)$ is expanded as in Eq. 2.21, the maximally localized Wannier functions can be produced if all $c_j^{(n,q)}$ are chosen to be purely real for the even bands *i.e.* $n = 0, 2, 4, \dots,$ and imaginary for the odd bands *i.e.* $n = 1, 3, 5, \dots,$ and are smoothly varying as a function of q. Wannier functions for deeply bound bands are very close to the harmonic oscillator wavefunctions, and for many analytical estimates of on-site properties, the Wannier functions may be replaced by harmonic oscillator wavefunctions if the lattice is sufficiently deep. The major difference between the two is that the Wannier functions are exponentially localized, *i.e.* $|w_n(x)| \sim \exp(-h_n x)$, whereas the harmonic oscillator wavefunctions decay more rapidly in the tails as $\exp\{-x^2/(2a_0)^2\}$.

2.2.3 Wannier-Stark States

Now consider a situtation where in addition to the periodic lattice potential we have a linear lilt potential due to an effective constant time-independent force F such that we obtain the Wannier-Stark Hamiltonian [45, 40]

$$H = \frac{p^2}{2m} + V_0 \sin^2(k_l x) + Fx. \tag{2.27}$$

Note that the linear tilt destroys the translation symmetry of the tiltless Hamiltonian, and so the Wannier wavefunctions will not be the proper description of a localized state. Being able to describe the localized wavefunctions resulting from this Hamiltonian, called Wannier-Stark states, is important in understanding our scheme for engineering the Harper Hamiltonian in an ultracold atomic system which is further described in chapter 4.

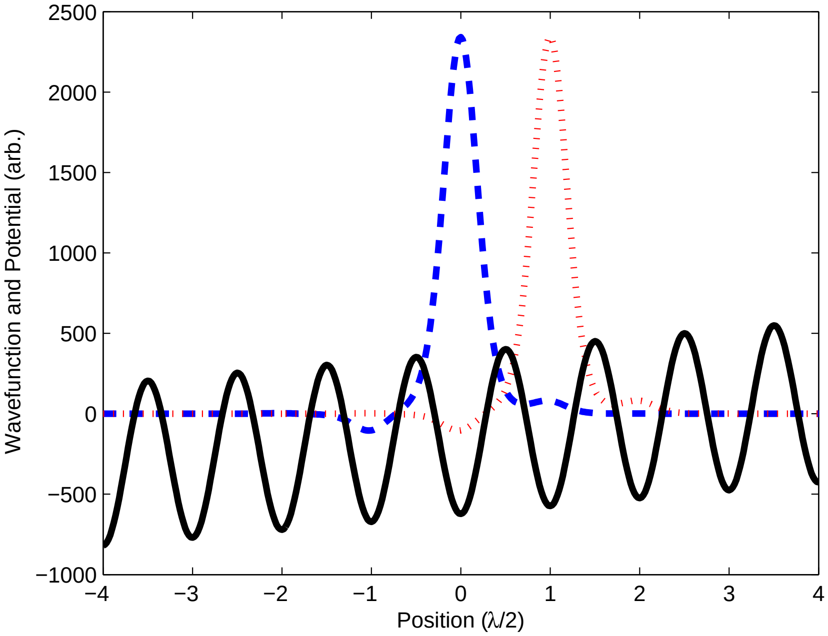

Figure 2-2: Wannier-Stark states in a tilted lattice.

In a sufficiently deep lattice such that the tight-binding approximation can be used, and a sufficiently steep tilt such that the bare tunneling energy J (this parameter is explained in the following section) is smaller than the energy offset between adjacent sites Fa, the Wannier-Stark Hamiltonian can be diagonalized in the basis of the Wannier-Stark states $|\Psi_{\alpha,l}\rangle$ given by

$$|\Psi_{\alpha,l}\rangle = \sum_m J_{m-l}\left(\frac{2J}{Fa}\right)|m\rangle, \tag{2.28}$$

where $|m\rangle$ are Wannier functions centered at site m, and $J_{m-l}(x)$ are Bessel functions. Thus when one is interested in the properties of a lattice system in the presence of a linear tilt potential, the Wannier-Stark states should be used instead of the Wannier states. Wannier-Stark states are depicted in Fig. 2-2.

2.3 Bose-Hubbard Hamiltonian and the Mott Insulator

Although band theory for non-interacting particles has been hugely successful in explaining the properties of a wide range of metals [9], there are a few shortcomings. In particular, there are a class of materials, including NiO, which band theory would predict should be conductors, but are in reality insulators [24]. The Hubbard model proposed by John Hubbard has been shown to explain quite well why this material is insulating [53, 63]. In particular, this model Hamiltonian captures the interactions between the electrons effectively in the tight-binding approximation and is a useful model to begin to understand the effects of interactions between constitutent particles in a lattice system.

The Bose-Hubbard Hamiltonian also describes a quantum phase transition between a superfluid state and an insulating state, called the Mott insulator [33, 58]. This was first observed in an ultracold atomic system in 2002 [42] and has been studied extensively since then. In chapter 3 of this thesis I describe our work on studying this quantum phase transition using the technique of Bragg scattering. The Mott insulating state is also the starting point in realizing spin gradient thermometry and demagnetization cooling, where the published papers [76, 116, 115] are included in this thesis as appendices D, E, and F.

Now in an ultracold atomic system, for bosonic atoms in a lattice and an external trapping potential, the Hamiltonian operator is given by [58]

$$\begin{aligned} H = \int d^3x \psi^\dagger(\mathbf{x}) \left(-\frac{\hbar^2}{2m}\nabla^2 + V_0(\mathbf{x}) + V_T(\mathbf{x}) \right) \psi(\mathbf{x}) \\ + \frac{1}{2}\frac{4\pi a\hbar^2}{m} \int d^3x \psi^\dagger(\mathbf{x})\psi^\dagger(\mathbf{x})\psi(\mathbf{x})\psi(\mathbf{x}), \quad (2.29) \end{aligned}$$

where $\psi(\mathbf{x})$ is a boson field operator for atoms in a given internal atomic state, $V_0(\mathbf{x})$ is the optical lattice potential, and $V_T(\mathbf{x})$ is the additional slowly varying external trapping potential, such as a magnetic or optical dipole trap. In the simplest case, the optical lattice potential has the form $V_0(\mathbf{x}) = \sum_{j=1}^{3} V_{j0}\sin^2(kx_j)$ with wavevector $k = 2\pi/\lambda$ where λ is the wavelength of the lattice beam. The interaction potential between the atoms is approximated by a short-range pseudopotential where a is the s-wave scattering length and m is the mass of the atom. If we assume the energies of the system are low enough that the atoms remain in the lowest band, we can expand the field operators in the Wannier basis and keep only the lowest vibration states and write $\psi(\mathbf{x}) = \sum_i a_i w(\mathbf{x} - \mathbf{x}_i)$. This then allows us to simplify Eq. 2.29 to obtain the Bose-Hubbard Hamiltonian

$$H = -J\sum_{\langle i,j\rangle} a_i^\dagger a_j + \frac{1}{2}U\sum_i \hat{n}_i(\hat{n}_i - 1) + \sum_i \epsilon_i \hat{n}_i, \tag{2.30}$$

where $\langle i,j\rangle$ denotes a sum over the nearest neighbor sites, the operators $\hat{n}_i = a_i^\dagger a_i$ count the number of bosonic atoms at site i. The annihilation and creation operators, a_i and $a_i^\dagger$ respectively, obey the canonical commutation relations $[a_i, a_j^\dagger] = \delta_{ij}$. The parameter $U = 4\pi a\hbar^2 \int d^3x\, |w(\mathbf{x})|^4/m$ corresponds to the strength of the on-site repulsion of two atoms on the lattice site i, a is the s-wave scattering length of the atom, $J = \int d^3x w^*(\mathbf{x}-\mathbf{x}_i)[-\frac{\hbar^2}{2m}\nabla^2 + V_0(\mathbf{x})]w(\mathbf{x}-\mathbf{x}_j)$ corresponds to the hopping matrix element between adjacent sites i and j, and $\epsilon_i = \int d^3x V_T(\mathbf{x})|w(\mathbf{x}-\mathbf{x}_i)|^2 \approx V_T(\mathbf{x}_i)$ corresponds to an energy offset of each lattice site.

One can use a harmonic approximation about the minima of the potential wells to determine these parameters. In particular, for 1D,

$$H' = \frac{p^2}{2m} + V_0\sin^2(kx) \approx \frac{p^2}{2m} + V_0k^2x^2 \tag{2.31}$$

$$= \frac{p^2}{2m} + \frac{1}{2}m\omega^2x^2 \tag{2.32}$$

$$\Rightarrow \omega^2 = \frac{2V_0k^2}{m} = \frac{4E_\mathrm{R}V_0}{\hbar^2} \Rightarrow \omega = \sqrt{\frac{4E_\mathrm{R}V_0}{\hbar^2}}, \tag{2.33}$$

where $E_\mathrm{R} = \hbar^2k^2/(2m)$ is the recoil energy. Furthermore, the ground state eigenfunction of this Hamiltonian can be written

$$w(x) = \frac{1}{(\pi\sigma^2)^{1/4}} e^{-\frac{x^2}{2\sigma^2}}, \tag{2.34}$$

where

$$\sigma = \sqrt{\frac{\hbar}{m\omega}} = \frac{\hbar}{m^{1/2}(4E_{\mathrm{R}}V_0)^{1/4}}. \tag{2.35}$$

The generalization to 3D is given by

$$w(\mathbf{x}) = \frac{1}{\pi^{3/4}(\sigma_1\sigma_2\sigma_3)^{1/2}} e^{-\left(\frac{x^2}{2\sigma_1^2}+\frac{y^2}{2\sigma_2^2}+\frac{z^2}{2\sigma_3^2}\right)}. \tag{2.36}$$

Using the expression for U and the above approximate Wannier function, we may write

$$U = \frac{4\pi a\hbar^2}{m} \int d^3x \, |w(\mathbf{x})|^4 \tag{2.37}$$

$$\approx \sqrt{\frac{8}{\pi}} ka \left(E_{\mathrm{R}}V_1V_2V_3\right)^{1/4}. \tag{2.38}$$

In all experiments described in this thesis, we work with lattice lasers of wavelength 1064 nm and ^{87}Rb atoms which weigh 1.443×10^{-25} kg with s-wave scattering length of $100a_0$ (in reality, the scattering length depends on the hyperfine states that are undergoing the scattering, but for ^{87}Rb all relevant scattering lengths are identical to within about 1% and so differences are typically negligible) [116]. For these parameters, Fig. 2-3 shows the interaction energy U, tunneling energy J, and the superexchange energy J^2/U as a function of lattice depth in units of the recoil energy E_{R}. These three terms set the energy scale of the system.

The on-site interaction energy term can be most naturally be understood as an energy between any two atoms on a single lattice site. In particular, if a lattice site has n atoms in it, then there are n choose 2 pairs that one can form, and each of

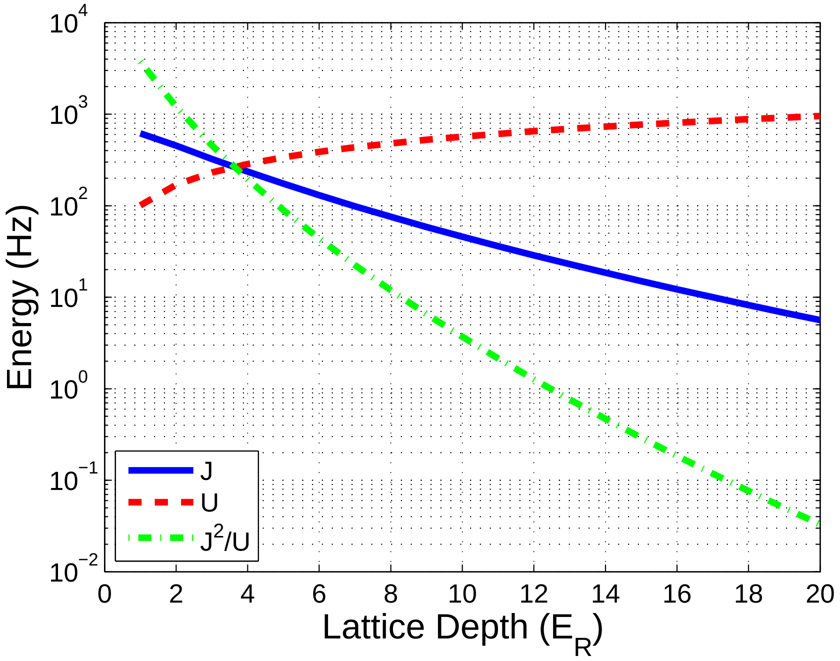

Figure 2-3: Dependence of Bose-Hubbard Hamiltonian parameters on lattice depth. Calculations are done for a 3D optical lattice of equal lattice depth in all three directions created by a laser of wavelength 1064 nm and ^{87}Rb atoms which weigh 1.443×10^{-25} kg with s-wave scattering length of $100a_0$.

these pairs contributes an energy U to the lattice site. This then gives us

$$E_n = \binom{n}{2} U = \frac{n(n-1)}{2} U. \tag{2.39}$$

Consider the case of zero tunneling, so that $J = 0$. The Hamiltonian is then simplified to

$$H = \frac{1}{2} U \sum_i \hat{n}_i(\hat{n}_i - 1) - \sum_i \mu_i \hat{n}_i. \tag{2.40}$$

It is clear that the eigenstate is the one where each lattice site has an integer number of atoms n_i. Furthermore, the Hamiltonian is now an independent sum of all of the lattice sites. Therefore for the case of $J = 0$, we need only consider a single lattice site. The energy of a single lattice site with n atoms is then

$$E_n = \frac{n(n-1)}{2}U - \mu n. \tag{2.41}$$

The energy of a lattice site with $n-1$ atoms is

$$E_{n-1} = \frac{(n-1)(n-2)}{2}U - \mu(n-1). \tag{2.42}$$

Consider the energy difference between the configuration with $n-1$ atoms and n atoms. Since the two terms in the energy have opposite signs, it is possible for there to be a critical n where it is just barely favorable to have one more particle in the site. The relevant energy to determine this critical n is the energy different between E_n and E_{n-1}. This is found to be

$$\Delta E_n \equiv E_n - E_{n-1} = (n-1)U - \mu. \tag{2.43}$$

The maximum possible n is determined by $\Delta E_n < 0$. This implies

$$n_{\max} < \frac{\mu}{U} + 1 \Rightarrow n_{\max} = \mathrm{Int}\left(\frac{\mu}{U}\right) + 1. \tag{2.44}$$

This discreteness of the possible occupation number is a distinct signature of the Mott insulator state and is what gives rise to the so-called ‘wedding cake structure.’ Such a discrete spatial structure is particularly amenable to the technique of Bragg scattering, which is described in detail in this thesis [77].

2.3.1 Mott Insulator Phase Diagram

Depending on the parameter J/U and μ/U, the system can be either in a Mott insulator or superfluid phase [79, 108]. The phase diagram can be found by considering the energy of the system using second-order perturbation theory. This requires a mean-field approximation, where the nearest-neighbor interactions as expressed by the term in the Hamiltonian with J are decoupled into single-site operators and an order parameter ψ, which in this case is $\psi = \sqrt{n}$. Furthermore, Landau's theory of second order phase transitions says that phase transitions occur when $d^2E/d\psi^2 = 0$, where the energy E can be expressed as $E = a_0 + a_2\psi^2 + \mathcal{O}(\psi^4)$, which requires that at the phase transition, $a_2 = 0$. With this understanding, the phase boundary is given by the equation

$$\frac{U}{zJ} = \frac{n+1}{n - \mu/U} + \frac{n}{1 - n + \mu/U}, \tag{2.45}$$

where z is the coordination number ($2 \times 3 = 6$ in the case of a 3 dimensional lattice), and the occupation number n is given by $n = \text{Integer}(\mu/U) + 1$ for $\mu/U > 0$ and $n = 0$ otherwise. The phase diagram determined by this expression is given in Fig. 2-4, where regions of occupation number up to 5 are shown.

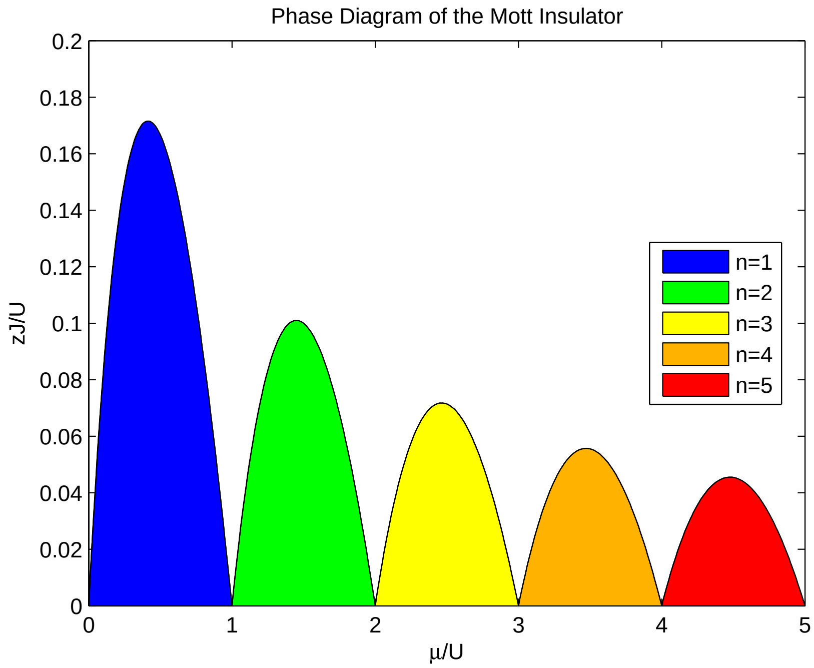

Figure 2-4: Phase diagram of the superfluid to Mott insulator transition. The colored regions correspond to the Mott insulator phase, and the white regions correspond to the superfluid phase. Occupation number regions of up to 5 are shown. The boundary is given by Eq. 2.45.

2.3.2 Non-Zero Temperature Effects

So far our description of the Bose-Hubbard Hamiltonian has assumed zero temperature. But of course in reality the system realized in an experiment is at a non-zero temperature. Understanding the system at non-zero temperature is particularly important when one is hoping to realize even lower energy Hamiltonians such as the Heisenberg Hamiltonian which we describe in the next section. Our results on spin gradient thermometry and demagnetization cooling, included in this thesis as appendices D, E, and F, relied strongly on our understanding of non-zero temperature effects.

Consider a Mott domain with n atoms per site. Then it is reasonable to expect that the lowest-lying excited states are particle and hole states, where an additional particle has been added/removed from the background occupation number of n [36, 51]. The energies of a particle and a hole are

$$E_{n,\text{particle}} = \frac{(n+1)n}{2}U - \frac{n(n-1)}{2}U = nU, \tag{2.46}$$

$$E_{n,\text{hole}} = \frac{(n-1)(n-2)}{2}U - \frac{n(n-1)}{2}U = -(n-1)U. \tag{2.47}$$

This particle-hole approximation allows us to truncate the Hilbert space of a lattice site to states with $n-1$, n, and $n+1$ atoms. Other states are suppressed by factors of $e^{-\beta U}$. Assuming $\beta U \ll 1$, this approximation is expected to be valid. In general, the partition function for a single site can be written,

$$z = \sum_n e^{-\beta H(n)} = \sum_n e^{-\beta(n(n-1)U/2-\mu n)}. \tag{2.48}$$

Truncating this to the relevant states and factoring the common term, we get

$$z = e^{-\beta H(n-1)} + e^{-\beta H(n)} + e^{-\beta H(n+1)} \tag{2.49}$$

$$\propto e^{-\beta(-(n-1)U+\mu)} + 1 + e^{-\beta(nU-\mu)} \tag{2.50}$$

$$= e^{-\beta(E_{\text{hole}}+\mu)} + 1 + e^{-\beta(E_{\text{particle}}-\mu)} \tag{2.51}$$

With this partition function, we can write down the probability for there to be a hole and particle in any given Mott region with occupation number n. This is found to be

$$p_{\text{hole}} = \frac{e^{-\beta(E_{\text{hole}}+\mu)}}{z} \tag{2.52}$$

$$p_{\text{particle}} = \frac{e^{-\beta(E_{\text{particle}}-\mu)}}{z}. \tag{2.53}$$

We can now calculate the mean occupation number at non-zero temperature as a function of the chemical potential and the interaction energy, given the probability of holes and particles. This is given by

$$\bar{n} = n + p_{\text{particle}} - p_{\text{hole}}. \tag{2.54}$$

This is plotted as a function of μ/U for various values of $U/k_{\text{B}}T$ in Fig. 2-5. One can see that the sharp steps a $T = 0$ become rounded as the temperature increases, and roughly at $k_{\text{B}}T/U \approx 0.2$, the sharpness has almost completely faded away. This value of 0.2 is commonly accepted as the 'melting temperature' of the Mott insulator.

2.4 Heisenberg Hamiltonian and Quantum Magnetism

The Heisenberg Hamiltonian is a model which describes spin-spin interactions in a lattice and gives rise to phases such as ferromagnetic and antiferromagnetic states [29]. This Hamiltonian can be realized from the Bose-Hubbard Hamiltonian in the perturbative limit of $J/U \ll 1$, where the relevant energy scale becomes J^2/U, also called the superexchange energy scale. This energy scale corresponds to a temperature of order 100 pK for rubidium atoms in a 3D lattice of lattice spacing a few hundred nanometers. Our work on spin gradient thermometry and demagnetization cooling, included in this thesis as appendices D, E, and F, were particularly driven by our goal of realizing the Heisenberg Hamiltonian which requires very low temperatures. Our work on Bragg scattering, described in chapter 3, was undertaken with the goal

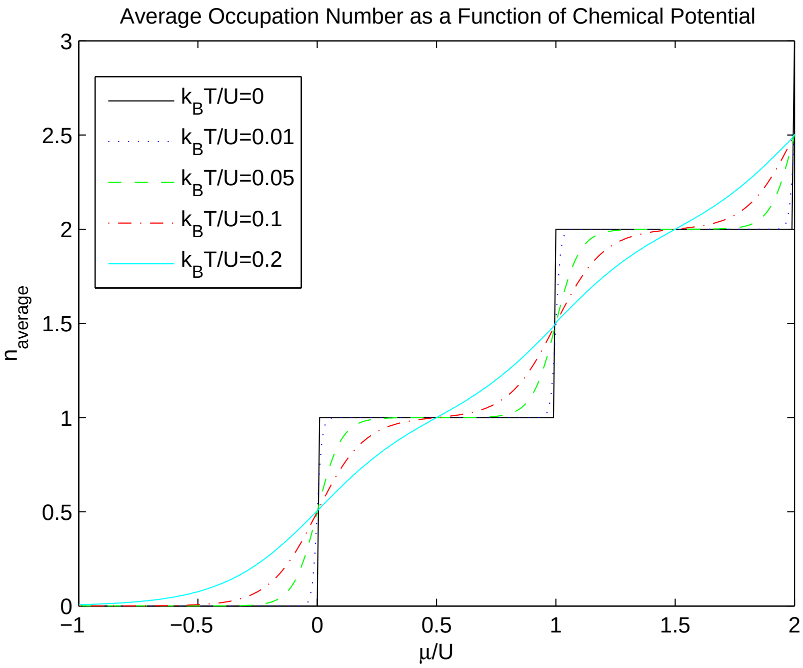

Figure 2-5: Average occupation number as a function of chemical potential for various temperatures. These steps are often call the 'wedding cake structure.'

of applying it to study spin ordering once the Heisenberg Hamiltonian is realized.

Let us start with a system where two different effective spin species interact differently in a lattice [29]. Denote the two relevant internal states with the effective spin index $\sigma = \uparrow, \downarrow$ respectively. These two spins are trapped in a perodic potential $V_{\mu\sigma} \sin^2(\mathbf{k}_\mu \cdot \mathbf{r})$ in a certain direction μ where $\mathbf{k}_\mu$ is the wavevector of light. For sufficiently strong periodic potential and low temperatures, the low energy Hamiltonian is given by

$$H = -\sum_{\langle i,j\rangle,\sigma} \left(t_{\mu\sigma} a^\dagger_{i\sigma} a_{j\sigma} + \text{H.c.} \right) + \frac{1}{2} \sum_{i,\sigma} U_\sigma n_{i\sigma} \left(n_{i\sigma} - 1 \right) + U_{\uparrow\downarrow} \sum_i n_{i\uparrow} n_{i\downarrow}, \tag{2.55}$$

where $\langle i, j \rangle$ denotes the nearest neighbor sites in the direction μ, $a_{i\sigma}$ are bosonic annihilation operators for atoms of spin σ localized on site i, and $n_{i\sigma} = a^\dagger_{i\sigma} a_{i\sigma}$.

Using the harmonic Wannier functions, the spin-dependent interaction energy $U_{\uparrow\downarrow}$

is given by

$$U_{\uparrow\downarrow} = \frac{4\pi a_{\uparrow\downarrow}\hbar^2}{m} \int d^3x \, |w_\uparrow(\mathbf{x})|^2 \, |w_\downarrow(\mathbf{x})|^2 \tag{2.56}$$

$$\approx \sqrt{\frac{8}{\pi}} k a_{\uparrow\downarrow} \left(E_{\mathrm{R}} \bar{V}_{1\uparrow\downarrow} \bar{V}_{2\uparrow\downarrow} \bar{V}_{3\uparrow\downarrow}\right)^{1/4}, \tag{2.57}$$

where $\bar{V}_{\mu\uparrow\downarrow} = 4V_{\mu\uparrow}V_{\mu\downarrow}/(V_{\mu\uparrow}^{1/2} + V_{\mu\downarrow}^{1/2})^2$ is the spin average potential in each direction.

2.4.1 Anisotropic Heisenberg Hamiltonian

Using a generalization of the Schrieffer-Wolff transformation [50, 89] (or another method [67]), to leading order in $t_{\mu\sigma}/U_{\uparrow\downarrow}$, Eq. 2.55 is equivalent to the effective Hamiltonian

$$H = \sum_{\langle i,j \rangle} \left[\lambda_{\mu z} \sigma_i^z \sigma_j^z - \lambda_{\mu\perp} \left(\sigma_i^x \sigma_j^x + \sigma_i^y \sigma_j^y\right)\right], \tag{2.58}$$

where $\sigma_i^z = n_{i\uparrow} - n_{i\downarrow}$, $\sigma_i^x = a_{i\uparrow}^\dagger a_{i\downarrow} + a_{i\downarrow}^\dagger a_{i\uparrow}$, and $\sigma_i^y = -i(a_{i\uparrow}^\dagger a_{i\downarrow} - a_{i\downarrow}^\dagger a_{i\uparrow})$ are the usual spin operators. The parameters $\lambda_{\mu z}$ and $\lambda_{\mu\perp}$ are given by

$$\lambda_{\mu z} = \frac{t_{\mu\uparrow}^2 + t_{\mu\downarrow}^2}{2U_{\uparrow\downarrow}} - \frac{t_{\mu\uparrow}^2}{U_\uparrow} - \frac{t_{\mu\downarrow}^2}{U_\downarrow} \text{ and } \lambda_{\mu\perp} = \frac{t_{\mu\uparrow} t_{\mu\downarrow}}{U_{\uparrow\downarrow}}. \tag{2.59}$$

Note that the Hamiltonian in Eq. 2.58 is the well-known anisotropic Heisenberg model (XXZ model) which arises in various condensed matter systems [10].

One can also consider the case where an external magnetic field along the z direction is applied. The Hamiltonian then becomes

$$H = \sum_{\langle i,j \rangle} \left[\lambda_{\mu z} \sigma_i^z \sigma_j^z - \lambda_{\mu\perp} \left(\sigma_i^x \sigma_j^x + \sigma_i^y \sigma_j^y\right)\right] - \sum_i h_z \sigma_i^z. \tag{2.60}$$

Now assume that the tunneling and same-spin interaction energies are the same for the two spin states. We can perform a variational calculation on the minimum energy of this system by two trial functions (i) a Néel state in the z direction $\langle \boldsymbol{\sigma}_i \rangle = (-1)^i \mathbf{e}_z$; (ii) a canted phase with ferromagnetic order in the $x-y$ plane and finite polarization in the z direction $\langle \boldsymbol{\sigma}_i \rangle = \cos\theta \mathbf{e}_x + \sin\theta \mathbf{e}_z$. Here θ is a varational parameter and $\mathbf{e}_{x,z}$ are unit vectors in the direction x, z. We then take the expectation value of H for each case to get

$$\langle H \rangle_{\mathrm{N}} = -\frac{Z\lambda_z}{2}, \text{ and } \langle H \rangle_{\mathrm{F}} = \frac{Z\lambda_z}{2}\sin^2\theta - \frac{Z\lambda_\perp}{2}\cos^2\theta - h_z \sin\theta, \tag{2.61}$$

where $\langle H \rangle_{\mathrm{N}}$ and $\langle H \rangle_{\mathrm{F}}$ are the Néel and canted phases respectively and Z is the coordination number corresponding to the number of nearest neighbors.

We can minimize the expression for the canted phase with respect to θ to get

$$\cos\theta (Z(\lambda_z + \lambda_\perp)\sin\theta - h_z) = 0. \tag{2.62}$$

The energy is minimized when

$$\cos\theta = 0 \quad \text{or} \quad \sin\theta = \frac{h_z}{Z\lambda_\perp} \times \frac{1}{1 + \lambda_z/\lambda_\perp}. \tag{2.63}$$

The two values that minimize the energy are $\theta = \pi/2, \sin^{-1}(h_z/Z(\lambda_z + \lambda_\perp))$. Note $\theta = \pi/2$ corresponds to the z ferromagnetic phase, and whose energy is given by

$$\langle H \rangle_{\mathrm{z}} = \frac{Z\lambda_z}{2} - h_z. \tag{2.64}$$

At this point, we are ready to determine the phase boundaries between the z ferromagnet, xy ferromagnet, and the antiferromagnet states. We can let $y \equiv \lambda_z/\lambda_\perp$ and $x \equiv h_z/Z\lambda_\perp$ for ease of manipulation. Then if we consider $\langle H \rangle_{\mathrm{z}} = \langle H \rangle_{\mathrm{F}}$, we obtain

$$y = x - 1 \Rightarrow h_z = Z\left(\lambda_z + \lambda_\perp\right). \tag{2.65}$$

We can also consider $\langle H \rangle_{\mathrm{N}} = \langle H \rangle_{\mathrm{F}}$ to obtain

$$y = \sqrt{x^2 + 1} \Rightarrow h_z = Z\sqrt{\lambda_z^2 - \lambda_\perp^2}. \tag{2.66}$$

The phase diagram dictated by Eqs. 2.63, 2.65 and 2.66 is given in the left plot of Fig. 2-6. For an actual ultracold atomic experiment, we can assume that there are no spin-flips and that the density of atoms throughout the sample must remain the same. To explore this phase space, we can apply a controlled magnetic field gradient, so that $B \approx x(dB/dx)$ and can take a slice along the horizontal direction with one sample. If we create a sample with an equal mixture of $\uparrow$ and $\downarrow$ atoms, then from the previous assumption, the only thing that the spins can do is rearrange themselves in the sample. Spin $\uparrow$ atoms will congregate in the lower field region and spin $\downarrow$ atoms will congregate in the higher field region. Then it is natural to expect the center of the sample to have zero spin, and the sample will have a symmetric spin profile about the center.

As can be seen in the Hamiltonian, the energy scale for these phases are of order t^2/U, which for typical experimental paramters for ^{87}Rb are on the order of 100 pK [15]. Thus this low energy scale causes difficulties in preparing such phases of matter. However, recent work performed in this group shows that such low temperatures can be achieved by the method of adiabatic spin gradient cooling [76].

These phase diagrams represent magnetic phases of matter, which in its fermionic incarnation is believed to form the basis for high-temperature superconductors [69]. Thus there is great technological as well as scientific interest in understanding the properties of this Hamiltonian.

2.4.2 Quantum Magnetism and Bragg Scattering

The Bose-Hubbard Hamiltonian has been studied extensively since its observation in 2002 [42]. One major step in this field would be to study an even lower temperature phase, which is the Heisenberg Hamiltonian. Bragg scattering will be a powerful tool to study the magnetic phases of matter arising from the Heisenberg Hamiltonian by making use of spin-dependent scattering, as was done in neutron scattering to observe the antiferromagnetic state [91]. Chapter 3 describes our work to study the Bose-Hubbard Hamiltonian with Bragg scattering, thus paving the way towards its employment in the search for quantum magnetism in optical lattices.

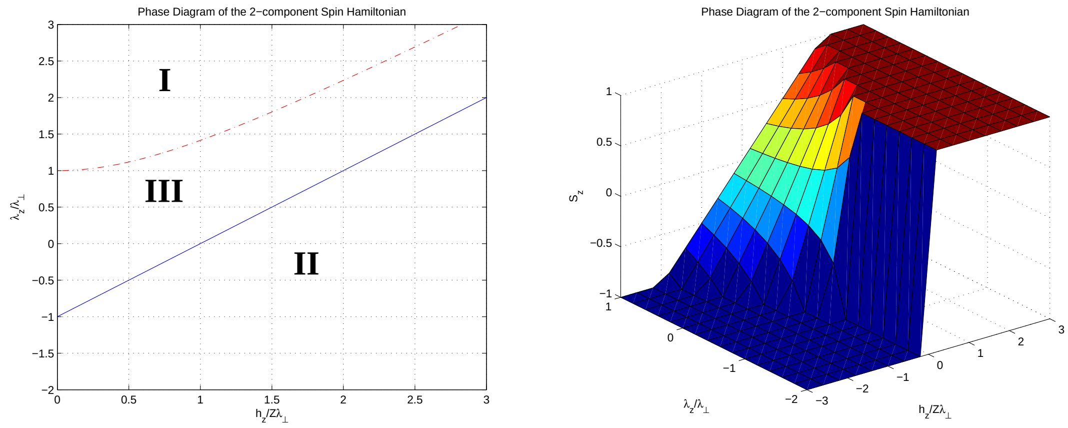

Figure 2-6: Phase diagrams of the Heisenberg Hamiltonian. The left figure is characterized by the following order parameter: I, z-Néel order; II, z-ferromagnetic order; and III, xy-ferromagnetic order. The right figure is the same plot as the left figure but with the spin along the magnetic field direction ($\sin\theta$) represented by the vertical axis.

2.5 Harper Hamiltonian and Gauge Fields

Gauge fields play an important role in various areas of modern physics, from particle physics, where the Standard Model relies heavily on gauge fields [81], to condensed matter physics, where gauge fields can explain the integer and fractional quantum Hall effects [107, 68]. Quantum Hall effects are interesting because they can manifest topological properties of wavefunctions, which could form the basis of a robust quantum computing platform due to the fact that environmental noise have a much more difficult time perturbing topological properties of matter [64]. In condensed matter, gauge fields can help to explain the dynamics of electrons in magnetic fields. However, gauge fields in condensed matter systems can be more general than magnetic fields because they can describe non-abelian gauge fields [94, 48].

One particular type of Hamiltonian that can give rise to such quantum Hall effects is the Harper Hamiltonian [105]. This Hamiltonian describes the dynamics and energy levels of electrons moving in the presence of a magnetic field and a background lattice in the tight-binding limit [49]. This Hamiltonian has been shown to exhibit

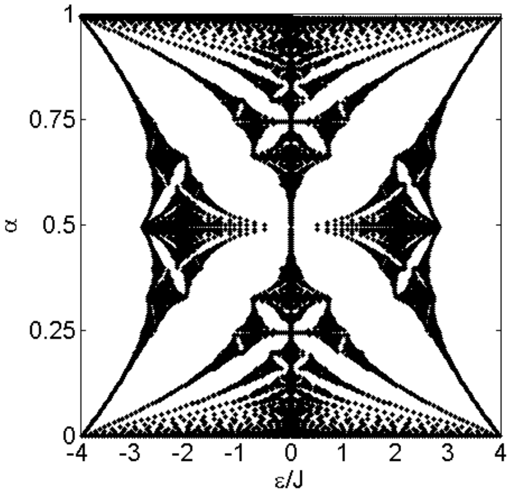

Figure 2-7: The Hofstadter butterfly [52]. This plot shows the fractal nature of the Harper Hamiltonian. The x-axis is in units of the eigenenergy per tunneling energy and the y-axis is in units of the enclosed flux quanta.

a fascinating fractal band structure which is colloqually called the 'Hofstadter butterfly', named after the discover Douglas Hofstadter [52]. Such a band structure is shown in Fig. 2-7.

The particular Harper Hamiltonian we are interested in can be written as

$$H = -K \sum_{m,n} \left(e^{i\phi_{m,n}} a^{\dagger}_{m+1,n} a_{m,n} + e^{-i\phi_{m,n}} a^{\dagger}_{m,n} a_{m+1,n} \right) \\ - J \sum_{m,n} \left(a^{\dagger}_{m,n+1} a_{m,n} + a^{\dagger}_{m,n} a_{m,n+1} \right) \quad (2.67)$$

where K and J are tunneling amplitudes in the x and y directions respectively, $a^{\dagger}_{m,n}$ and $a_{m,n}$ are the creation and annihilation operators, respectively, at site (m, n), and the indices m and n are for the x and y lattice positions respectively. In general, for the scheme we are interested in we can write $\phi_{m,n} = m\phi_x + n\phi_y$. In chapter 4 I describe in more detail how this Hamiltonian can be engineered with ultracold atoms, but for the purposes of this section I would like to focus on the properties of this Hamiltonian.

2.5.1 Electromagnetism, Gauge Fields, and Wavefunctions

The phase that the wavefunction acquires upon tunneling is directly related to another important concept in physics, namely that of gauges [86, 44, 109].

In electromagnetism, the electric field **E** and magnetic field **B** can be written in terms of the scalar potential ϕ and vector potential **A** as

$$\mathbf{E} = -\nabla\phi - \frac{\partial \mathbf{A}}{\partial t} \quad \text{and} \quad \mathbf{B} = \nabla \times \mathbf{A}. \tag{2.68}$$

Quantum mechanically, the Hamiltonian can be written in the following way to incorporate the scalar and vector potentials

$$H = \frac{(\mathbf{p} - q\mathbf{A})^2}{2m} + q\phi. \tag{2.69}$$

Now, it is possible to rewrite ϕ and **A** in a way such that it leaves the electric and magnetic fields unchanged. Namely,

$$\phi' = \phi - \frac{\partial \Lambda}{\partial t} \quad \text{and} \quad \mathbf{A}' = \mathbf{A} + \nabla\Lambda, \tag{2.70}$$

where Λ is in general any function of space and time. Thus the particular form of the scalar and vector potentials that give rise to specific electric and magnetic fields are not unique, but is defined up to a gauge given by the function Λ [57]. One speaks of 'choosing a gauge' in solving specific problems. For example, one could choose the gauge $\nabla \cdot \mathbf{A} = 0$.

Here let us consider the situation of time-independent fields and potentials. If you have a particle moving in the presence of some vector potential **A**, the wavefunction of the particle evolves as [2]

$$\psi = \psi_0 \exp\left[\frac{iq}{\hbar}\int \mathbf{A} \cdot d\mathbf{x}.\right] \tag{2.71}$$

Now we will consider a specific example where this phase of the wavefunction can manifest itself in an observable.

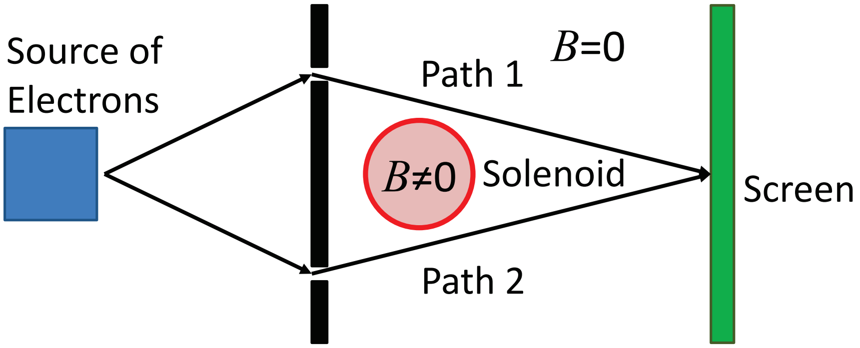

Figure 2-8: Setup for the Aharonov-Bohm effect. Electrons emerge from the electron source to the left, traverse through two slits, and then impinge on a screen to the right. In between is an infinitely long solenoid which has a non-zero magnetic field inside, but zero magnetic field outside. Even though the magnetic field is zero where the electrons are, they feel the effect of the magnetic field inside the solenoid.

Consider the following set up, shown in Fig. 2-8. We have a source of electrons to the left, which pass through two slits. Beyond the slits, there is an infinitely long solenoid pointing out of the page which is also impenetrable to the electrons. Thus we can consider this solenoid to have zero magnetic field anywhere outside of the solenoid. Note however that the vector potential can still be non-zero in the outer region. After passing through the slits the electrons impinge on a screen.

Now if we consider the wavefunction of an electron which traveled around path 1 and path 2 to the same point on the screen, the probability to observe the electron will be determined by the sum of the two wavefunctions. This can be written

$$\psi_{tot} = \psi_1 \exp\left(\frac{iq\int_{\text{path1}} d\mathbf{x}\cdot\mathbf{A}}{\hbar}\right) + \psi_2 \exp\left(\frac{iq\int_{\text{path2}} d\mathbf{x}\cdot\mathbf{A}}{\hbar}\right) \tag{2.72}$$

$$= \exp\left(\frac{iq\int_{\text{path2}} d\mathbf{x}\cdot\mathbf{A}}{\hbar}\right)\left[\psi_1 \exp\left(\frac{iq\oint d\mathbf{x}\cdot\mathbf{A}}{\hbar}\right) + \psi_2\right] \tag{2.73}$$

$$= \exp\left(\frac{iq\int_{\text{path2}} d\mathbf{x}\cdot\mathbf{A}}{\hbar}\right)\left[\psi_1 \exp\left(\frac{iq\Phi}{\hbar}\right) + \psi_2\right], \tag{2.74}$$

where we used the fact that the integral $\oint d\mathbf{x}\cdot\mathbf{A}$ is exactly the magnetic flux Φ through the solenoid. The observable is the wavefunction squared, and due to the complex phase, the resulting probability of observing an electron on the screen will oscillate as a function of the magnetic flux. It is very curious that even though the electron never enters the region with non-zero magnetic field, the probability to observe an electron depends on the magnetic field in the forbidden region. This is the celebrated Aharonov-Bohm effect [2], also sometimes called the Ehrenberg-Siday effect [30]. This effect beautifully illustrates the fact that two different paths can imprint non-trivial topological phases on wavefunctions just by enclosing a region with magnetic flux.

2.5.2 Flux Density per Plaquette α

Now that we have an appreciation of the connection of topological properties to the phase of the wavefunction, which in turn can be understood as a particular gauge chosen for the system, let us return to the Harper Hamiltonian written as Eq. 2.67 and understand how the phase relates to an effective magnetic field. As we saw previously, we can write the phase as $\phi_{m,n} = m\phi_x + n\phi_y$ where m and n are integers describing the position in the two-dimensional lattice and $\phi_{x,y}$ are constants. Then a phase will be accumulated upon tunneling in the x direction. In this case the phase accumulated can be shown as in the left of Fig. 2-9. We see that the total phase accumulated if one atom tunnels around one full square, called a plaquette or a unit cell, is $\Phi = \phi_y$. Note that the total accumulated phase only depends on the y dependence of the phase accumulated upon tunneling in the x direction.

The flux density per plaquette is defined as $\alpha \equiv \Phi/(2\pi)$. This parameter has a strong connection to electrons with charge e in a square two-dimensional lattice of side a in a magnetic field B [52]. Hofstadter defines this parameter as (in SI units)

$$\alpha = \frac{a^2 B}{h/e}. \tag{2.75}$$

This is precisely the magnetic flux enclosed by a square of side a divided by the magnetic flux quantum of an electron. This shows that for a typical crystal with lattice spacing of a few ångstroms, magnetic fields on the order of a billion gauss is necessary to achieve α of order unity. However, very recently researchers have devised a clever

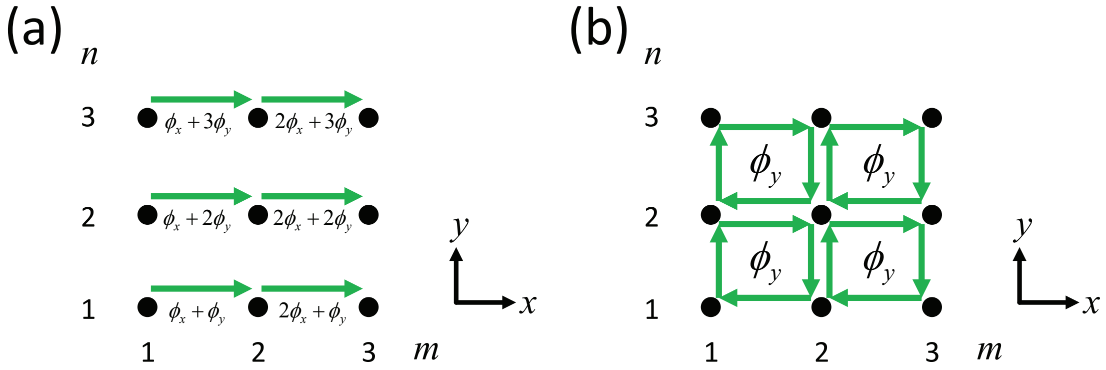

Figure 2-9: Phase accumulated upon tunneling and enclosed flux. (a) shows the phase accumulated upon tunneling from site (m, n) to $(m+1, n)$. (b) shows the total phase accumulated after tunneling as $(m, n) \to (m, n+1) \to (m+1, n+1) \to (m+1, n) \to (m, n)$, which is ϕ_y for each such plaquette.

scheme by using boron nitride and a layer of graphene on top and slightly rotated from each other to create an effectively much more widely spaced superlattice on the order of tens of nanometers. This allowed the researchers to observe the signatures of the Hofstadter butterfly through conductivity measurements in magnetic fields of tens of tesla [26, 54]. Our proposal with ultracold atoms in optical lattices allow us to achieve effectively high magnetic fields by making use of Raman transitions which impart phases upon tunneling, which will be discussed in more detail in chapter 4.

2.5.3 Band Structure for $\alpha = 1/2$

As an example, here we we consider the specific case $\phi_x = -\pi$ and $\phi_y = \pi$ which leads to $\phi = \pi(-m+n)$ and therefore $\alpha = 1/2$. This is the particular type of phase we initially study experimentally, but any other phase dependence and consequently any other α is also realizable. Schematically the Hamiltonian can be represented as the left part of Fig. 2-10.

The 2D square lattice can be divided into two sub-lattices, where an atom on one sub-lattice accumulates a phase of 0 when it tunnels one site in the $+\hat{\mathbf{x}}$ direction, and an atom in the other sub-lattice accumulates a phase of π when it tunnels one site in the $+\hat{\mathbf{x}}$ direction. These two sub-lattices are represented by filled and unfilled circles

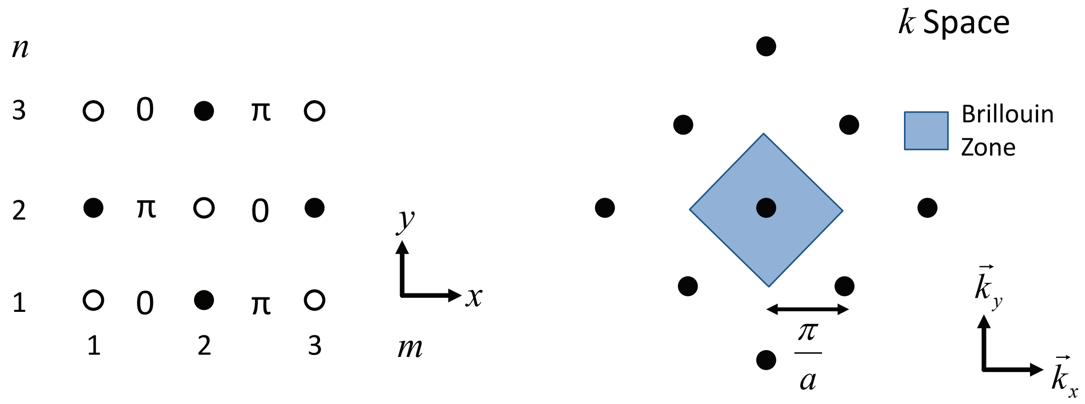

Figure 2-10: Schematic of a two-dimensional lattice with phases. The left figure is in real space, where the phase accumulated upon tunneling is represented. The right figure is the reciprocal space representation, along with the first Brillouin zone highlighted.

in the left of Fig. 2-10. With these two sub-lattices, we can define primitive vectors and basis vectors [9].

We see that the primitive vectors are $\mathbf{a}_1 = a(\hat{\mathbf{x}} - \hat{\mathbf{y}})$ and $\mathbf{a}_2 = a(\hat{\mathbf{x}} + \hat{\mathbf{y}})$ where a is the lattice spacing. The basis vectors are $\mathbf{b}_1 = 0$ and $\mathbf{b}_2 = a\hat{\mathbf{x}}$. The reciprocal lattice vectors are $\mathbf{c}_1 = \frac{\pi}{a}(\hat{\mathbf{x}} - \hat{\mathbf{y}})$ and $\mathbf{c}_2 = \frac{\pi}{a}(\hat{\mathbf{x}} + \hat{\mathbf{y}})$. The Brillouin zone is then a tilted square at $\theta = 45°$ and is shown in the right of Fig. 2-10. With this information, we can calculate the band structure for this system.

The Hamiltonian in matrix form is,

$$H = \begin{pmatrix} 0 & J\left(e^{ik_y a} + e^{-ik_y a}\right) + K\left(e^{ik_x a} - e^{-ik_x a}\right) \\ J\left(e^{-ik_y a} + e^{ik_y a}\right) + K\left(e^{-ik_x a} - e^{ik_x a}\right) & 0 \end{pmatrix} \tag{2.76}$$

$$= \begin{pmatrix} 0 & 2J\cos(k_y a) + 2iK\sin(k_x a) \\ 2J\cos(k_y a) - 2iK\sin(k_x a) & 0 \end{pmatrix}. \tag{2.77}$$

The band structure then is

$$E_\pm(k_x, k_y) = \pm 2\sqrt{J^2\cos^2(k_y a) + K^2\sin^2(k_x a)}. \tag{2.78}$$

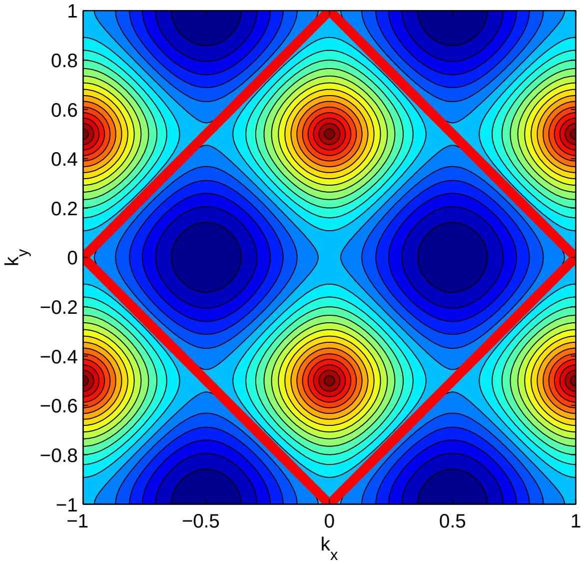

Figure 2-11: Band structure of the $\alpha = 1/2$ Harper Hamiltonian. It is a contour plot of the lowest band structure, where we have two minima and two Dirac cones in the Brilloin zone, the boundary which is given in red bold lines.

The lower branch is plotted in Fig. 2-11. We see that the band minima are at $(k_x, k_y) = (\pm\pi/(2a), 0)$. Furthermore, the band has Dirac points at $(k_x, k_y) = (0, \pm\pi/(2a))$ where the band gap between the two bands is zero.

Another approach to solving the same problem is to use the concept of magnetic unit cells [121, 122, 78, 83]. This approach is well-suited to lattice systems which have such non-trivial phases associated with tunneling between neighboring lattice sites.

Different phase dependencies corresponding to different α will give rise to different band structures. For non-rational α, the system will not have any periodicity and so a band description will not be appropriate, but practically any α realized will have some spread and will include rational α and so a band description should be adepquate even if one does not precisely achieve rational α [52]. Furthermore, if interactions are added to the Harper Hamiltonian, even more fascinating states such as fractional quantum Hall states are expected to arise [94, 48]. Therefore the Harper Hamiltonian provides an exciting new frontier in the study of topological states of matter, both with and without interactions.

Chapter 3

Bragg Scattering as a Probe of Ordering and Quantum Dynamics

This chapter elaborates on the work published as *Bragg Scattering as a Probe of Atomic Wave Functions and Quantum Phase Transitions in Optical Lattices*, Phys. Rev. Lett. **107**, 175302 (2011) [77].

As discussed in the introduction, ultracold atomic gases are an ideal system in which to study many-body phenomena because of the relative ease with which parameters in the model Hamiltonian can be tuned across a wide range [70, 13]. Such studies have resulted in a better understanding of various phase transitions such as the Berezinskii-Kosterlitz-Thouless transition in two dimensional systems [47], the BEC-BCS crossover of interacting fermions [123] and the superfluid to Mott insulator transition in a three-dimensional lattice [42]. One major goal of this field is to realize spin phases such as antiferromagnetic states to explore quantum magnetism and its interplay with high-temperature superconductivity [69].

Concurrently, there are numerous efforts to develop techniques to probe and understand the atomic ensemble once a new type of ordering is achieved. One recent development is the realization of single-site resolution of atoms in two-dimensional optical lattices [11, 90]. An alternative method to measure *in situ* spatial ordering is the technique of Bragg scattering, often used in a condensed matter context to determine crystal structure [9]. In particular, Bragg scattering with neutrons led to the discovery of antiferromagnetism in the solid state [91] and with x-rays led to the discovery of the double helix structure of DNA [111].

Bragg scattering relies on the interference of waves scattered coherently from an ensemble of particles. In particular when atoms are arranged in a periodic pattern in three spatial dimensions, there are certain angles of the incoming and reflected beams where scattering is dramatically enhanced compared to other angles. This has allowed crystallographers to use x-rays to determine the properties of crystals such as lattice geometry at the ångstrom scale. We have applied this technique to ultracold atoms in a three-dimensional optical lattice by scattering near-infrared light where the atoms are spaced almost 10^4 times farther apart than those in typical condensed matter samples.

Pioneering works on Bragg scattering from cold atoms in optical lattices were done by the Hänsch and Phillips groups using laser cooled atoms [113, 12, 84, 112]. These lattices were sparsely populated and the atoms occupied several bands. In this Letter, we have used Bragg scattering to study bosonic atoms cooled to quantum degeneracy and placed in a three dimensional cubic lattice where the atoms occupy the lowest band. In particular, we have measured directly the Heisenberg-limited width of both position and momentum of the single ground state atomic wavefunction in an optical lattice. Furthermore, there is a revival of Bragg scattered light some time after releasing the atoms from the optical lattice, analogous to the optical Talbot effect. This signal gives a direct measure of the coherence of the superfluid component in the lattice.

3.1 Experimental Setup for Bragg Scattering

Laser cooling and evaporative cooling are used to achieve quantum degeneracy of ^{87}Rb atoms in the $|F = 2, m_F = -2\rangle$ state [100] which are loaded into a crossed dipole trap whose trap frequencies range between 30 and 160 Hz. Once quantum degeneracy is achieved, the optical lattices generated by a single 1064 nm fiber laser are adiabatically ramped on. The lattices are calibrated by applying a 12.5 μs pulse

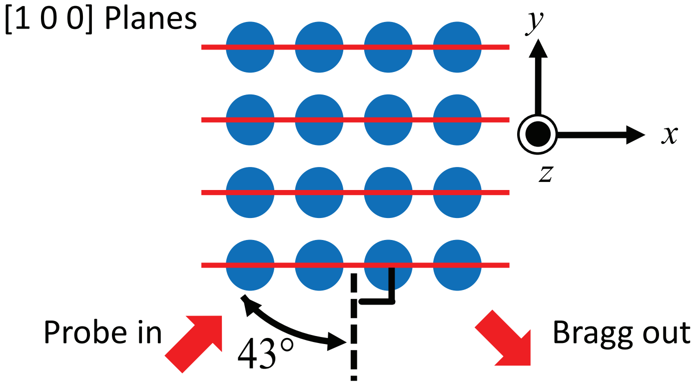

Figure 3-1: Bragg scattering schematic setup. The atoms are arranged in a cubic lattice structure with spacing of 532 nm, and the probe beam is a laser at a wavelength of 780 nm, close to one of the rubidium transition lines. The thin red lines indicate the [1 0 0] planes of the lattice.

and measuring the Kapitza-Dirac diffraction of the atoms and comparing this to theory. The system typically contains about 10^5 atoms, which leads to up to 5 atoms per lattice site. The Bragg reflected light is detected on a CCD camera which images along a direction which satisifies the Bragg condition.

The Bragg scattering condition for a three-dimensional cubic lattice is given by

$$2d \sin\theta = n\lambda_p \tag{3.1}$$

where d is the spacing between lattice planes, θ is the angle between the incoming beam and the lattice planes, n is any positive integer and λ_p is the wavelength of the probe beam. For our experiment λ_p is 780 nm and d is 532 nm. With these conditions the only allowed angle θ is 47° where n is one and corresponds to Bragg reflection off the [1 0 0] plane or any equivalent plane. A schematic of the probe beam with respect to the atoms in the lattice is shown in Fig. 3-1. Since the full angular width of the Bragg scattered light is small (measured to be $4.1 \pm 0.4°$), a precise alignment of the incident beam had to be performed at the 1/min repetition rate of the experiment. In contrast, in one and two dimensions, diffractive light scattering occurs at any angle of incidence, as recently shown with atoms in a two-dimensional optical lattice [114].

The probe beam at the Bragg angle had a typical power of 0.3 mW and beam diameter of 300 μm, large enough to illuminate the entire atomic cloud, and was detuned from the $5^2S_{1/2}, F = 2 \rightarrow 5^2P_{3/2}, F' = 3$ cycling transition of ^{87}Rb by a few natural linewidths, where the natural linewidth Γ is 6 MHz. The detuning needs to be sufficient so that the light traverses the entire atom cloud. Although the absolute signal varies with the detuning, the conclusions reached in this Letter appear not to depend strongly on the amplitude or sign of the detuning. The probe beam was applied for a few microseconds, enough to obtain a signal but short enough to avoid heating effects.

In the following subsection I describe how we characterized and determined the optimum parameters for the Bragg beam.

3.1.1 Characterization of Bragg Scattering

In this subsection I elaborate on how we characterized our Bragg scattered light so that we obtained the optimum signal to study atomic dynamics and many-body effects.

A schematic of the optics setup for the Bragg beam is shown in the top of Fig. 3-2. We use a guide mirror at the focal point of our telescope system, which adjusts the incident angle of the Bragg probe upon our atom cloud while keeping the beam aligned on the atoms at all angles. The exact angle required to achieve Bragg scattering between the incident probe beam and the atoms in the lattice is determined by the Bragg condition, but in reality due to the finite size of the sample, there is a range of angles that will still lead to Bragg scattering. Thus we characterized the range of angles that will give Bragg scattering and optimized our alignment to maximize our signal. We accomplished this by scanning the guide mirror angles.

The Bragg scattered light as a function of the vertical and horizontal alignment of the guide mirror are given in the bottom of Fig. 3-2. The mirror mount is a Thorlabs KM200, which has 1/4"-80 adjuster screws with a resolution of 5 mrad (0.3°) per revolution. If we use the full width half maximum (FWHM) of our signal with -500 counts being the background, the vertical FWHM is 1150° and the horizontal FWHM

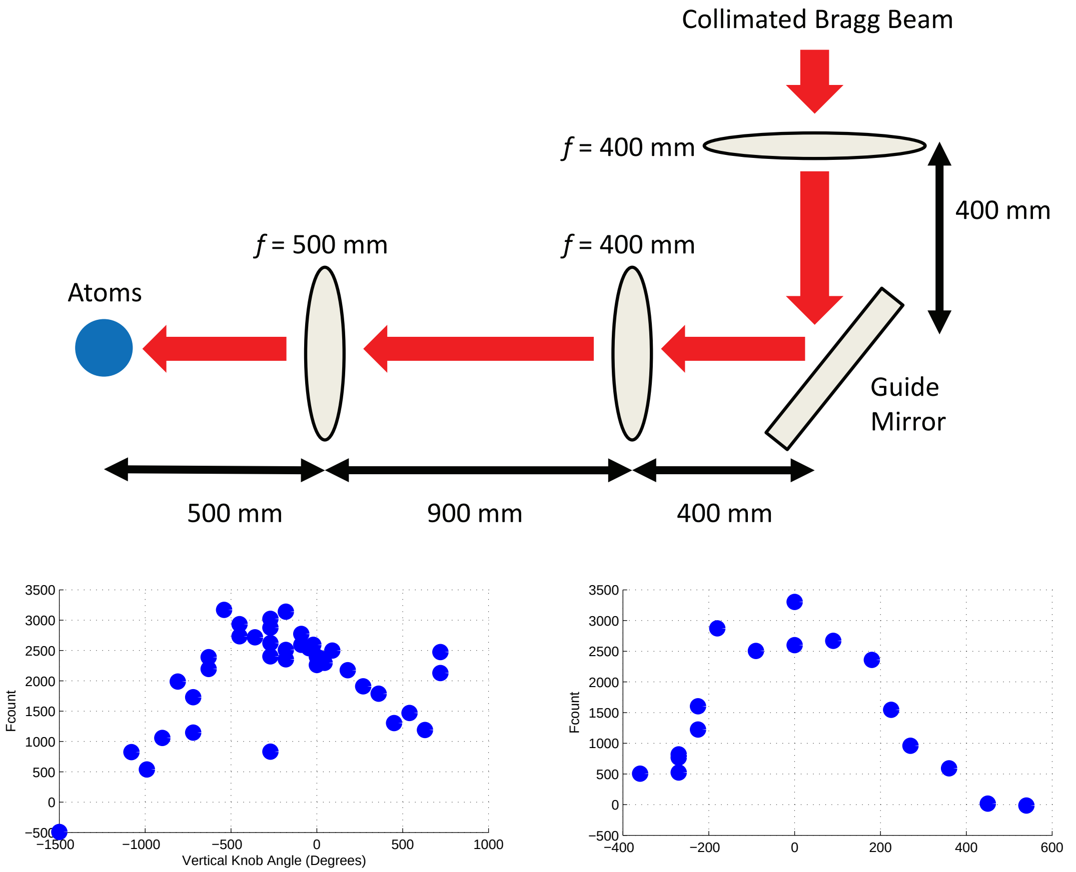

Figure 3-2: Bragg reflection as a function of the guiding mirror screw angle. Top: schematic for the optics setup for our Bragg beam. Bottom: plots of Bragg scattered light vs. the vertical (left) and horizontal (right) alignment of the guide mirror. With the known screw specifications, these correspond to a FWHM angular extent of 0.9° and 0.3° respectively. This agrees well with simple estimates of these values as described in the text.

is 400° in adjuster screw angles, which correspond to 0.9° and 0.3° respectively in true beam angles. Note the relationship $\theta \sim \lambda/2d$, where θ is the angular extent of the cloud, λ is the laser wavelength, and d is the spatial extent of the cloud [113]. From this we have $\theta_H/\theta_V = d_V/d_H$, where θ_H and θ_V are the angular extent in the horizontal and vertical directions respectively and d_H and d_V are the spatial extent in the horizontal and vertical directions respectively. From our trap geometry, we expect this to be $d_V/d_H = 1/3$, and experimentally we find that $\theta_H/\theta_V = 0.3°/0.9° = 1/3$, giving good agreement.

The detuning of the Bragg beam from the atomic resonance is an important parameter. If the beam is too close to resonance, then the atom cloud will be opaque to the beam, and the entire cloud cannot coherently scatter at the same time and simply lead to fluorescence as well as re-absorption by other atoms. On the other hand, if the beam is detuned too far, the atoms will not interact sufficiently strongly and will not lead to any scattering, coherent or incoherent. Thus the detuning must be chosen far enough so that the Bragg beam penetrates the entire cloud, but not so far that the atoms do not scatter much of the Bragg beam. We determined experimentally that we see no Bragg scattering lower than 4Γ detuning, where $\Gamma = 6$ MHz is the natural linewidth of the rubidium D2 line. At 8Γ, we see Bragg reflection but little fluorescence. Therefore the optimum initial setting for searching for Bragg reflection is 6Γ detuning, so that we have fluorescence to guide the eye, but the Bragg signal is observable if the Bragg condition is satisfied.

The optical power in the Bragg beam is another important parameter for much the same reason as how the detuning is important if we are to obtain the strongest signal in the shortest amount of time possible. For example, if the power is too low, not enough photons are scattered. Thus we measured the Bragg reflection by varying the power in the Bragg beam, and a representative response is shown in Fig. 3-3, where the probe was on for 3 μs and the detuning was 8Γ. We see that the optimum power for observing the maximum Bragg reflection in this case is at around 0.8 mW.

The duration that the Bragg probe is turned on is also a relevant parameter to obtain the best signal. The longer the beam is on, the more Bragg scattering will happen, until the atoms have scattered enough photons to be ejected from the ground state of the lattice at which point all of the Bragg scattered light obtainable has been obtained. This plateau behavior is shown in Fig. 3-4. We see that the optimum probe time is at about 5 μs where the Bragg signal reaches a limit.

We also determined the spatial extent of the Bragg scattered beam. This was done by positioning a razor blade perpendicular to the beam path and partially blocking the beam. This works because the Bragg reflection is expected to produce a fairly well collimated beam. The schematic of the setup and data are shown in Fig. 3-5. From the spatial extent of the beam, we can deduce the angular width of the beam

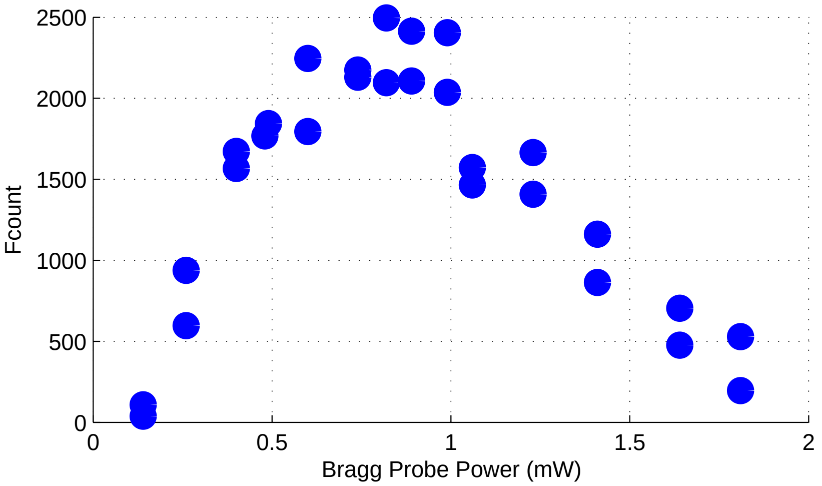

Figure 3-3: Bragg scattering as a function of Bragg probe power. For this case of 8Γ detuning, the maximum Bragg reflection is at about 0.8 mW.

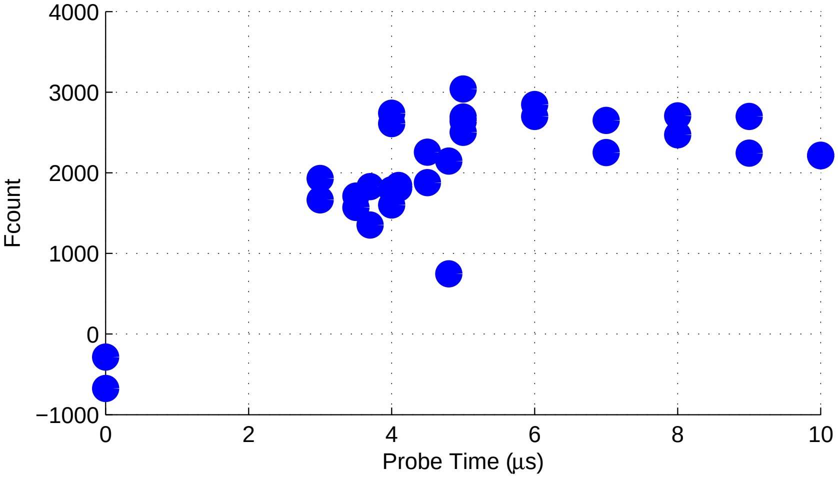

Figure 3-4: Bragg scattering as a function of Bragg probe time. For this case of 8Γ detuning, we see that the Bragg signal reaches a plateau at about 5 μs.

coming from the atom cloud. A fit of the data to an error function gives the width to be 4.5 mm and using the fact that the imaging lens has $f = 125$ mm, the half angular size of the beam is 2.0°. This is in rough agreement with our estimate given by $\theta \sim \lambda/2d$ where λ is the wavelength of the Bragg probe and d is the spatial extent of the cloud [113]. If we take the cloud size to be 10 μm and the $\lambda = 780$ nm, we have $\theta \sim 0.039$ radians, or 2.2°, which is in rough agreement with our measurement.

With the optimum parameters that maximize our signal from the Bragg beam, we have studied properties of atoms in a three-dimensional optical lattice.

3.2 Debye-Waller Factor and Bragg Scattering

As the lattice is increased the Bragg reflected signal increases as expected from the crystal ordering and tighter localization of the atoms (Fig. 3-6). For this data, the lattice in the z direction, which is also the direction of gravity, was ramped to $15E_{\mathrm{R}}$, where $E_{\mathrm{R}} = h^2/(2m\lambda_L^2)$ is the recoil energy, h is the Planck constant, m is the mass of ^{87}Rb and $\lambda_L = 1064$ nm is the lattice laser wavelength. Simultaneously the lattices in the horizontal directions were ramped to various lattice depths. Note that for our geometry the Bragg reflected intensity is insensitive to the lattice depth in the z direction because Bragg scattering occurs only in the horizontal xy plane, as we discuss later.

The scattering of light by a collection of atoms can be modeled in the following way. In the limit of low probe intensity and low optical density of the cloud, the Born approximation can be used. Then the scattering cross-section $d\sigma/d\Omega$ can be written as a product of one-dimensional Debye-Waller factors where

$$\frac{d\sigma}{d\Omega} \propto \prod_i \exp\left[-\frac{(\Delta r_i)^2 K_i^2}{2}\right], \tag{3.2}$$

where $i = x, y, z$ is the index for the three dimensions, K_i is the magnitude of the i-th component of $\mathbf{K}$ where $\mathbf{K} = \mathbf{k}_{\mathrm{in}} - \mathbf{k}_{\mathrm{out}}$ is the difference between the incoming probe beam and Bragg scattered wavevectors, and $\Delta r_i = \sqrt{\hbar/(m\omega_i)}$ is the harmonic

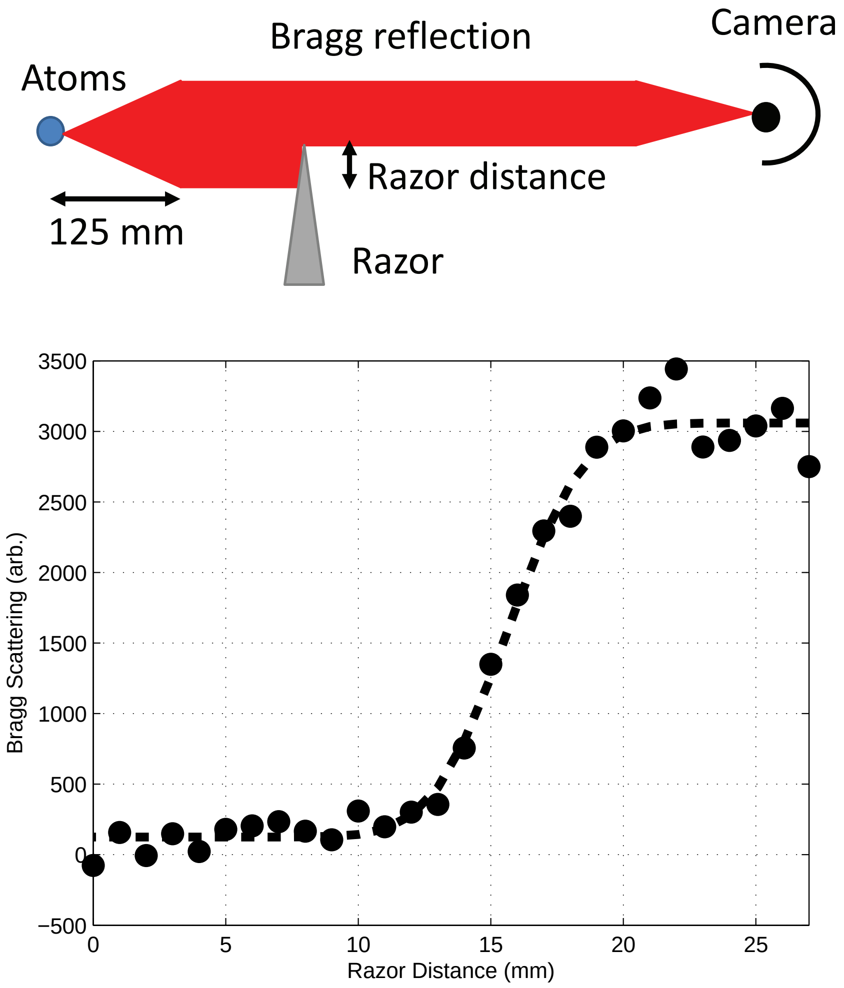

Figure 3-5: Bragg reflection as a function of razor position. Top is the experimental setup. Bottom is the Bragg scattered signal as a function of razor position at 8Γ detuning. From the error function fit, the width is about 4.5 mm. With an imaging lens of $f = 125$ mm, this corresponds to an angular extent of 2.0°. This is in rough agreement with an estimate of 2.2°.

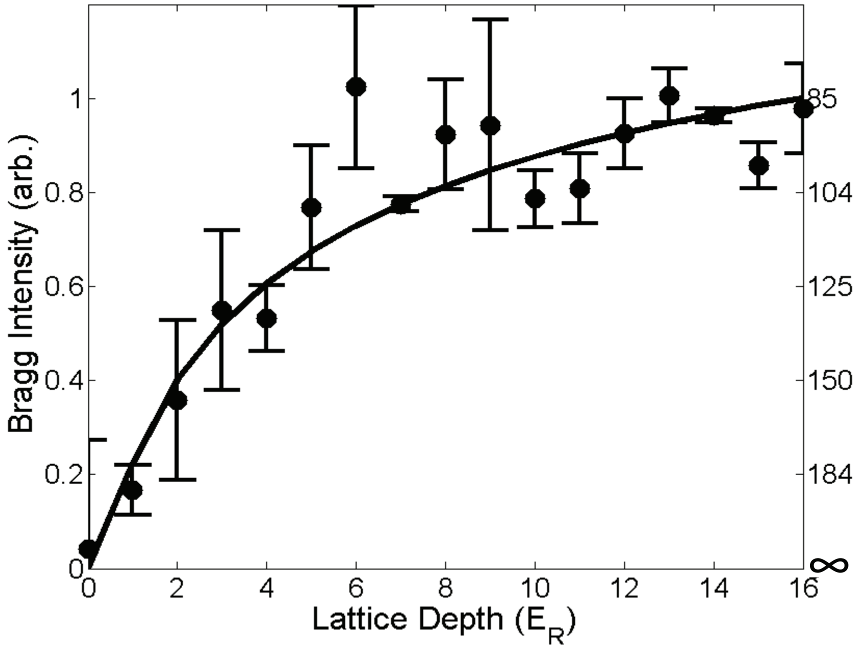

Figure 3-6: Bragg scattering as a probe of the spatial wavefunction width. The plot shows Bragg scattered intensity vs. lattice depth in units of the recoil energy. The right axis gives the corresponding root-mean-square width of the wavefunction squared. The solid line is a no-free-parameter curve given by the Debye-Waller factor. Error bars are statistical.

oscillator width where $\hbar$ is the reduced Planck constant and ω_i is the trap frequency in the i-th direction, which depends on the optical lattice depth. The atoms are approximated as gaussian wavefunctions, which is a good approximation for sufficiently large lattice depths. However, we find that even for low lattice depths where significant superfluid components are expected, this approximation describes the Bragg scattered signal well.

For our experimental conditions, $K_z = 0$ because Bragg scattering occurs in the horizontal xy plane. The lattice depths are controlled in a way such that they are the same in both the x and y directions which leads to $\Delta x \equiv \Delta r_x = \Delta r_y$. This simplifies the scattering cross-section to

$$\frac{d\sigma}{d\Omega} \propto \exp\left[-\frac{(\Delta x)^2 K^2}{2}\right]. \tag{3.3}$$

Thus Bragg scattering allows the study of the spatial extent of the atomic wavefunction.

The data can be compared to a no-free-parameter theoretical line, assuming non-interacting atoms. The Bragg scattered intensity $B(N_L)$ as a function of lattice depth N_L can be written as

$$B(N_L) \propto \exp\left[-\frac{\lambda_L^2 K^2}{8\pi^2\sqrt{N_L}}\right]. \tag{3.4}$$

Both the harmonic oscillator width Δx, which depends on the mass of the rubidium atom and trap frequency, and change in wavevector K are known. This theoretical line and the data is shown in Fig. 3-6 and we see good agreement. Thus the Bragg scattered light as a function of lattice depth can be well-described by a model where the atoms are assumed to be non-interacting gaussian atomic wavefunctions whose spatial width is determined by the lattice depth.

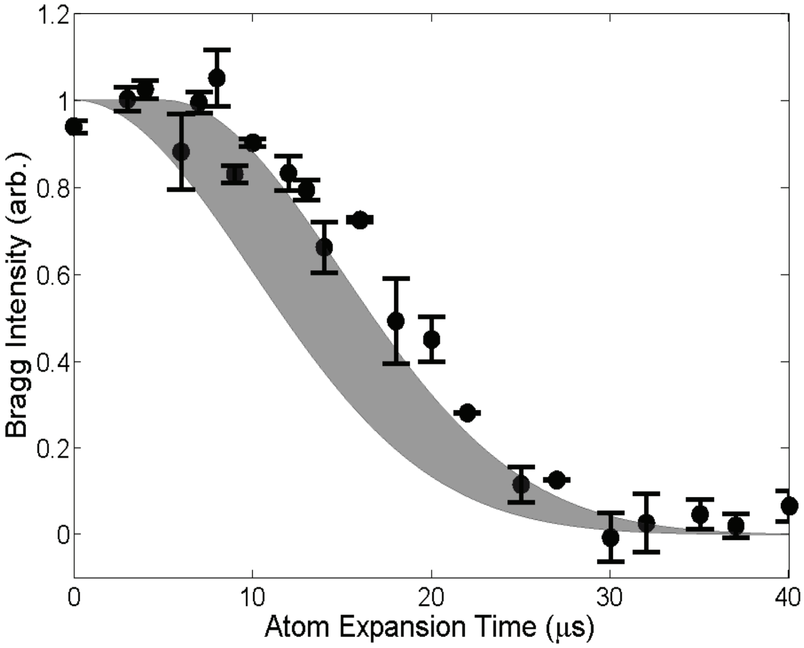

Figure 3-7: Bragg scattering as a probe of the momentum wavefunction width. The plot shows Bragg scattered intensity vs. the free-expansion time of the atoms after rapidly turning off the lattices from $15E_\mathrm{R}$. The decay in signal indicates a melting of the crystal structure, or in other words spreading of the atomic wavepacket with a given momentum uncertainty. The gray area is a no-free-parameter curve using the Debye-Waller factor taking into account the probe pulse duration of 5 μs. Error bars are statistical.

3.3 Heisenberg-Limited Wavefunction Dynamics

Bragg scattering can also be used to probe the momentum width of the atomic wavefunctions. This is done by measuring Bragg reflection as a function of the expansion time of the atoms between a rapid lattice turn off and Bragg probe. In particular, the two horizontal lattices were turned off from $15E_\mathrm{R}$ to $0E_\mathrm{R}$ in less than 1 μs and the lattice in the z direction was kept at $15E_\mathrm{R}$. Turning off the lattices allows the atomic wavepackets in each individual lattice well to expand freely in those directions. The data in Fig. 3-7 shows that the signal has decayed in 30 μs. The time it takes to lose crystal structure is roughly the time it takes for the atoms to move over half of a lattice distance.

The Debye-Waller factor can be used to determine more precisely how the Bragg reflection should behave as a function of the expansion time with no free parameters, assuming gaussian atomic wavepackets. This makes use of the well-known time-dependent behavior of a Heisenberg-limited gaussian wavepacket in free space which can be written as

$$(\Delta x(t))^2 = (\Delta x)^2 + \frac{(\Delta p)^2 t^2}{m^2} \tag{3.5}$$

where Δx and Δp are the uncertainty of position and momentum respectively at the initial time and t is the expansion time [87]. In a previous paper where the atoms were not quantum degenerate, the momentum distribution was assumed to be determined by temperature [113]. The results of our work show that the momentum uncertainty is Heisenberg-limited, meaning $(\Delta x)^2(\Delta p)^2 = \hbar^2/4$, so the Bragg scattered light $B(t)$ as a function of expansion time can be written as

$$B(t) \propto \exp\left[-\frac{(\Delta p)^2 K^2 t^2}{2m^2}\right]. \tag{3.6}$$

This curve is shown in Fig. 3-7. The curve is broadened by taking into account the probe beam duration which was 5 μs and shows good agreement with data. This analysis shows that by releasing the atoms from a lattice, we can directly probe the *in situ* time evolution of the ground state atomic wavefunctions with spatial extent of tens of nanometers. Furthermore, the atomic spatial and momentum widths are seen to be Heisenberg-limited.

3.4 Superfluid Revivals of Bragg Scattering

Coherent many-body non-equilibrium dynamics can also be studied with Bragg scattering after a sudden release of the atoms from the optical lattice in three dimensions. At low lattice depths the Bragg scattered signal shows revivals as a function of expansion time because of the rephasing of the superfluid atomic wavefunctions that were originally confined in the lattices. Therefore, these revival signals should give a measure of the superfluid order parameter. Furthermore, the revivals are analogous to the optical Talbot effect, whose atomic version was observed previously for a thermal beam [16] and for a quantum degenerate gas in the temporal domain [28]. Here we observe the atomic Talbot effect for an interacting quantum degenerate gas in a three-dimensional optical lattice. Revivals can be seen in Fig. 3-8 and become less pronounced as the lattice depth increases.

In particular, the characteristic revival time is determined by

$$\tau = \frac{h}{\frac{\hbar^2(2k)^2}{2m}} \tag{3.7}$$

and is 123 μs for our parameters, where $2k$ corresponds to the wavevector of the matter wave. However, with Bragg scattering we expect the first revival at half that time of 61 μs, which is what we observe in Fig. 3-8. This can be understood by realizing that the atomic wavepackets need only travel half the lattice spacing to constructively interfere with the wavepackets traveling in the opposite directions from the nearest neighbor sites.

3.5 Superfluid to Mott Insulator Through Bragg Scattering

The superfluid coherence as a function of lattice depth can be studied by comparing the Bragg reflected signal when the atoms are in the optical lattice to the signal at the first revival. The revival signal as a function of lattice depth is shown in Fig. 3-9, where the superfluid to Mott insulator transition is expected to occur around $13E_{\mathrm{R}}$ [42]. In a non-interacting system without any dissipation, one would expect complete revivals. On the other hand, in the Mott insulating phase where phase coherence has been lost, revivals should completely disappear, except for a very weak signal at intermediate lattice depths due to particle-hole correlations [38].

To understand the measured revival decay, we have numerically studied the one-dimensional Gross-Pitaevskii equation that assumes interacting matter waves at zero temperature. The simulations show that interactions and finite size effects have neg-

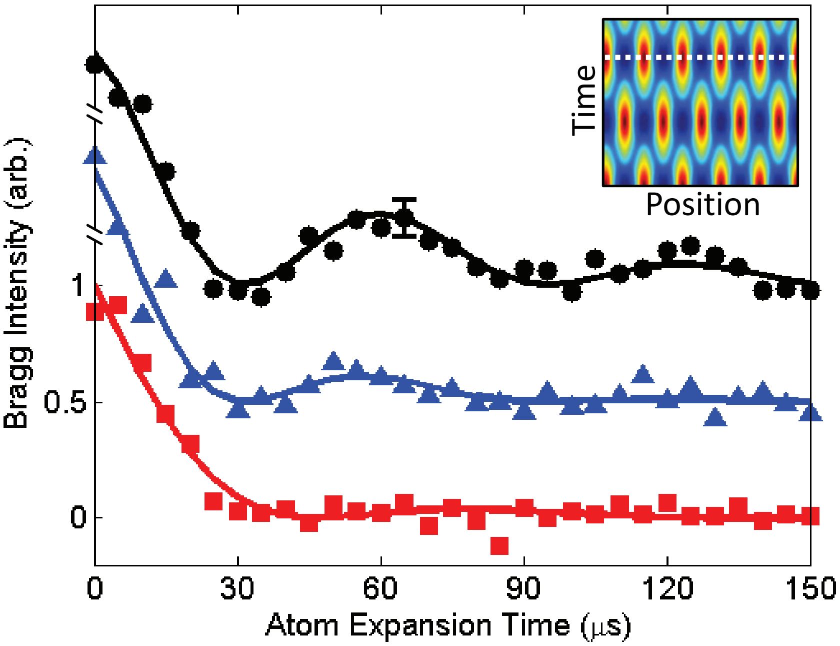

Figure 3-8: Revivals of Bragg scattered light. The plot shows the Bragg scattered intensity vs. the expansion time in three dimensions for three different initial lattice depths: $5E_{\mathrm{R}}$ (circles), $8E_{\mathrm{R}}$ (triangles), and $15E_{\mathrm{R}}$ (squares). Each data set is normalized to the Bragg intensity at the initial time. Revivals at lower lattice depths indicate coherence of the atoms across multiple lattice sites. The lines are phenomenological fits to exponentially decaying sine waves. Different lattice depth data are offset for clarity and the error bar is represenative. Inset is a solution to the one-dimensional Gross-Pitaevskii equation with experimental parameters and an initial state of a chain of gaussian wavefunctions, showing the revivals of the density distribution as a function of time. The white dotted line represents the revival time.

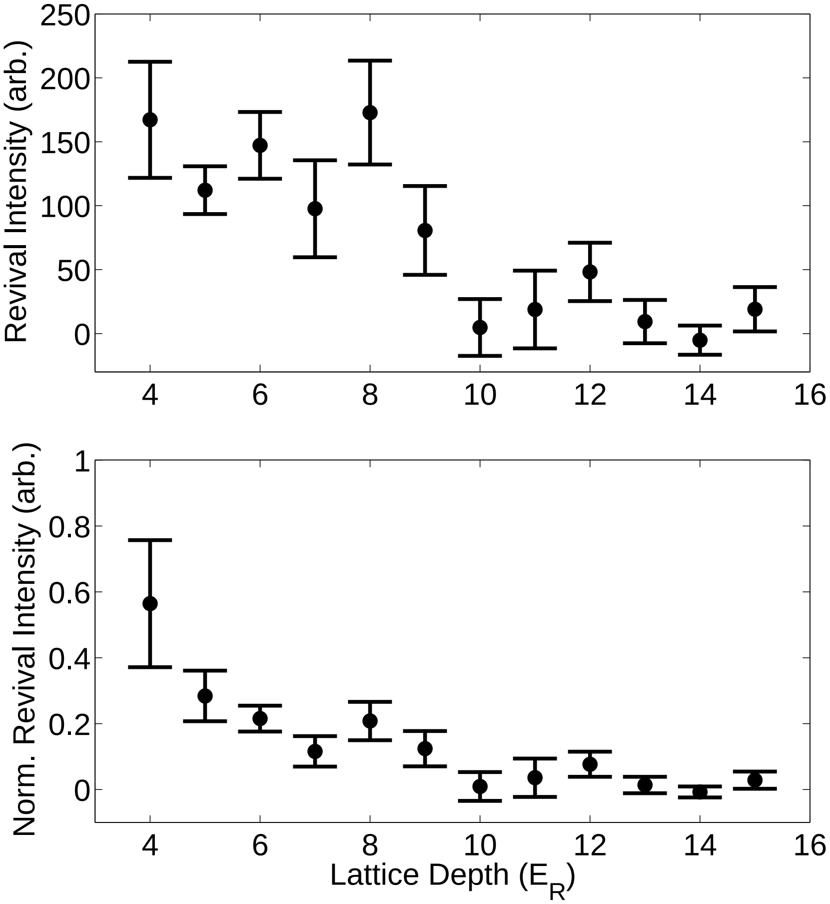

Figure 3-9: Bragg scattering revival as a probe of superfluid coherence. Top: Bragg scattered revival signal at 60 μs vs. lattice depth. Bottom: The top plot normalized to the Bragg scattered signal without expansion. We see a decrease in revival, and consequently superfluid coherence, as the lattice is increased. Error bars are statistical.

ligible effect on the decay of revivals. Empirically, randomizing the phase between neighboring sites reduces the revival fraction. The loss of phase coherence across lattice sites could be due to factors such as temperature, beyond Gross-Pitaevskii equation effects, or technical factors. We have considered quantum depletion [118], but the calculated depletion fraction at $5E_{\mathrm{R}}$ is 2%, too low to account for the observed decay. Future work should provide a more complete picture of the decay of revivals.

Note that Bragg scattered revivals are complementary to the observation of diffraction peaks in time-of-flight absorption images [42]. Both are based on matter-wave interference due to superfluid coherence: revivals at short expansion times and diffraction at long expansion times. Diffraction is a far-field effect only possible for finite size samples, whereas revivals are a near-field bulk effect. The order of the revival or the angular resolution of the diffraction peaks determine whether these techniques probe short-range or long-range spatial coherence. Further studies are needed to determine which technique is more sensitive to certain aspects of the superfluid to Mott insulator transition.

In this work we have not focused on the effects of occupation number on Bragg scattering. In principle the atomic wavefunctions are more extended for higher occupation numbers, but this effect is small for our parameters. However, light scattering at higher occupation numbers will have an inelastic component due to colliding atoms or photoassociation [34]. The dependence of Bragg scattering on lattice depth suggests that these effects are not dominant.

To examine this, we measured the Bragg reflection by varying the lattice ramp up time, where the ramp up was up to $15E_R$. The Bragg reflection was essentially unaffected by the ramp up time down to 1 ms, where we do not necessarily expect the lattice ramp up to be adiabatic and therefore could expect the occupation number of the atoms to be randomly distributed. This shows that the Bragg reflection is simply a manifestation of the underlying crystal ordering, and does not depend strongly on the exact filling of the atoms in the optical lattice.

3.6 Conclusions

After Bragg scattering has been established as a probe for Mott insulators, it can now be applied to study other types of quantum phases such as antiferromagnetic ordering in both the occupation number and spin sectors [21, 93]. Although temperatures required to realize spin ordering are on the order of tens to hundreds of picokelvins, recent experimental results suggest a way forward to lower the temperature of a two-component Mott insulator [76].

To detect spin ordering such as the antiferromagnetic state, we need spin-dependent Bragg scattering. Since spins in an ultracold atom context will be different hyperfine states, by choosing an appropriate wavelength of the Bragg beam one can scatter selectively from a chosen state as well as scatter in a spin independent way [21]. Thus Bragg scattering will allow experimentalists to probe both density and spin ordering by varying the Bragg beam wavelength.

In conclusion, we have observed Bragg scattering of near-resonant photons from a quantum degenerate Bose gas in a three-dimensional optical lattice. We have shown that this technique probes not only the periodic structure of the atoms, but also the spatial and momentum width of the localized atomic wavefunctions and the superfluid coherence.

Chapter 4

Raman-Assisted Tunneling and the Harper Hamiltonian

Ultracold atoms in optical lattices have ushered in an era of unprecedented controllability, tunability, and flexibility in the study of strongly-correlated many body physics, both experimentally and theoretically [13, 70, 42]. Here we propose and experimentally study a scheme where one can experimentally realize the Harper Hamiltonian with ultracold atoms in optical lattices. The Harper Hamiltonian was described in section 2.5, and is expected to give rise to a fractal band structure called the Hofstadter butterfly [52], shown in Fig. 2-7, mimicing solids in extremely high magnetic fields of order one billion gauss. Once interactions are included, the Harper Hamiltonian is believed to give rise to fractional quantum Hall states, which would allow the experimental study of fascinating topological phases of matter [94, 48].

We have emphasized how ultracold atomic systems can simulate the behavior of electrons in solid state materials. However many interesting effects, such as the integer and fractional quantum Hall effects [107, 68], occur when a solid is placed in an external magnetic field. Due to the charge neutrality of ultracold atoms, one cannot directly apply a magnetic field to a cold atom system and expect a similar response as an electron in a solid. Despite this seeming limitation, there are ways to create effective magnetic fields which lead to Hamiltonians as if the atoms were moving in a magnetic field with an effective charge. The method initially realized by experimentalists was to physically rotate the atomic cloud to genereate rotational velocity, which then acted as an effective magnetic field giving rise to quantized vortices in bulk Bose-Einstein condensates [74, 1]. The seminal work by Ian Spielman's group [72] realized effective magnetic fields by taking advantage of Raman transitions between different hyperfine states, thus paving the way for optical realizations of effective magnetic fields.

Other methods to generate artificial gauge fields have been proposed by Jaksch and Zoller [59] and Gerbier and Dalibard [37], which involve Raman transitions but now in an optical lattice geometry. Both schemes envision a two-component system, where the lattices of the two components are offset by half a lattice spacing. The Raman transitions induce tunneling between the two sub-lattices, in the process imprinting a position-dependent phase.

Furthermore, there have been experimental realizations of a spatially-independent phase by the Sengstock [101] and Spielman groups [60], as well as a staggered flux arrangement by the Bloch group [3]. The Sengstock group realizes their phase by a particular type of lattice phase modulation, the Spielman group uses Raman transitions and radiofrequency magnetic fields, and the Bloch group uses a superlattice in conjunction with Raman beams. Although all three results have led to new insights into the nature of phases in ultracold atomic systems, they have limitations if one is hoping to reach high enclosed fluxes per unit cell. In particular, the Sengstock and Spielman approaches as it is only create a spatially-independent phase, which does not give rise to any enclosed flux. In the Bloch approach, because the superlattice can only create a staggered flux arrangement, no globally macroscopic enclosed flux is possible. In all three of these cases, rectification of the fluxes to create a spatially varying flux seem to be in principle possible, but the proposed schemes involve many more laser beams and requires further complexity in the experimental arrangement. In contrast, our proposed technique involves only two lattice laser beams and two running wave Raman beams and a single spin state of bosonic ^{87}Rb, which is significantly more simple than the other proposed schemes and should allow access to any desired enclosed flux with simple modifications to the experimental geometry.

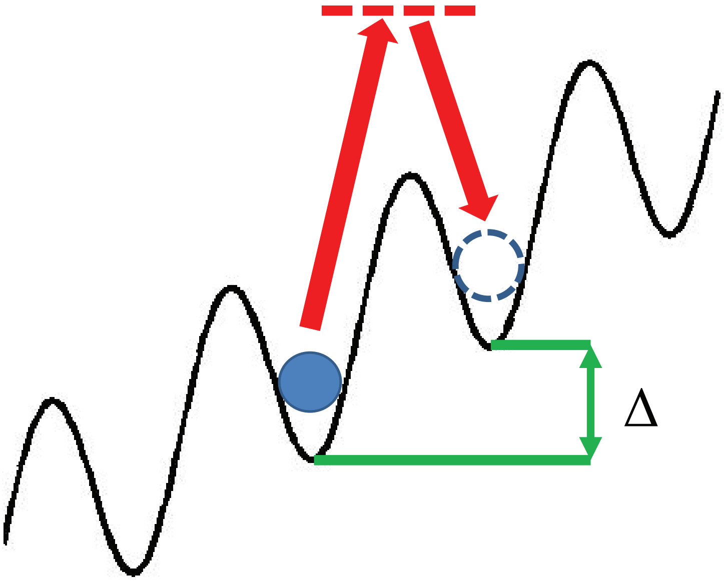

Figure 4-1: Schematic of a tilted lattice and Raman beams to create artificial gauge fields. The tilt induces an energy offset Δ between neighborin sites. Then Raman beams that are frequency detuned by exactly Δ can cause transitions between localized states in nearest neighbors. Furthermore, this tunneling can have a position-dependent phase which gives rise to topologically non-trivial ground states.

Our proposal involves realizing the topologically non-trivial Harper Hamiltonian by creating a two-dimensional optical lattice with a linear potential gradient along one of the lattice directions. As it is, this tilted potential causes a suppression of resonant tunneling along the tilt direction and only allows resonant tunneling along the direction perpendicular to the tilt. Then on top of that two laser beams are applied which are frequency detuned to precisely match the energy offset caused by the linear potential. Then these two laser beams are able to induce a Raman transition between a localized state in one lattice site to a nearest neighbor lattice site in the tilt direction, effectively flattening out the tilt. Thus we call these two beams our Raman beams. Crucially, in addition to restoring tunneling, these running wave Raman beams can imprint a position-dependent phase on the atoms, which then results in the Harper Hamiltonian. A schematic of this setup is shown in Fig. 4-1. Note that the tilt can be created by any physical mechanism which creates a linear potential gradient, including gravity and magnetic field gradients.

In the rest of this chapter, I will describe in more detail the theoretical underpinnings of the scheme, as well as present experimental results which give indications that we have successfully created the Harper Hamiltonian. However, thus far we have been unable to observe direct signatures of the ground state of the Harper Hamiltonian, namely superfluid interference peaks corresponding to the band structure of the Harper Hamiltonian.

4.1 Raman-Assisted Tunneling in the Perturbative Limit

Modification of tunneling in an optical lattice system by dynamical modulation of the lattice have been explored by other groups, notably the Arimondo and Tino groups in Italy [71, 92, 56, 6, 5, 103]. Our proposed Raman beams are in the same spirit, since two laser beams which induce a Raman transition can be thought of as a travelling wave optical lattice.

In particular, two Raman lasers with wavevectors $\mathbf{k}_1$ and $\mathbf{k}_2$ and lattice depth V_K can induce tunneling through a time-dependent potential

$$\begin{aligned} V_K(\mathbf{r},t) &= V_K \cos^2(\mathbf{q}\cdot\mathbf{r} - \omega t/2) && (4.1)\\ &= V_K \frac{1+\cos(2\mathbf{q}\cdot\mathbf{r} - \omega t)}{2} && (4.2)\\ &= \frac{V_K}{4}\left(1 + e^{i(2\mathbf{q}\cdot\mathbf{r}-\omega t)} + e^{-i(2\mathbf{q}\cdot\mathbf{r}-\omega t)}\right) && (4.3)\\ &= \frac{V_K}{4}\left(1 + e^{i(\delta\mathbf{k}\cdot\mathbf{r}-\omega t)} + e^{-i(\delta\mathbf{k}\cdot\mathbf{r}-\omega t)}\right), && (4.4) \end{aligned}$$

where ω is the frequency detuning between the two Raman beams, $2\mathbf{q} = \delta\mathbf{k}$, $\delta\mathbf{k} = \mathbf{k}_1 - \mathbf{k}_2$, and $\mathbf{q} = (\mathbf{k}_1 - \mathbf{k}_2)/2$.

Let us assume that the linear tilt exists in the x direction with an energy offset between nearest neighbor lattice sites of Δ and that the detuning of the Raman beams is exactly Δ. Then in the perturbative limit of $V_K \ll \Delta$ and in the rotating wave approximation, the laser-assisted tunneling term can be written

$$
\begin{aligned}
K &= \frac{V_K}{4}\int d^2 r w^*(\mathbf{r}-\mathbf{R})w(\mathbf{r}-\mathbf{R}-\mathbf{d}_x)e^{-i\delta\mathbf{k}\cdot\mathbf{r}} && (4.5)\\
&= \frac{V_K}{4}\int d^2 r w^*(\mathbf{r})w(\mathbf{r}-\mathbf{d}_x)e^{-i\delta\mathbf{k}\cdot(\mathbf{r}+\mathbf{R})} && (4.6)\\
&= e^{-i\delta\mathbf{k}\cdot\mathbf{R}}\frac{V_K}{4}\int d^2 r w^*(\mathbf{r})w(\mathbf{r}-\mathbf{d}_x)e^{-i\delta\mathbf{k}\cdot\mathbf{r}} && (4.7)\\
&= e^{-i\delta\mathbf{k}\cdot\mathbf{R}}\frac{V_K}{4}\int dx w^*(x)w(x-d_x)e^{-i\delta k_x x} && (4.8)\\
&\qquad\qquad \times\int dx w^*(y)w(y)e^{-i\delta k_y y} && (4.9)\\
&= K_0 e^{-\delta\mathbf{k}\cdot\mathbf{R}}, && (4.10)
\end{aligned}
$$

where $K_0 = V_K/4\int d^2 r w^*(\mathbf{r})w(\mathbf{r}-\mathbf{d}_x)e^{-i\delta\mathbf{k}\cdot\mathbf{r}}$, and $w(\mathbf{r}) = w(x)w(y)$ where $w(x)$ is the Wannier-Stark state due to the linear tilt in the x direction and $w(y)$ is the Wannier function. The position-dependent phase which gives rise to the Harper Hamiltonian is embodied in the factor $\delta\mathbf{k}\cdot\mathbf{R}$. I plot the absolute value of the relevant overlap integrals present in the Raman-assisted tunneling expression in Fig. 4-2. The overlap integrals teach us something interesting about the requirements to achieve position-dependent phases under realistic conditions.

We see that the overlap integral involving the Wannier-Stark states in the tilt direction exhibits oscillatory behavior. In particular, we learn that there must be a non-zero momentum transfer in the tilt direction for the Raman-assisted tunneling to be strong enough to induce tunneling. This is an important point, since from phase accumulation considerations, all one needs is momentum transfer in the direction orthogonal to the tilt. Thus to get position-dependent phase which gives rise to non-zero enclosed flux and a sizable tunneling amplitude, the Raman beams must transfer momentum along both the direction of the tilt and orthogonal to it.

Note that V_K can be related to the two-photon Rabi frequency of the two Raman lasers, which is also related to the one-photon Rabi frequency of the individual lasers. Knowing the precise relationship between the lattice depth and two-photon Rabi frequency is important when we calibrate the strength of our Raman beams by

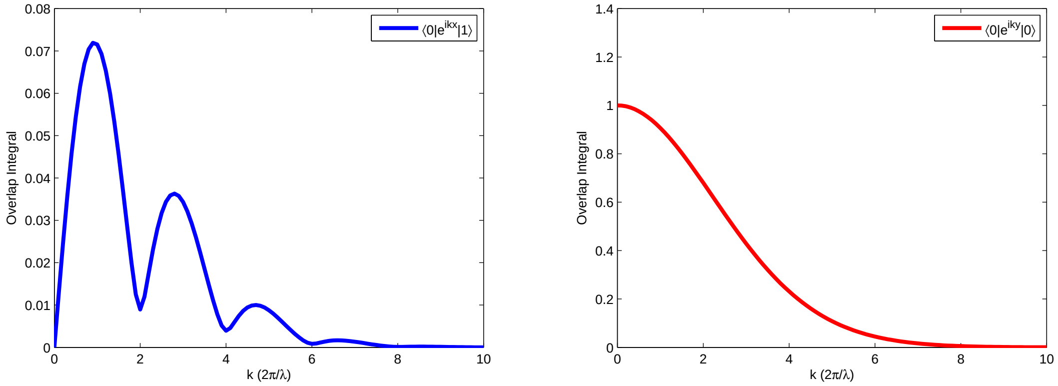

Figure 4-2: Overlap integrals for perturbative Raman coupling. The integral in the x direction is done with Wannier-Stark states and the integral in the y direction is done with Wannier states.

measuring the two-photon Rabi oscillation frequency between states with momentum $\mathbf{0}$ and $\mathbf{k}_1 - \mathbf{k}_2$.

The two-photon Rabi frequency Ω_{R2} is given as [59]

$$\Omega_{R2} = \frac{\Omega_{Rg}\Omega_{Re}}{2\delta} \tag{4.11}$$

where $\Omega_{Rg,e}$ are the one-photon Rabi frequency of each of the Raman beams and δ is the detuning between the Raman laser and the D1 and/or D2 lines. The one-photon Rabi frequency is given by $\hbar\Omega = eE\langle e|z|g\rangle$ where e is the electron charge, E is the electric field, and $e\langle e|z|g\rangle \equiv D$ is the electric dipole moment [35]. The two-photon Rabi oscillation from the ground state $|g\rangle$ to an excited state $|e\rangle$, starting in $|g\rangle$ is given by $P_e(t) = \sin^2(\Omega_{R2}t/2)$. This means that the population transfer oscillates at frequency Ω_{R2}.

Now, the moving lattice depth V_K is given by $V_K = \hbar\Omega_{Rg}\Omega_{Re}/\delta$ [80]. This can be understood by recalling that the single traveling wave AC Stark shift is given as $\hbar\Omega_{Rg}^2/(4\delta)$. Interference of two laser beams leads to a multiplicative factor of 4. So, combining all that, the two-photon Rabi oscillation frequency Ω_{R2} is related to the

Raman lattice depth V_K as

$$V_K = 2\Omega_{R2}. \tag{4.12}$$

Note that in general K_0 is complex and so can have some non-zero phase in addition to the spatially-dependent phase give by $\delta\mathbf{k}\cdot\mathbf{R}$. But for a given configuration, the phase is not spatially dependent so is effectively a global, constant phase.

4.1.1 Energy Hierarchy to Realize the Harper Hamiltonian

Certain inequalities must be satisfied in order to realize the Harper Hamiltonian. First, the band gap ω must be larger than any other energy scale so that the atoms do not occupy higher orbital states. In particular, if the potential tilt Δ is equal to the band gap, Wannier-Stark transitions, where states in the lowest band in one lattice site become resonant with states in the first excited band in a neighboring site, will be allowed to happen, therefore destroying the requirement to be in the lowest band [45, 40]. Therefore the potential tilt Δ must be smaller than ω.

A second requirement is for the bare tunneling energy J to be smaller than the potential tilt Δ. If this condition is not satisfied, then resonant tunneling can be stronger than the light-assisted tunneling and consequently position-dependent phase upon tunneling will not manifest itself.

These two conditions lead to the following energy hierarchy,

$$J \ll \Delta \ll \omega. \tag{4.13}$$

For ^{87}Rb, the mass is 1.443×10^{-25} kg [97], and for a lattice spaced apart 532 nm, the potential tilt due to gravity is 1137 Hz. Similar tilts can also be achieved for atoms in the hyperfine state $|F = 2, m_F = -2\rangle$ with a magnetic field gradient of around 15 G/cm, which is experimentally accessible. For lattice depths of $10E_{\mathrm{R}}$, the tunneling energy J is around 45 Hz and the band gap is around 10 kHz. Thus these experimentally accessible parameters will satisfy the inequalities necessary to realize the Harper Hamiltonian.

4.2 Experimental Geometries to Realize Specific α

As shown in section 4.1, the factor $\delta\mathbf{k}\cdot\mathbf{R}$ gives rise to the non-trivial topological phase in the Harper Hamiltonian. Therefore, controlling the angle between the Raman beams and the two-dimensional lattice axes are crucial to realize the Harper Hamiltonian with a particular α. First I explore the possible α for an arbitrary Raman geometry in a square lattice, and then focus on a specific geometry which we have implemented which should give rise to $\alpha = 1/2$.

Let us consider a 2D geometry where the lattice and Raman beams are propagating in a 2D plane as in Fig. 4-3. Let the lattice be square along the x and y axes and have spacing a, so that the position vector is $\mathbf{R} = a(m\hat{x} + n\hat{y})$. Also, let the difference in k vectors of the two Raman beams k_1 and k_2 be $\mathbf{k} = \mathbf{k}_1 - \mathbf{k}_2$ so that if the angle between k_1 and k_2 is θ and $k_1 = k_2 = 2\pi/\lambda$, then $|\mathbf{k}| \equiv k = 4\pi/\lambda|\sin(\theta/2)|$. Also, in this lattice coordinates write $\mathbf{k} = k(\cos\phi\hat{x} + \sin\phi\hat{y})$. The phase is

$$\mathbf{k}\cdot\mathbf{R} = 2\pi\left|\sin\left(\frac{\theta}{2}\right)\right|(m\cos\phi + n\sin\phi) \tag{4.14}$$

$$= m\phi_x + n\phi_y, \tag{4.15}$$

where we defined $\phi_x = 2\pi|\sin(\theta/2)|\cos\phi$ and $\phi_y = 2\pi|\sin(\theta/2)|\sin\phi$. Now assume the tilt is in the x direction. Then the phase accumulated is as given in the left of Fig. 4-3. We see that the flux accumulated along one unit cell is $\Phi = \phi_y$, which corresponds to a magnetic flux per plaquette of $\alpha = \phi_y/2\pi$. If the tilt is in the y direction, then the phase accumulated is as given in the right of Fig. 4-3. We see that the flux accumulated along one unit cell is $\Phi = \phi_x$ which corresponds to a magnetic flux per plaquette of $\alpha = \phi_x/2\pi$. Thus we see that if the linear tilt is along a given direction, the total phase accumulated after one full rotation around a plaquette is given by the phase that depends on the perpendicular direction.

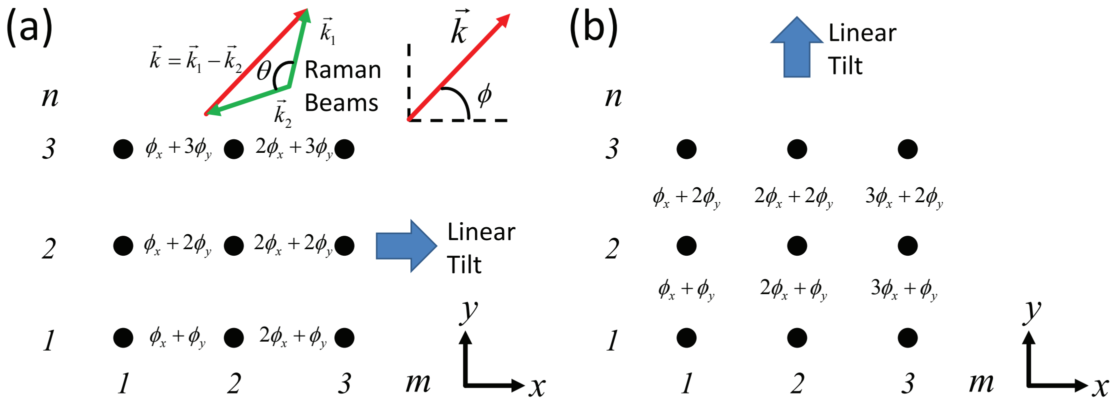

Figure 4-3: Tilt and phase accumulated for general Raman geometry. Left figure is tilt along the x direction, the right figure is tilt along the y direction. Note $\phi_x = 2\pi|\sin(\theta/2)|\cos\phi$ and $\phi_y = 2\pi|\sin(\theta/2)|\sin\phi$.

4.2.1 Experimental Geometry for $\alpha = 1/2$

Now consider the specific case where the Raman beams are copropagating along the lattice beam directions so that $\mathbf{k}_1 = 2\pi/\lambda\hat{\mathbf{x}}$ and $\mathbf{k}_2 = 2\pi/\lambda\hat{\mathbf{y}}$. A schematic is shown in Fig. 4-4. In this case, we have $\theta = 90°$ and $\phi = -45°$, so we get that

$$\mathbf{k} \cdot \mathbf{R} = \pi(m - n). \tag{4.16}$$

With a linear tilt along the x direction, the total phase accumulated around one plaquette is given by $\Phi = \pi$. This phase then corresponds to a flux density per plaquette of $\alpha = 1/2$ and will be the geometry I will be focusing on for most of the rest of this chapter.

4.3 Raman-Assisted Tunneling in the Rotating Frame

In section 4.1 we showed the effective Raman-assisted tunneling and accompanying position-dependent phase factor which gives rise to effective magnetic fields in the perturbative regime. Here I derive a more general expression for the Raman-assisted tunneling which include both the position-dependent phase and saturation of the tunneling amplitude. The effective tunneling can be solved for more general cases by

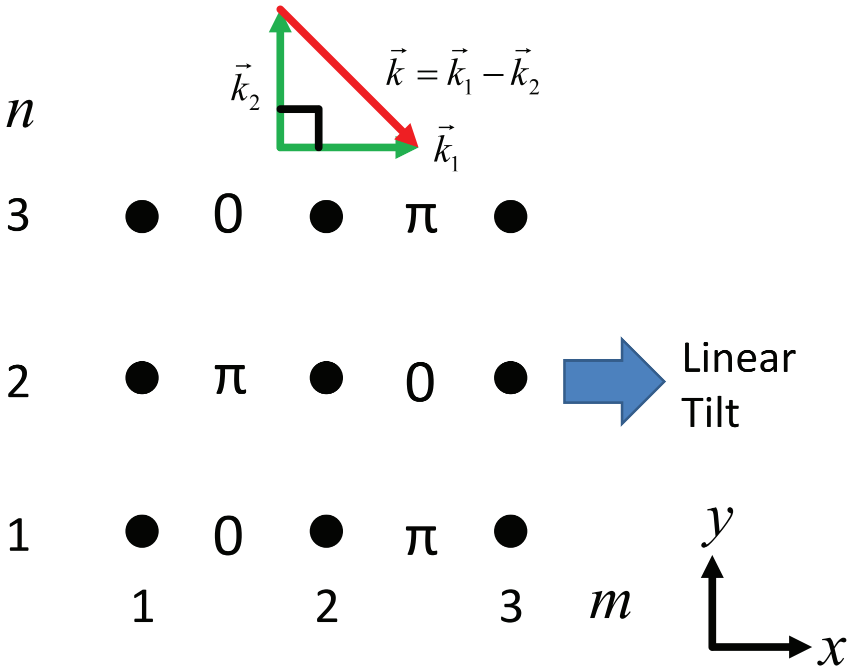

Figure 4-4: Experimental geometry for $\alpha = 1/2$. The phase accumulated along the tilt alternates between 0 and π.

rewriting the original Hamiltonian into a time-independent Hamiltonian with effective tunneling by using the rotating-wave approxiation [103].

If you have a two-dimensional system with a square 2D lattice $V_L(x, y)$ with lattice spacing a and a linear tilt with energy per lattice site of Δ in the x direction and an additional term $\mathcal{E}(x, y, t)$, we can write the Hamiltonian as

$$H = \frac{p_x^2}{2m} + \frac{p_y^2}{2m} + V_L(x, y) + \frac{\Delta}{a} x + \mathcal{E}(x, y, t). \tag{4.17}$$

This can be rewritten into a second quantized, time-dependent Hamiltonian of the form [103]

$$\begin{aligned} H = \sum_{m,n} \Delta m |m, n\rangle\langle m, n| - J_y \sum_{m,n} (|m, n+1\rangle\langle m, n| + \text{c.c.}) \\ + \sum_{m,m',n,n'} |m, n\rangle\langle m, n|\mathcal{E}(x, t)|m', n'\rangle\langle m', n'|, \end{aligned} \tag{4.18}$$

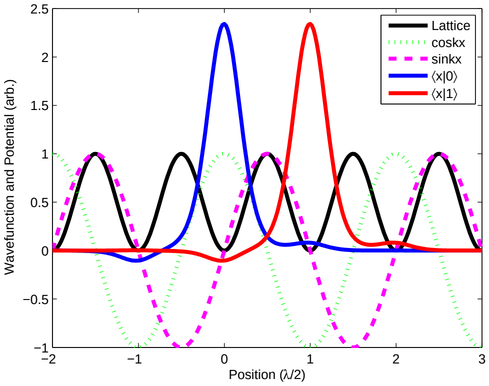

Figure 4-5: Tilt and Wannier-Stark states. Sines and cosines are also depicted to get a better sense for how the overlap integrals should behave.

where $|m, n\rangle \equiv |m\rangle_x \otimes |n\rangle_y$, $|m\rangle_x$ is the Wannier-Stark state centered at site m in the x direction [45, 40], $|n\rangle_y$ is the Wannier state centered at site n in the y direction, and J_y is the bare tunneling in the y direction just as in the Bose-Hubbard Hamiltonian. The Wannier-Stark states are shown in Fig. 4-5. From this Hamiltonian, a unitary transformation can be performed which eliminates the time-dependence in the rotating wave approximation.

The following identities are necessary to proceed and can be derived from the definition of exponentiated operators and the properties of bra and ket operators.

$$\langle m|n\rangle = \delta_{mn} \tag{4.19}$$

$$(|m\rangle\langle m|)^n = |m\rangle\langle m| \tag{4.20}$$

$$e^{-ix|m\rangle\langle m|}e^{ix|m\rangle\langle m|} = |m\rangle\langle m| \tag{4.21}$$

$$e^{-i\sum_m x|m\rangle\langle m|} = \sum_m e^{-ix|m\rangle\langle m|} = \sum_m e^{-ix}|m\rangle\langle m|. \tag{4.22}$$

Our Raman beams create a potential of the form

$$\mathcal{E}(x, y, t) = \Omega \sin(2\mathbf{q}\cdot\mathbf{r} - \omega t). \tag{4.23}$$

Recall that $2\mathbf{q} = \mathbf{k}_1 - \mathbf{k}_2$ and for the specific case under consdieration $\mathbf{k}_1 = k\hat{\mathbf{x}}$,

$\mathbf{k}_2 = k\hat{\mathbf{y}}$ and $k = 2\pi/\lambda$. The relevant matrix elements are then $\langle m,n|\sin(2\mathbf{q}\cdot\mathbf{r} - \omega t)|m+l,n+p\rangle$. With a change of variables using the symmetry of the system, we can write

$$\langle m,n|\sin(2\mathbf{q}\cdot\mathbf{r}-\omega t)|m+l,n+p\rangle = \langle 0,0|\sin(2\mathbf{q}\cdot(\mathbf{r}+\mathbf{R}_{m,n})-\omega t)|l,p\rangle, \tag{4.24}$$

where $\mathbf{R}_{m,n} = ma\hat{\mathbf{x}} + na\hat{\mathbf{y}}$. In general, we can write $2\mathbf{q}\cdot\mathbf{r} = k_x x + k_y y$. We let $\theta_{m,n} = \omega t - 2\mathbf{q}\cdot\mathbf{R}_{m,n}$ and $\phi_{m,n} = 2\mathbf{q}\cdot\mathbf{R}_{m,n}$. Then we get the matrix element in the x direction to be

$$\begin{aligned}
\langle 0,0|\sin(2\mathbf{q}\cdot(\mathbf{r}+\mathbf{R}_{m,n})-\omega t)|l,0\rangle &= \langle 0,0|\sin(k_x x + k_y y - \theta_{m,n})|l,0\rangle && (4.25)\\
&= \langle 0,0|\sin k_x x\cos k_y y\cos\theta_{m,n} && (4.26)\\
&\quad + \sin k_x x\sin k_y y\sin\theta_{m,n} && (4.27)\\
&\quad + \cos k_x x\sin k_y y\cos\theta_{m,n} && (4.28)\\
&\quad - \cos k_x x\cos k_y y\sin\theta_{m,n}|l,0\rangle && (4.29)\\
&= -\sin\theta_{m,n}\langle 0|\cos k_x x|l\rangle. && (4.30)
\end{aligned}$$

Note that we have used the approximations $\langle 0|\sin k_x x|l\rangle = \langle 0|\sin k_y y|0\rangle = 0$, due to the asymmetry in the Wannier-Stark state and $\langle 0|\cos k_y y|0\rangle = 1$. We are primarily interested in nearest neighbor tunneling, so we need only consider $l = 0,1$. Then we can approximate $\langle 0|\cos k_x x|0\rangle = 1$ and $\langle 0|\cos k_x x|1\rangle = -2J_x/\Delta$. A numerical evaluation of these integrals shown in Fig. 4-6 support these approximations.

Similar analysis shows that the matrix element in the y direction becomes

$$\langle 0,0|\sin(2\mathbf{q}\cdot(\mathbf{r}+\mathbf{R}_{m,n})-\omega t)|0,1\rangle = \cos\theta_{m,n}\langle 0|\sin k_y y|1\rangle, \tag{4.31}$$

where we used the approximations $\langle 0|\sin k_x x|0\rangle = \langle 0|\cos k_y y|1\rangle = 0$, and $\langle 0|\cos k_x x|0\rangle = 1$. Now numerically for typical experimental parameters of lattice depth $10E_{\mathrm{R}}$ and tilt per lattice site of 1 kHz, we find that $\langle 0|\sin k_y y|1\rangle \approx 0.01$. The off-diagonal term in the y direction then will have a component with strength J_y and $0.01\Omega\cos\theta_{m,n}$.

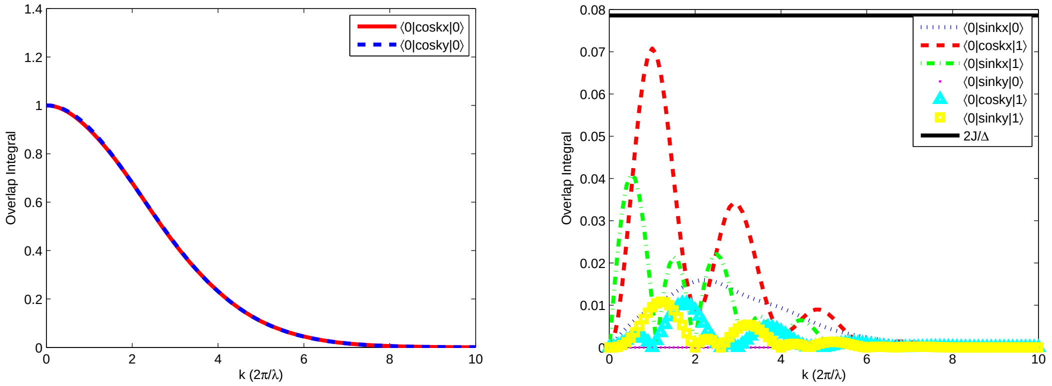

Figure 4-6: Overlap integrals to calculate Raman-assisted tunneling. The integrals involving x are done with Wannier-Stark states and the integrals involving y are done with Wannier states. The calculations were done assuming a lattice depth of $10E_{\mathrm{R}}$ in both x and y directions the linear tilt along x was assumed to be 1 kHz per lattice site.

To be able to neglect this time-dependent term, we need $J_y \gg 0.01\Omega$. For lattice depth $10E_{\mathrm{R}}$, we have $J_y = 45$ Hz and typically $\Omega \approx 1$ kHz, so we marginally have $J_y \gg 0.01\Omega$. In any case, in the perturbative regime of $\Omega/\Delta \ll 1$, this time-dependent term will be even less important.

So the relevant terms in the Hamiltonian become

$$\langle m,n|\sin(2\mathbf{q}\cdot\mathbf{r}-\omega t)|m,n\rangle = -\sin(\omega t - 2\mathbf{q}\cdot\mathbf{R}_{m,n}) \tag{4.32}$$

$$\langle m,n|\sin(2\mathbf{q}\cdot\mathbf{r}-\omega t)|m+1,n\rangle = \frac{2J_x}{\Delta}\sin(\omega t - 2\mathbf{q}\cdot\mathbf{R}_{m,n}) \tag{4.33}$$

$$\langle m,n|\sin(2\mathbf{q}\cdot\mathbf{r}-\omega t)|m,n+1\rangle = 0. \tag{4.34}$$

So our Hamiltonian becomes

$$H = \sum_{m,n}(\Delta m - \Omega\sin\theta_{m,n})|m,n\rangle\langle m,n| + \sum_{m,n}\left[\frac{2\Omega J_x}{\Delta}\sin\theta_{m,n}|m+1,n\rangle\langle m,n| + \text{h.c.}\right] - \sum_{m,n}\left[J_y|m,n+1\rangle\langle m,n| + \text{h.c.}\right]. \tag{4.35}$$

To get rid of our time-dependence, we can define a unitary transformation

$$U = \exp\left[-i\sum_{m,n}\left\{m\omega t + \frac{\Omega}{\hbar\omega}\cos\theta_{m,n}\right\}|m,n\rangle\langle m,n|\right] \tag{4.36}$$

$$= \exp\left[-i\sum_{m,n}\Lambda_{m,n}|m,n\rangle\langle m,n|\right] \tag{4.37}$$

$$= \sum_{m,n}\exp\left[-i\Lambda_{m,n}\right]|m,n\rangle\langle m,n| \tag{4.38}$$

where $\Lambda_{m,n} = m\omega t + \frac{\Omega}{\hbar\omega}\cos\theta_{m,n}$. Then in the rotating frame, the Hamiltonian transforms as

$$H' = UHU' - i\hbar U\frac{dU}{dt}. \tag{4.39}$$

The time derivative term in the transformed Hamiltonian gets rid of the time dependence in the diagonal term and replaces Δ with $\delta \sim \Delta - \omega$, which becomes zero if you drive the system on resonance, which is the situation we are considering. Since U is diagonal, it has no effect on the diagonal terms of H. So we can focus our attention on the off-diagonal terms of the transformation.

First we consider how the off-diagonal coupling in the x direction transform.

$$UH^{x}_{\mathrm{off-diag}}U' = \left\{\sum_{m',n'}\exp\left[-i\Lambda_{m',n'}\right]|m',n'\rangle\langle m',n'|\right\}\frac{2\Omega J_x}{\Delta}\sin\theta_{m,n}|m+1,n\rangle\langle m,n| \tag{4.40}$$

$$\times\left\{\sum_{m'',n''}\exp\left[i\Lambda_{m'',n''}\right]|m'',n''\rangle\langle m'',n''|\right\} \tag{4.41}$$

$$= \exp\left[-i\Lambda_{m+1,n}\right]|m+1,n\rangle\frac{2\Omega J_x}{\Delta}\sin\theta_{m,n}\exp\left[i\Lambda_{m,n}\right]\langle m,n| \tag{4.42}$$

$$= \frac{2\Omega J_x}{\Delta}\sin\theta_{m,n}e^{i(\Lambda_{m,n}-\Lambda_{m+1,n})}|m+1,n\rangle\langle m,n|. \tag{4.43}$$

Keep in mind the complex conjugate term exists but behaves almost identically. The exponential term can be simplified as

$$
\begin{aligned}
e^{i(\Lambda_{m,n}-\Lambda_{m+1,n})} &= \exp i\left[m\omega t + \frac{\Omega}{\hbar\omega}\cos\theta_{m,n} - (m+1)\omega t - \frac{\Omega}{\hbar\omega}\cos\theta_{m+1,n}\right] && (4.44)\\
&= \exp i\left[-\omega t + \frac{\Omega}{\hbar\omega}(\cos\theta_{m,n} - \cos\theta_{m+1,n})\right] && (4.45)\\
&= \exp i\left[-\omega t - 2\frac{\Omega}{\hbar\omega}\sin\left(\frac{k_x a}{2}\right)\sin\left(\theta_{m,n} - \frac{k_x a}{2}\right)\right] && (4.46)\\
&= e^{-i\omega t}e^{i\Gamma\sin(\theta_{m,n}-k_x a/2)} && (4.47)\\
&= e^{-i\omega t}\sum_p J_p(\Gamma)e^{ip(\theta_{m,n}-k_x a/2)}. && (4.48)
\end{aligned}
$$

where $\Gamma = -2\frac{\Omega}{\hbar\omega}\sin\left(\frac{k_x a}{2}\right)$ and with the relationship $e^{i\Gamma\sin\theta} = \sum_p J_p(\Gamma)e^{ip\theta}$. With this, the off-diagonal term in the x direction can be written

$$
\begin{aligned}
\frac{2\Omega J_x}{\Delta}\sin\phi_{m,n}e^{i(\Lambda_{m,n}-\Lambda_{m+1,n})} &= \frac{2\Omega J_x}{\Delta}\frac{e^{i\omega t - i\phi_{m,n}} - e^{-i\omega t + i\phi_{m,n}}}{2i} && (4.49)\\
&\quad \times e^{-i\omega t}\sum_p J_p(\Gamma)e^{ip(\omega t - \phi_{m,n} - k_x a/2)} && (4.50)\\
&= \frac{\Omega J_x}{i\Delta}\left(e^{-i\phi_{m,n}}J_0(\Gamma) - e^{-i\phi_{m,n} - ik_x a}J_2(\Gamma)\right) && (4.51)\\
&= \frac{\Omega J_x}{i\Delta}e^{-i\phi_{m,n}}\left(J_0(\Gamma) + J_2(\Gamma)\right) && (4.52)\\
&= \frac{\Omega J_x}{i\Delta}e^{-i\phi_{m,n}}\frac{2}{\Gamma}J_1(\Gamma) && (4.53)\\
&= -\frac{i\hbar\omega J_x}{\Delta}e^{-i\phi_{m,n}}J_1\left(\frac{2\Omega}{\hbar\omega}\right) && (4.54)
\end{aligned}
$$

where we used $k_x a = \pi$, the identity $J_0(x) + J_2(x) = 2/xJ_1(x)$, and $\Gamma = -2\frac{\Omega}{\hbar\omega}$ and neglected all terms which have time dependence.

Now let us consider the off-diagonal term corresponding to tunneling along the y

direction which is the direction perpendicular to the tilt.

$$UH^{y}_{\text{off}-\text{diag}}U' = -\left\{\sum_{m',n'} \exp\left[-i\Lambda_{m',n'}\right] |m',n'\rangle\langle m',n'|\right\} J_y |m,n+1\rangle\langle m,n| \tag{4.55}$$

$$\times \left\{\sum_{m'',n''} \exp\left[i\Lambda_{m'',n''}\right] |m'',n''\rangle\langle m'',n''|\right\} \tag{4.56}$$

$$= -\exp\left[-i\Lambda_{m,n+1}\right] |m,n+1\rangle J_y \exp\left[i\Lambda_{m,n}\right] \langle m,n| \tag{4.57}$$

$$= -J_y e^{i(\Lambda_{m,n}-\Lambda_{m,n+1})} |m,n+1\rangle\langle m,n|. \tag{4.58}$$

The exponential term in this case becomes

$$e^{i(\Lambda_{m,n}-\Lambda_{m,n+1})} = \exp i\left[m\omega t + \frac{\Omega}{\hbar\omega}\cos\theta_{m,n} - m\omega t - \frac{\Omega}{\hbar\omega}\cos\theta_{m,n+1}\right] \tag{4.59}$$

$$= \exp i\left[\frac{\Omega}{\hbar\omega}(\cos\theta_{m,n} - \cos\theta_{m,n+1})\right] \tag{4.60}$$

$$= \exp i\left[-2\frac{\Omega}{\hbar\omega}\sin\left(\frac{k_y a}{2}\right)\sin\left(\theta_{m,n} - \frac{k_y a}{2}\right)\right] \tag{4.61}$$

$$= e^{i\Gamma\sin(\theta_{m,n}-k_y a/2)} \tag{4.62}$$

$$= \sum_p J_p(\Gamma) e^{ip(\theta_{m,n}-k_y a/2)}. \tag{4.63}$$

where we used the relationship $e^{i\Gamma\sin\theta} = \sum_p J_p(\Gamma)e^{ip\theta}$ and $\Gamma = -2\frac{\Omega}{\hbar\omega}\sin\left(\frac{k_y a}{2}\right)$.

Then keeping only time independent terms, we have

$$-J_y e^{i(\Lambda_{m,n}-\Lambda_{m,n+1})} = -J_y \sum_p J_p(\Gamma) e^{ip(\theta_{m,n}-k_y a/2)} \tag{4.64}$$

$$= -J_y J_0(\Gamma) \tag{4.65}$$

$$= -J_y J_0\left(-2\frac{\Omega}{\hbar\omega}\sin\left(\frac{k_y a}{2}\right)\right) \tag{4.66}$$

$$= -J_y J_0\left(\frac{2\Omega}{\hbar\omega}\right), \tag{4.67}$$

where we used the fact $k_y a = \pi$ and $J_0(x) = J_0(-x)$.

In the case of resonant driving, $\hbar\omega = \Delta$ so ultimately we obtain

$$H' = \sum_{m,n} \left[-ie^{-i\phi_{m,n}} J_x J_1 \left(\frac{V_K}{\Delta} \right) |m+1, n\rangle\langle m, n| + \text{h.c.} \right] \\ - \sum_{m,n} \left[J_y J_0 \left(\frac{V_K}{\Delta} \right) |m, n+1\rangle\langle m, n| + \text{h.c.} \right]. \quad (4.68)$$

4.3.1 Perturbative and Exact Raman-Assisted Tunneling

So far we have considered two approaches to determining the laser-assisted tunneling. One was perturbative, giving rise to a Raman-assisted tunneling term which depended linearly on the Raman lattice depth, and the second involved a more explicit treatment of the time-dependent term which showed saturation in the magnitude.

Both approaches give rise to the position-dependent phase which is crucial in realizing artificial gauge fields. However, the dependence of the magnitude of Raman-assisted tunneling on the Raman lattice depth is different for the two approaches. The two expressions are

$$K_{\text{pert}} = \frac{V_K}{4} \int dx w^*(x) w(x - d_x) e^{-i\delta k_x x} \quad (4.69)$$

$$\times \int dx w^*(y) w(y) e^{-i\delta k_y y} \quad (4.70)$$

$$|K_{\text{exact}}| = J \left| J_1 \left(\frac{V_K}{\Delta} \right) \right|. \quad (4.71)$$

We can numerically check how close the two magnitudes are. This is shown in Fig. 4-7, where we had a lattice depth of $10E_{\text{R}}$ and an energy tilt between adjacent sites of 1 kHz. We see good agreement between the two results for $V_K/\Delta \lesssim 2$.

4.4 Amplitude and Phase Modulation Tunneling

It is possible to relate the mechanism of Raman-assisted tunneling to amplitude and phase modulation of the underlying lattice.

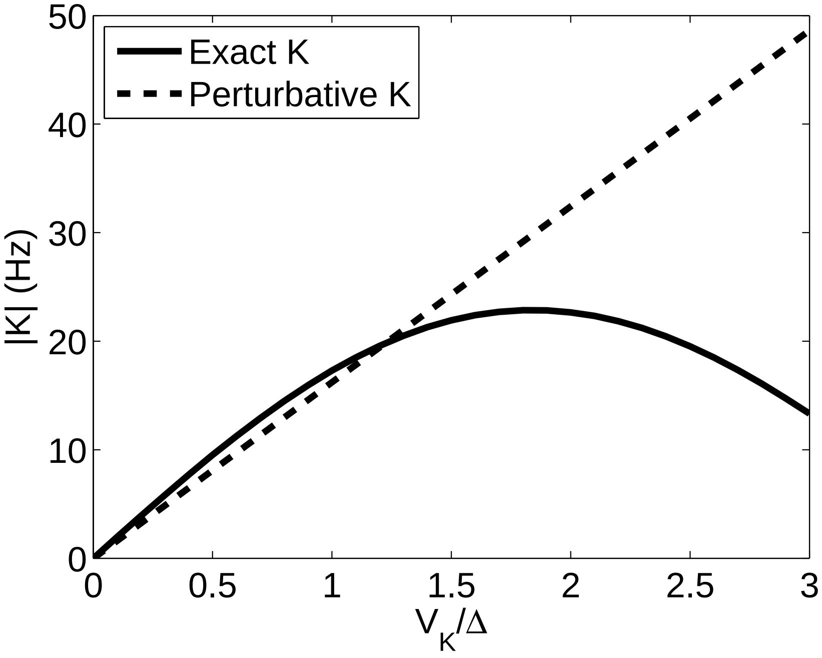

Figure 4-7: Perturbative and exact treatment of Raman-assisted tunneling. We assumed a lattice depth of $10E_\mathrm{R}$ and an energy tilt between adjacent sites of 1 kHz.

In the case of amplitude modulation, in 1D the Hamiltonian can be written [103]

$$H_{\mathrm{AM}} = \frac{p_x^2}{2m} + V_L(x)(1 + \alpha \sin \omega t) + \frac{\Delta}{a} x, \tag{4.72}$$

where α is the modulation fraction and is such that $0 \leq \alpha \leq 1$ and we write $V_L(x) = -U_0/2 \cos(2kx)$ where $k = 2\pi/a$. In second quantized form in the Wannier-Stark basis this Hamiltonian becomes

$$H_{\mathrm{AM}} = -\sum \Delta n |n\rangle\langle n| + \sum_n \left[\frac{\alpha U_0}{2} \langle n+1| \cos 2kx |n\rangle \sin \omega t |n+1\rangle\langle n| + \text{h.c.} \right]. \tag{4.73}$$

Then a unitary transformation similar to what I performed in the previous section gives, on resonance at $\hbar\omega = \Delta$,

$$H'_{\mathrm{AM}} = \sum_n \left[\frac{i\alpha U_0}{4} \langle n+1| \cos 2kx |n\rangle |n+1\rangle\langle n| + \text{h.c.} \right]. \tag{4.74}$$

Thus we see that the bare Hamiltonian in the Wannier-Stark basis has time-dependent off-diagonal terms but time-independent diagonal terms, which in the rotating wave can be written as a Hamiltonian with effective time-independent tunneling. In particular, the result permits a unlimited increase in the effective tunneling amplitude if one drives the modulation harder and harder in the frame where the lattice is stationary.

In the case of phase modulation, the lattice in the laboratory frame can be written as $V = -U_0/2 \cos[2k(x - x_0 \sin \omega t)]$ where x_0 and ω are the modulation amplitude and frequency [75]. In a frame accelerating at exactly the phase modulation, the Hamiltonian can be written [71, 92, 56, 103]

$$H_{\mathrm{PM}} = \frac{p_x^2}{2m} + V_L(x) + \beta x \sin \omega t + \frac{\Delta}{a} x, \tag{4.75}$$

where we have the atomic mass m and $\beta = m x_0 \omega^2$. With this, in the Wannier-Stark basis the Hamiltonian becomes

$$H_{\mathrm{PM}} = -\sum n(\Delta + \beta a \sin \omega t)|n\rangle\langle n| - \sum_{n} \left[\beta \langle n+1|x|n\rangle \sin \omega t |n+1\rangle\langle n| + \text{h.c.}\right]. \tag{4.76}$$

Then in the appropriate rotating frame the Hamiltonian becomes

$$H'_{\mathrm{PM}} = \sum_{n} \left[\frac{i\Delta\langle n+1|x|n\rangle}{a} J_1\left(\frac{\beta a}{\Delta}\right)|n+1\rangle\langle n| + \text{h.c.}\right]. \tag{4.77}$$

Note that in this case the effective tunneling amplitude has a maximum possible value limited by the maximum of the Bessel function as in Raman-assisted tunneling [92].

4.5 Experimental Studies of Amplitude Modulation (AM) Tunneling

Due to the fundamentally related phenomenon of ampltidue modulation (AM) tunneling and Raman-assisted tunneling, we have used amplitude modulation as a testing ground to understand under what parameter regimes we observe Raman-assisted tunneling. Experimentally, AM is much easier to implement since it can be implemented in 1D and does not require any other laser beams aside from that which is creating the lattice. AM tunneling has been experimentally explored by other groups, most notably the group of Guglielmo Tino [6, 5, 103].

4.5.1 Experimental Sequence for AM Tunneling

For our initial experiments, we have used gravity as our linear potential tilt, which should create an energy offset per lattice site with 532 nm spacing of 1137 Hz. Our experimental sequence is as follows. Using standard optical and evaporative cooling techniques [100] to achieve a Bose-Einstein condensate of a few hundred thousand atoms, we transfer the atoms which are in the $|F=1, m_F=-1\rangle$ hyperfine state into a crossed optical dipole trap with trap frequencies in the range of 30 to 160 Hz. At that point, we adiabatically ramp up a 1D optical lattice in the direction of gravity which is created by retroreflecting a single laser beam in about 200 ms. Then we extinguished our crossed dipole traps in 200 ms (we also attempted to extinguish even faster, but aside from center-of-mass motion perpendicular to the lattice, this had no discernable effect on the results presented here). At this point, the atoms are held only by an optical lattice pointing in the vertical direction. Confinement in the vertical direction is provided by the optical lattice, and confinement in the perpendicular direction is provided by the gaussian envelope of the lattice beam. Furthermore, by extinguishing the crossed optical dipole traps, that automatically creates a linear gradient with exactly the strength of gravity. The lowering of the confinement in the perpendicular direction appears to help to reduce density and inhomogeneous tilts due to curvature. At this point, we begin to modulate the lattice depth and perform measurements.

4.5.2 *In Situ* Measurements of AM Tunneling

Our initial measurements were performed *in situ*, by taking absorption images of the atoms in the optical lattice. When the potential gradient is present, the atoms are unable to tunnel because they are off-resonant. Modulation of the lattice amplitude reestablishes tunneling as described in a previous section. This AM tunneling then allows the atom cloud to expand symmetrically in the vertical direction due to the lack of confinement in addition to the lattice. Thus measuring the spatial width of the atomic cloud after modulation gives an indication of the strength of tunneling.

The way we determined the resonance frequency of AM tunneling was to modulate an originally static lattice with a depth of $10E_{\mathrm{R}}$ for 501 cycles of modulation with an amplitude of $2E_{\mathrm{R}}$ and repeat the experiment for various modulation frequencies. This result is shown in the top left of Fig. 4-8. Fitting the data to a lorentzian, we determine the resonance to be at 1133.5 ± 0.5 Hz and the width to be 2.2 ± 0.2 where the uncertainties indicate 95% confidence intervals (note this is equivalent to two standard deviations). From the fact that $g = 9.81$ m/s^2, we expect the resonance at 1137 Hz. The discrepancy is primarily expected to be due to slight misalignment

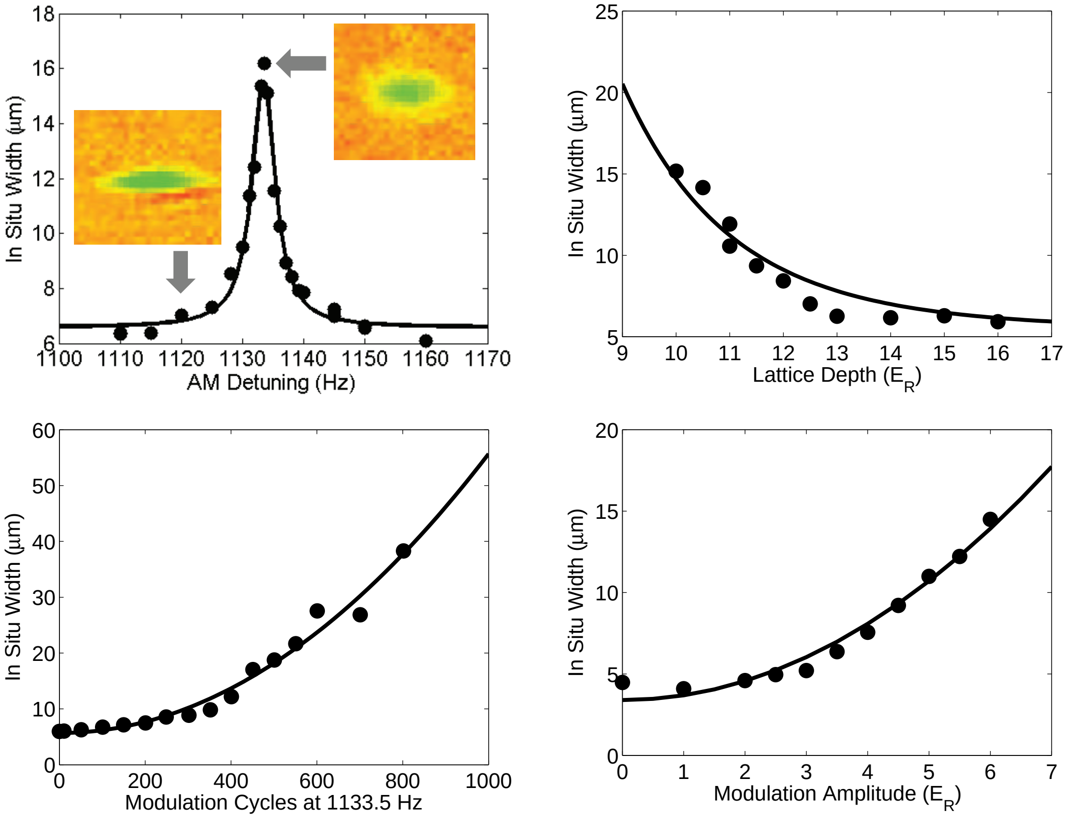

Figure 4-8: *In situ* amplitude modulation tunneling measurements. Top left: *In situ* width of the atomic cloud as a function of AM frequency. Inset is a representative atom distribution on and off resonance observed by absorption imaging. Top right: Atom width as a function of lattice depth for modulation on resonance at 1133.5 Hz. Curve is a plot of the square of the analytical expression for the tunneling matrix element, whose close agreement with data suggests that the width increases as the square of the tunneling matrix element. Bottom left: Atom width as a function of the number of modulation cycles. The curve is a fit of the data to a parabola. Bottom right: Atom width as a function of modulation amplitude. The curve is a fit of the data to a parabola. Both bottom curves suggest the width increases as the square of the tunneling matrix element, $(aJt)^2$.

of the laser beams.

We also studied the dependence of the *in situ* width on the lattice depth. Our static lattice was at a depth of $10E_{\mathrm{R}}$, on resonance at 1133.5 Hz and modulated for 501 cycles at an amplitude of $2E_{\mathrm{R}}$. This is shown in the top right of Fig. 4-8. I also plot the analytic expression for the square of resonant tunneling with only one fitting parameter which determines the overall proportionality factor. The analytic expression for resonant tunneling in a flat lattice with lattice depth V_L is given as [29]

$$J = \frac{4}{\sqrt{\pi}} E_{\mathrm{R}}^{1/4} V_L^{3/4} e^{-2\sqrt{\frac{V_L}{E_{\mathrm{R}}}}}. \tag{4.78}$$

We can write $V_L = N_L E_{\mathrm{R}}$, so in the figure I plot the square of this up to some proportionality factor C, as

$$\sigma(V_L) = C V_L^{3/2} e^{-4\sqrt{N_L}}. \tag{4.79}$$

It is reasonable to expect the width to increase as a function of the value aJt where t is the modulation time and a is the lattice spacing. The close agreement between data and the analytic expression suggests that the width increases as the square of the tunneling, $\sigma \propto (aJt)^2$. The following two data sets are consistent with tunneling increasing the size as $(aJt)^2$.

We further studied the *in situ* width as a function of the number of modulation cycles and modulation amplitude. These are plotted in the left bottom and right bottom of Fig. 4-8, respectively. The data are well-fitted by parabolic curves, again indicating that the width increases as the square of tunneling, or $(aJt)^2$.

Note that in general, ballistic expansion goes linearly in time, and diffusive expansion goes as the square root of time. Thus the expansion behavior observed in our measurements is not compatible with either, and could be due to heating effects. Further study is needed to fully understand the expansion behavior of the atomic cloud.

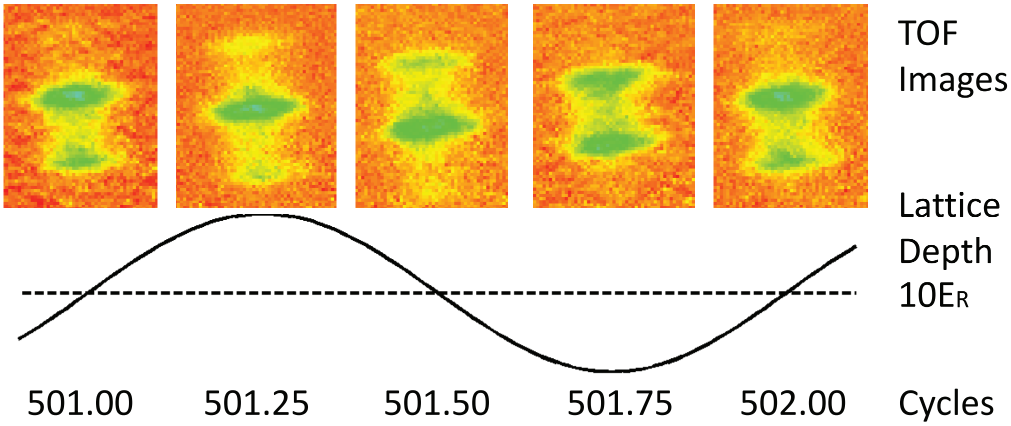

Figure 4-9: Evolution of superfluid peaks under lattice amplitude modulation. These data were taken at a lattice depth of $10E_{\mathrm{R}}$ and modulation amplitude of $2E_{\mathrm{R}}$. Note that the particular interference pattern depends on the particular phase of the modulation when the atoms are released from the lattice.

4.5.3 Time-of-Flight Measurements of AM Tunneling

We have further studied the effects of AM tunneling on the coherence properties of the atomic cloud by the method of time-of-flight absorption imaging. In particular, initially after the tilt is turned on, the atomic cloud does not exhibit sharp interference peaks, but after typically about 100 ms of amplitude modulation on resonance, we are able to restore superfluid peaks. The speed of restoring superfluid peaks depend on the AM strength as well as the initial lattice depth. One particular sequence of pictures is shown in Fig. 4-9. These data were taken at a lattice depth of $10E_{\mathrm{R}}$ and modulation amplitude of $2E_{\mathrm{R}}$. Note that the particular interference pattern depends on the particular phase of the modulation when the atoms are released from the lattice, in agreement with the qualitative behavior seen by the Sengstock group in their phase modulated phase imprinting scheme [101]. This indicates that when we are able to establish superfluid coherence with Raman beams, the particular time-of-flight interference pattern will depend on the exact phase relationship between the two Raman beams, which could change from shot-to-shot.

4.6 Experimental Observation of Raman-Assisted Tunneling

After having determined the experimental parameter space where we can observe amplitude modulation tunneling, we implemented the Raman-assisted tunneling scheme to create position-dependent phases. We analyzed *in situ* atomic dynamics, whose expansion we found to become saturated and subsequently decreased in the tunneling amplitude upon increasing our Raman laser intensities, just as predicted from our theory of Raman-assisted tunneling. Although this gives an indication that we have successfully created the Harper Hamiltonian, we have been unable to observe the signature of the ground state of this Hamiltonian which should manifest itself in a time-of-flight picture.

4.6.1 Experimental Sequence for Raman-Assisted Tunneling

Our experimental sequence is identical to the case of AM tunneling described in subsection 4.5.1 up until we create the linear potential tilt by extinguishing the crossed optical dipole trap, except for the fact that instead of a 1D lattice, now a 2D lattice is adiabatically ramped up in the same amount of time to $10E_{\mathrm{R}}$ in both directions (unless otherwise noted). Then the two Raman beams are turned on to a value when combined yield an effective travelling Raman lattice depth of V_K. The experimental schematic is shown on the left of Fig. 4-10.

The Raman lattice strengths were calibrated by performing two-photon Rabi oscillations between momentum states of $\mathbf{k} = \mathbf{0}$ and $\mathbf{k} = \mathbf{k}_1 - \mathbf{k}_2$, where $\mathbf{k}_1 = 2\pi/\lambda\hat{\mathbf{x}}$ $\mathbf{k}_2 = 2\pi/\lambda\hat{\mathbf{y}}$ are the wavevectors of the two Raman beams. This oscillation can be induced by detuning the two Raman beams by $2E_{\mathrm{R}}/h = 4056$ Hz. This can be understood from the fact that Raman beams impart a momentum on the atoms of magnitude $|\mathbf{k}| = \sqrt{2}2\pi/\lambda$. The corresponding kinetic energy of the recoiling atom is given by $\hbar^2\mathbf{k}^2/(2m) = 2E_{\mathrm{R}}$. The oscillation frequency Ω can be related to the Raman lattice depth as $V_K = 2\Omega$.

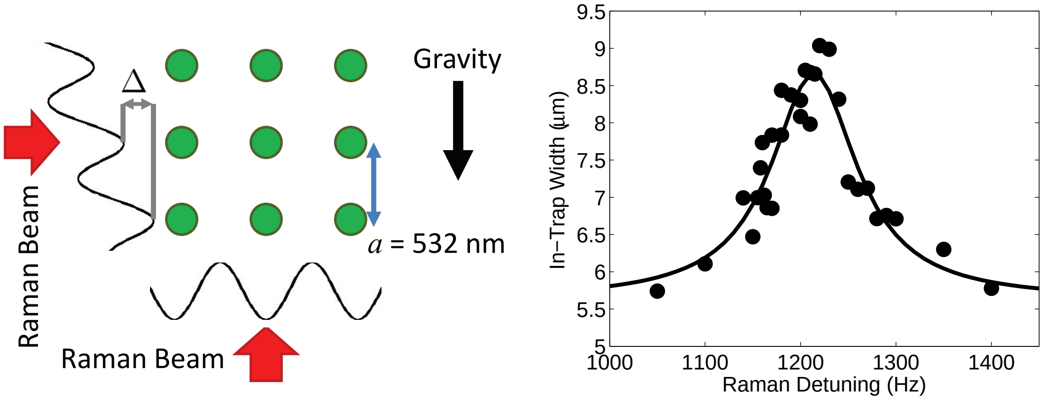

Figure 4-10: Raman-assisted tunneling setup and spectrum. Left: Schematic of our experimental setup. The energy offset per lattice site Δ from gravity is 1137 Hz. The lattice and Raman beams are all derived from a 1064 nm laser. Right: *In situ* atomic cloud width as a function of detuning of the two Raman beams. The 2D lattices were set at $10E_\mathrm{R} = 20.3$ kHz and $V_K = 2.3$ kHz. The solid line is a fit to a lorentzian curve.

4.6.2 *In Situ* Measurements of Raman-Assisted Tunneling

We performed *in situ* measurements just as in the amplitude modulation tunneling experiment, but now with Raman beams to induce Raman-assisted tunneling. We acquired data by taking absorption images along the direction perpendiclar to the 2D lattice. First we scanned the detuning between the two Raman beams and looked for expansion of the atom cloud. The two-dimensional lattices were both $10E_\mathrm{R} = 20.3$ kHz with intensities in the Raman beams corresponding to $V_K = 2.3$ kHz and held for 400 ms. This is shown in the right of Fig. 4-10. A lorentzian fit gives the resonance to be at 1214 ± 6 Hz and the width to be 54.6 ± 15.9 Hz where the uncertainties are again 95% confidence levels, equivalent to two standard deviations. Recall gravity should give a resonance at 1137 Hz. The discrepancy can be attributed to slight misalignment of the laser beams and could be larger than in the amplitude modulation case because we have one additional lattice beam, as well as two Raman beams.

Once the resonance was found, we fixed the detuning of the Raman beams at 1214 Hz and looked at the atomic cloud width for different modulation times at

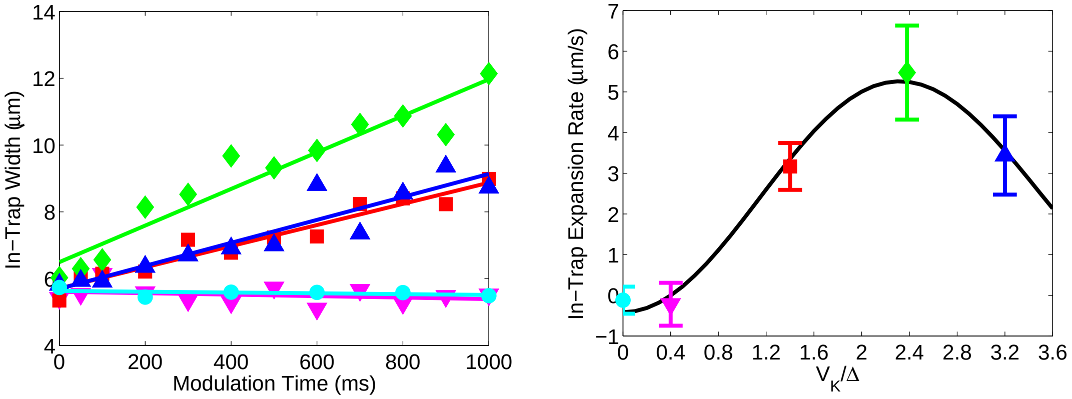

Figure 4-11: Raman-assisted tunneling leads to linear expansion in time. The atomic cloud expansion as a function of time is plotted on the left for different Raman intensities. On the right, the slope of the lines on the left plot are shown as a function of Raman strength, and is fit to the square of $J_1(V_K/\Delta)$. The Raman detuning was fixed to the resonance value of 1214 Hz.

different Raman intensities. From our theoretical discussions, we should expect to see a saturation in the tunneling as the Raman depth increases and even turn over so that beyond a certain point, stronger drives lead to less tunneling per time. The data are plotted in Fig. 4-11. We see a linear expansion in the width as a function of time for all Raman intensities. We would expect the slope of this expansion to be proportional to the tunneling amplitude. On the right of the figure I plot the slopes as a function of Raman lattice strength. The line is a fit to the square of the Bessel function, $J_1(V_K/\Delta)$. Recall that for amplitude modulation, we saw an expansion of the atomic cloud going as the square of time, whereas now the expansion goes linearly with time.

We further explored this Bessel function behavior by looking at the atomic cloud width as a function of Raman strength for fixed modulation time to observe the high Raman beam intensity regime. This is shown in Fig. 4-12, where we plot the obtained data, along with a fit to the square of $J_1(V_K/\Delta)$ for data up to $V_K/\Delta = 3.2$ which is the value we had in Fig. 4-11. The fit agrees well with data up to the value $V_K/\Delta = 3.2$, but does not fit the data well for higher Raman strengths. This could be due to inhomogeneities in the tilt Δ which gives rise to different resonance conditions

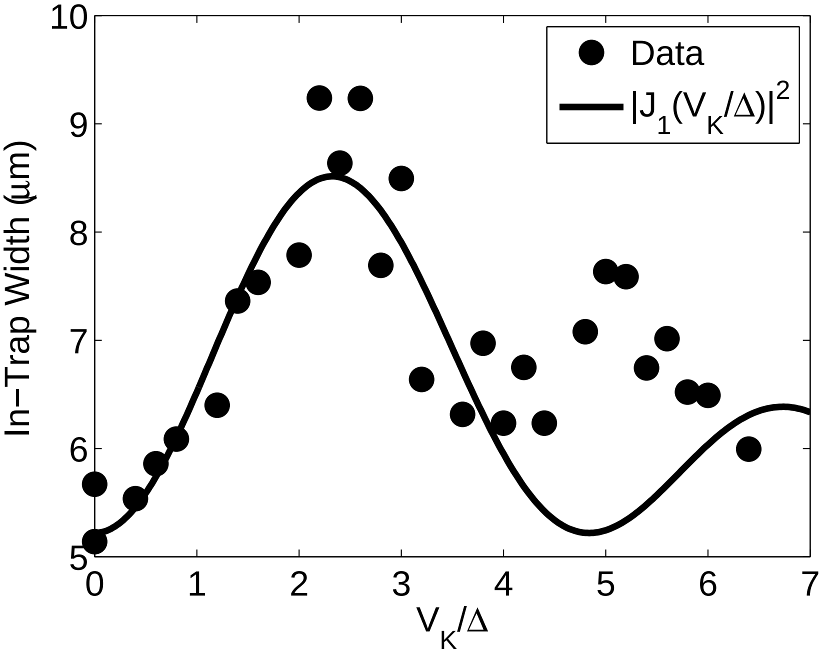

Figure 4-12: Raman-assisted tunneling for high Raman beam intensities. The Raman detuning was fixed to the resonance value of 1214 Hz, and the Raman laser strength was varied. The tunneling restored by the running wave Raman beams qualitatively behaves as a Bessel function as a function of the Raman strength. The line is a fit to the square of $J_1(V_K/\Delta)$ up to $V_K/\Delta = 3.2$ where the data in Fig. 4-11.

at different parts of the atom cloud or high intensity effects not captured in our model. Further studies are needed to understand the discrepancy at high Raman intensities.

Also, the expansion behavior as the square of the Bessel function is not quite well understood, although similar behavior has been observed by the Arimondo group using phase modulation [92]. They attribute this behavior partly to interaction effects, where by varying the atom number they can change the expansion behavior. Although we also varied our atom number by more than a factor of 5, we were unable to observe any difference in the expansion dynamics.

We also examined the cloud width for a given Raman strength and duration as a function of lattice depth in the direction of the tilt. This is shown in Fig. 4-13. The Raman detuning was fixed on resonance at 1214 Hz, the Raman strengths were such that $V_K = 2.6$ kHz and modulated for 400 ms. The curve is a fit of the analytic

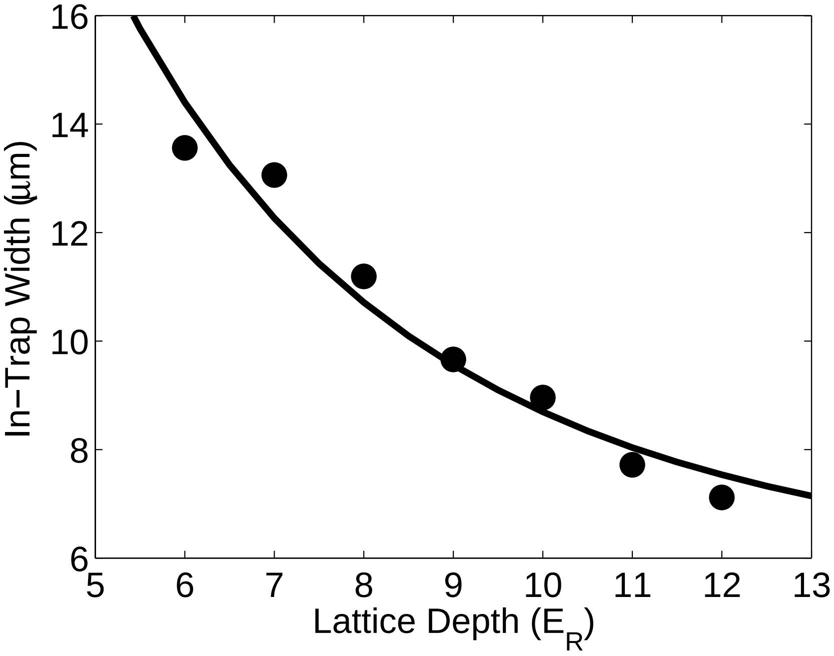

Figure 4-13: Raman-assisted tunneling as a function of the lattice depth. The curve is proportional to the analytic expression for the bare tunneling [29]. Contrast this with what we saw in the top right of Fig.4-8, where the width was proportional to the square of the tunneling.

expression for tunneling up to a proportionality constant, and is of the form [29]

$$\sigma(V_L) = CV_L^{3/4}e^{-2\sqrt{N_L}}. \tag{4.80}$$

This curve agrees well with the data. Compare this with the situation we saw with amplitude modulation, where the width was increasing as the square of the bare tunneling. Further studies will be needed to understand the cause of these different expansion behaviors.

By scanning the detuning even further from the resonance at Δ, we have been able to observe higher order tunneling processes. In particular we observed tunneling at $\Delta/2$ and possibly even lower fractions of Δ in the left of Fig. 4-14. This data was taken with the lattice in the tilt direction at $7E_{\mathrm{R}}$, the perpendicular lattice at $10E_{\mathrm{R}}$, and the Raman intensity at 1.1 kHz for 400 ms. The $\Delta/2$ resonance is clearly visible, but the lower frequency resonances are not as sharp, possibly due to the fact that the resonances are overlapping each other. A fit to three gaussians tells us that the left most peak is centered at 348 ± 37 Hz with a width of 62 ± 41 Hz, the $\Delta/2$ resonance is centered at 560 ± 5 Hz with a width of 29 ± 5 Hz, and the Δ resonance is centered at 1122 ± 18 Hz with a width of 91 ± 24 Hz. The uncertainties are 95% confidence levels, equivalent to two standard deviations.

We also observed tunneling at a Raman detuning of 2Δ, which corresponds to a two-photon Raman-assisted tunneling to next-nearest-neighbors. This is shown in the right of Fig. 4-14, where the Raman beams were applied for 2 s but otherwise the same experimental parameters as above. A fit to two gaussians tells us that the Δ resonance is centered at 1137 ± 31 Hz with a width of 107 ± 31 Hz and the 2Δ resonance is centered at 2262 ± 46 Hz with a width of 171 ± 87 Hz. Such higher order tunneling processes, especially the ability to engineer a system where the next-nearest-neighbor tunneing dominates the nearest-neighbor tunneling may be particularly attractive to study systems with long range interactions.

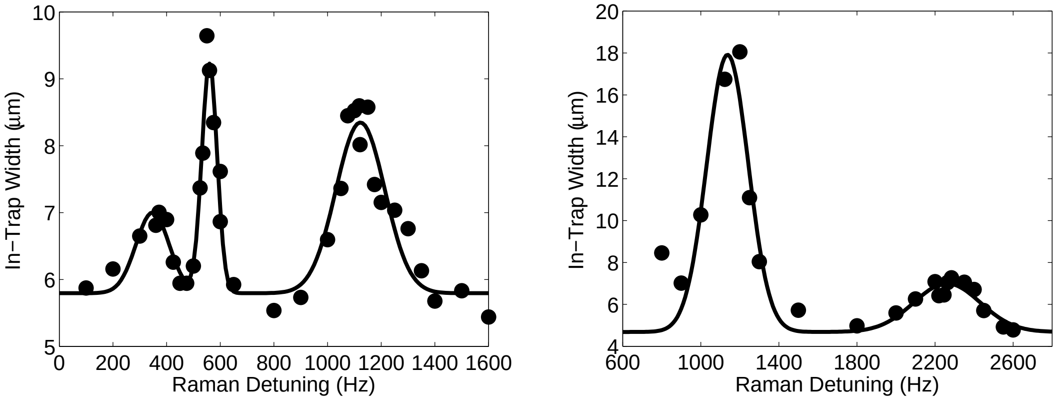

Figure 4-14: Higher-order and Next-nearest-neighbor tunneling with Raman beams. The left figure shows resonances at Raman detunings corresponding to $\Delta/2$, which are 4-photon processes to nearest neighbor sites, and even lower detunings. The right figure shows a resonance at 2Δ which corresponds to 2-photon tunneling to next-nearest-neighbor sites.

4.6.3 Time-of-Flight Measurements of Raman-Assisted Tunneling

Our successful observation of *in situ* Raman-assisted tunneling and the confirmation of its Bessel function-like properties gives a strong indication that we have been able to realize the Harper Hamiltonian. However, in order to confirm the creation of the ground state of the Harper Hamiltonian, we need to be able to observe the restored superfluid peaks whose spatial pattern should give an indication of the underlying band structure which have been modified from the simple square lattice by the position-dependent phase imprinted on the ground state wavefunction [82].

Unfortunately, we have so far been unable to observe the restoration of superfluid peaks and the consequent novel band structure. Empirically, it appears that the curvature of our laser beams may be preventing us from making the crucial observation. Immediate future efforts will focus on understanding how we can establish superfluid peaks in time-of-flight imaging. This should give the smoking-gun signature of the ground state of the Harper Hamiltonian.

4.7 Conclusions

The technique of Raman-assisted tunneling allows one to study the Harper Hamiltonian with arbitrary flux. In addition, by including a third optical lattice, we can significantly increase the interaction energy between the atoms such that we are in the highly non-trivial regime of strongly correlated matter with artificial magnetic fields, which can give rise to the celebrated Laughlin states of fractional quantum Hall state fame [68]. Another direction is to add more spin states so that one can study spin Hall effects which is a part of the burgeoning field of spintronics. Thus there is significant promise in terms of the types of physics one can explore if one is able to successfully create the Harper Hamiltonian and its ground state.

We have strong indications that the Harper Hamiltonian has been created with Raman-assisted tunneling, as indicated by our *in situ* data which shows that our tunneling behaves as a Bessel function. Thus we can say that we have confirmed the absolute value of the Raman-assisted tunneling in the Harper Hamiltonian. However, so far we have been unable to prove that we have created the ground state of this Hamiltonian in time-of-flight images. There are indications that curvature of our laser beams prevents us from achieving the ground state. We are able to restore coherence in amplitude modulation, and the *in situ* dynamics of the atomic cloud is different from that with Raman-assisted tunneling. Thus understanding the *in situ* dynamics in further detail may give us a better understanding of the requirements to obtain the ground state of the Harper Hamiltonian. Once this hurdle is over come and we are able to observe the ground state of the Harper Hamiltonian, a whole new field of exploring topological phases of matter with ultracold atoms in optical lattices will be realized.

Chapter 5

Future Prospects

I have described in this thesis two different types of work. The Bragg scattering work was geared toward the development of new measurement techniques to probe new states of matter. On the other hand, the work on realizing the Harper Hamiltonian by employing Raman-assisted tunneling was geared toward directly creating a new state of matter. Progress in the field of ultracold atoms will require both development of probing techniques and creation of new matter, with both providing inspiration to the other.

5.1 Prospects for Spin Hamiltonians

The Bragg scattering work was particularly geared towards its eventual use as a probe of spin ordering, such as the antiferromagnetic state. The Heisenberg Hamiltonian which gives rise to magnetic states have an energy scale of J^2/U, which is on the order of 100 pK [15]. This is a very low energy scale, which at present only adiabatic cooling techniques have any hope of directly reaching such low entropy states [116, 76].

Spin gradient demagnetization cooling in its original form may very well take the field down to the superexchange energy scale to realize spin Hamiltonians, but people, including our group, have been thinking of other ways to access spin physics. One notable success achieved by the group of Markus Greiner has been to use occupation number of atoms on lattice sites as pseudo-spins to realize antiferromagnetic ordering [93]. Another approach, developed by our group, has been to use spin-dependent lattices. In particular, one can create a low entropy effectively single component Mott insulator where the spin-dependent lattice creates a 3D lattice for two spin species interweaved between each other, and then adiabatically merge the two lattices. Because the initial 'dual Mott' system can have very low entropy, as long as the merging is adiabatic, one should be able to achieve very low entropy spin-mixed states in a 3D lattice, which should be able to exhibit magnetic phases of matter as dictated by the Heisenberg Hamiltonian.

Thus the future of spin Hamiltonians in ultracold atomic systems will most likely involve some combination of brute force cooling techniques to reach picoKelvin temperatures and ingeneous schemes which allow the manifestation of spin physics at higher energy scales.

5.2 Prospects for Topological Phases of Matter

Topological phases of matter are usually related to magnetic fields. In neutral cold atom systems, various techniques have already allowed the creation of effective magnetic fields. These include mechanical rotation of bulk quantum degenerate gases [74, 1] and Raman processes in bulk quantum degenerate gases [72, 110, 17]. These techniques have the limitation that high effective magnetic fields, or more specifically high effective magnetic flux per relevant spatial scale, are not easily realizable. Lattice systems offer a promising route to realizing such effectively high fluxes.

In the last few years, the group of Klaus Sengstock has realized the creation and control of artificial gauge fields in a lattice by lattice modulation [101], the group of Ian Spielman has achieved similar results by using Raman transitions and radiofrequency magnetic fields [60], and the group of Immanuel Bloch has realized staggered fluxes by using a superlattice and Raman-assisted tunneling. The first two techniques are only able to create position-independent phases, and the last is only able to create staggered fluxes. It seems possible to extend all of these techniques to achieve position-dependent, homogeneous fluxes, but the schemes are somewhat involved, requiring more laser beams to address more transitions. If we are able to prove experimentally that we can create the ground state of the Harper Hamiltonian which has non-trivial topological properties, it will be a much simpler way to realize the same physics that the other groups are aiming for with a more complicated setup.

Once the Harper Hailtonian is realized, one can add interactions to the system by using, for example, a third optical lattice, which should allow the study of fractional quantum Hall states [94, 48] which manifest interesting topological properties of matter.

Thus the general trend in the quest to realize artificial gauge fields and topological phases of matter has been to add more and more laser beams, but a technique such as ours which requires a relatively simple set up could hold the key to major progress in the field.

5.3 Prospects for Quantum Simulation

The prospects for the program of quantum simulation seem bright [18]. It seems that every few months a new type of system is realized in the laboratory, ranging from graphene-like honeycomb lattice structures exhibiting Dirac points [104], analogues of superconducting weak links with Bose-Einstein condensates in novel trap geometries [117], and 'Higgs' type excitations in the superfluid to Mott insulator transition [31]. As can be seen in these examples, results from the field of ultracold atoms is becoming strongly connected to concepts and ideas from condensed matter physics, and even high energy physics.

Furthermore, different groups are also pushing the boundaries of 'traditional' ultracold atoms. By traditional, I mean alkali-metal atoms which have one valence electron. Various groups have successfully created quantum degenerate gases of two-valence-electron atoms such as calcium [66] strontium [98, 25], and ytterbium [102]. Even more exotic atoms have been cooled to quantum degeneracy, such as chromium [43], erbium [4] and dysprosium [73], which all have large magnetic dipole moments and therefore can give rise to anisotropic dipolar interactions. All these different atomic systems will be able to explore a parameter space that alkali-metal atoms have not yet been able to access thus far.

Numerous developments on all fronts of quantum simulation will certainly lead to many new insights and discoveries of nature, most likely with implications beyond the field of ultracold atomic physics and further enriching and illuminating our understanding of condensed matter systems and beyond.

Appendix A

Optical Lattice Calibration Using Kapitza-Dirac Scattering

In this appendix, I describe the method we use to calibrate our optical lattice, namely Kapitza-Dirac scattering [46].

The basic procedure is to pulse the optical lattice beams on for a very short time. The short pulse then transfers momentum to the atoms, and then in a time-of-flight absorption picture observe the spatial distribution of atoms. In particular the atoms are scattered into discrete momentum states with probability given by how intense the pulse was. Therefore by knowing how much optical power was in the pulses, and measuring the population distribution of atoms in the different momentum states, one can determine the resulting lattice depth created by the pulse.

The electric field **E** produced by two counter-propagating plane waves is given by

$$\mathbf{E}(z,t) = E_0 f(t)\sin(kz-\omega t)\hat{e} + E_0 f(t)\sin(kz+\omega t)\hat{e} \tag{A.1}$$

$$= 2E_0 f(t)\sin(kz)\cos(\omega t)\hat{e}, \tag{A.2}$$

where E_0 is the electric field amplitude, k is the wavevector, ω is the angular frequency, $\hat{e}$ is the polarization vector, and $f(t)$ is the temporal envelope function.

Such a field will produce an AC Stark shift, leading to a standing wave potential

$U(z,t)$ given by

$$U(z,t) = \frac{\hbar\omega_{\mathrm{R}}^2}{\delta} f^2(t)\sin^2(kz), \tag{A.3}$$

where ω_{R} is the single-photon Rabi frequency, given by $\omega_{\mathrm{R}} = \mu E_0/\hbar$, where $\mu = \langle e|e\mathbf{r}|g\rangle \cdot \hat{e}$ is the electric dipole matrix element connecting the ground ($|g\rangle$) and excited ($|e\rangle$) states of the atom, and δ is the detuning. We may write

$$U_0 \equiv \frac{\hbar\omega_{\mathrm{R}}^2}{\delta}. \tag{A.4}$$

If the optical lattice is turned on for a very short time (i.e. $\tau \ll 1/\omega_{\mathrm{r}}$, where ω_{r} is the recoil energy), the initial atomic wavefunction $|\Psi_0\rangle$ will evolve in a way given by

$$|\Psi\rangle = \exp\left\{-\frac{i}{\hbar}\int dt' U(z,t')\right\}|\Psi_0\rangle \tag{A.5}$$

$$= e^{-\frac{i}{2\delta}\omega_{\mathrm{R}}^2\tau} e^{\frac{i}{2\delta}\omega_{\mathrm{R}}^2\tau\cos(2kz)}|\Psi_0\rangle, \tag{A.6}$$

where $\tau = \int dt' f^2(t')$ and the integral is over the interaction duration. This short time condition is called the Raman-Nath regime. For KD, our pulse is a constant square pulse, so we let $f(t') = 1$. We then make use of a Bessel function identity

$$e^{i\alpha\cos\beta} = \sum_{n=-\infty}^{\infty} i^n J_n(\alpha) e^{in\beta} \tag{A.7}$$

to get

$$|\Psi\rangle = e^{-\frac{i}{2\delta}\omega_{\mathrm{R}}^2\tau} \sum_{n=-\infty}^{\infty} i^n J_n\left(\frac{\omega_{\mathrm{R}}^2\tau}{2\delta}\right) e^{i2nkz}|\Psi_0\rangle. \tag{A.8}$$

We may let $|\Psi_0\rangle = |g\rangle|0\rangle$, where the first state represents the internal state of the atoms and the second state represents the external state of the atoms. Note that we can write

$$e^{i2nkz} = \sum_{p'} |p' + 2n\hbar k\rangle\langle p'|, \tag{A.9}$$

which can be used to get

$$\sum_{n=-\infty}^{\infty} e^{i2nkz}|0\rangle = \sum_{n=-\infty}^{\infty} |2n\hbar k\rangle. \tag{A.10}$$

This can be inserted into Eq. A.8 to get

$$|\Psi\rangle = e^{-\frac{i}{2\delta}\omega_{\mathrm{R}}^2\tau} \sum_{n=-\infty}^{\infty} i^n J_n\left(\frac{\omega_{\mathrm{R}}^2\tau}{2\delta}\right)|g\rangle|2n\hbar k\rangle. \tag{A.11}$$

It is now easy to see that the probability that a state with momentum $2N\hbar k$ will be populated is given by

$$P_N = J_N^2(\theta)\ ,\ N = 0, \pm 1, \pm 2, ...,\ \text{where} \tag{A.12}$$

$$\theta = \frac{\omega_{\mathrm{R}}^2\tau}{2\delta}. \tag{A.13}$$

Our KD fit program takes as input the intensity of the KD peaks, which is proportional to the probability P_N of atoms being in a particular momentum state, and the photodiode voltage V which is monitoring the power given to a particular lattice beam. Thus we may rewrite Eq. A.12 as

$$P_N = J_N^2(\alpha V), \tag{A.14}$$

where $\theta = \alpha V$. The KD program determines the proportionality constant α, where $[\alpha]$ =rad/V. Then we can write

$$\alpha V = \frac{\tau}{2} \times \frac{\omega_{\mathrm{R}}^2}{\delta}. \tag{A.15}$$

If we assume $f(t) = 1$ over the pulse duration (i.e. a square pulse), τ simply becomes the pulse duration and is typically 12.5 μs with a rise and decay time of 5 ns.

Now, note that we can rewrite Eq. A.4 to get

$$\frac{\omega_{\mathrm{R}}^2}{\delta} = \frac{U_0}{\hbar}. \tag{A.16}$$

From atomic physics we know that

$$U_0 \propto \omega_{\mathrm{R}}^2 \propto I \propto P \propto V, \tag{A.17}$$

where I is the intensity of the laser beam, P is the power incident on the photodiode, and V is the voltage induced in the photodiode. From this we can write

$$U_0 = \gamma V, \tag{A.18}$$

where $[\gamma]$ =J/V and is a proportionality constant. We can insert this into Eq. A.16 to get

$$\frac{\omega_{\mathrm{R}}^2}{\delta} = \frac{\gamma V}{\hbar}. \tag{A.19}$$

Now we can insert this into Eq. A.15 to get

$$\alpha V = \frac{\tau}{2} \times \frac{\gamma V}{\hbar} \Rightarrow \gamma = \frac{2\hbar\alpha}{\tau}. \tag{A.20}$$

Now, we want recoil/V, which we call β, for calibration purposes. We have $[E_{\mathrm{r}}]$ = J/recoil, where $E_{\mathrm{r}} = \hbar\omega_{\mathrm{r}}$, so

$$\beta = \frac{2\hbar\alpha}{\tau} \times \frac{1}{E_{\mathrm{r}}} = \frac{2\hbar\alpha}{\tau} \times \frac{1}{\hbar\omega_{\mathrm{r}}} = \frac{2\alpha}{\tau\omega_{\mathrm{r}}}. \tag{A.21}$$

We can write ω_{r} in terms of the wavelength λ of the lattice beam to make it easier for plug and chug. Recall $\hbar\omega_{\mathrm{r}} = \hbar^2 k^2/2m$ and $k = 2\pi/\lambda$ where m is the mass of the atom, so $\omega_{\mathrm{r}} = \hbar(2\pi/\lambda)^2/2m$. We can rewrite Eq. A.21 as

$$\beta = \frac{4\alpha m}{\hbar\tau} \times \left(\frac{\lambda}{2\pi}\right)^2. \tag{A.22}$$

Appendix B

Code to Construct Wannier Functions

This appendix provides a copy of a MATLAB® code to construct maximally localized Wannier functions for any lattice spacing and lattice depth that the user can specify. In the process the band structure can also be extracted. A sample output of this code for lattice spaing 532 nm and lattice depth $3E_{\mathrm{R}}$ is provided in Fig. B-1.

```
% Determine the Wannier function
% Written by Hirokazu Miyake
% Date: 4/21/2013
%
% lambda = lattice laser wavelength
% l = number of Fourier components to take
% Er = recoil energy
% V = V0/Er lattice depth in units of recoil energy
% q = q/k = q*a/pi where a = lattice spacing

clear;
lambda = 1064E-9;           %lattice laser wavelength
dxn = 0.01;
x = lambda/2*(-10:dxn:10); %real space coordinates
dx = dxn*lambda/2;          %discretization of space
x1 = 0;                     %center position of Wannier function
V = 3;                      %lattice depth in units of the recoil energy
l = 5;

wavevec = 2*pi/lambda;      %wavevector
```

```
dn = 500;
qend = 1;
dq = 2*qend/dn;

H = zeros(2*l+1);
q = -qend:dq:qend;
nq = length(q);
Eeig = zeros(1,dn+1);
%Veig is c_j's vs q
Veig = zeros(2*l+1,dn+1);

%construct the Hamiltonian and find eigenvalues and eigenvectors
%s is a sum over q
for s = 1:dn;
    for n = 1:(2*l + 1)
        for m = 1:(2*l + 1)
            if n == m
                H(n,m) = (2*(-l-1+n) + q(s)).^2 + V/2;
            elseif abs(n - m) == 1
                H(n,m) = -V/4;
            else
                H(n,m) = 0;
            end
        end
    end
    [W,D] = eig(H);
    Eeig(s) = D(1,1);
    for t = 1:(2*l+1)
       Veig(t,s) = W(t,1);
    end
end

nx = length(x);
wan1 = zeros(1,nx); %initialize wannier function
u=zeros(nq,nx);     %u is q vs x
phi=zeros(nq,nx);

%create u_q(x)
% loop over q
for qi = 1:(nq-1)
    for xi = 1:nx
        %sum over j's from -L to L
        for k = 1:(2*l + 1)
            u(qi,xi) = Veig(k,qi)*exp(1i*2*wavevec*x(xi)*(-l-1+k))...
                + u(qi,xi);
```

```
        end
        phi(qi,xi) = exp(1i*q(qi)*wavevec*x(xi)).*u(qi,xi);
    end
end

%create phi_q(x)
%note that the phase has to be this specific one to create
%the maximally localized Wannier function
for qi = 1:(nq-1)
    phi(qi,:) = exp(-1i*angle(phi(qi,x==0)))*phi(qi,:);
end

%create Wannier function w(x-x0)
%loop over x
for xi = 1:nx
    %sum over q
    for qi = 1:(nq-1)
        wan1(xi) = phi(qi,xi)*exp(-1i*q(qi)*wavevec*x1) + wan1(xi);
    end
end

%normalize Wannier function
wannorm1 = dx*sum(abs(wan1).^2);
wan1 = wan1/sqrt(wannorm1);

%plot Wannier function
figure(1);
plot(x/(lambda/2),real(wan1),’-k’,’linewidth’,3);
title (’Wannier Function’);
xlabel(’x/a’);
ylabel(’w(x)’);
```

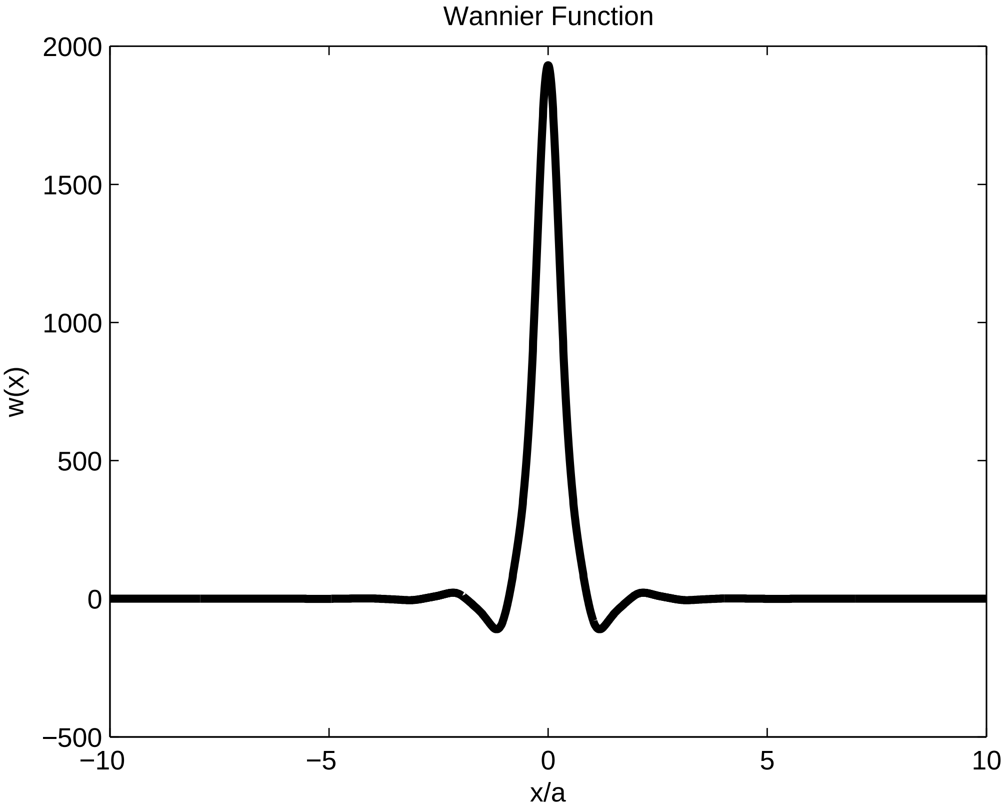

Figure B-1: Wannier function for lattice spacing 532 nm and lattice depth $3E_{\mathrm{R}}$. The x-axis is in units of the lattice spacing.

Appendix C

Bragg Scattering as a Probe of Atomic Wave Functions and Quantum Phase Transitions in Optical Lattices

This appendix contains a reprint of Ref. [77]: Hirokazu Miyake, Georgios A. Siviloglou, Graciana Puentes, David E. Pritchard, Wolfgang Ketterle, and David M. Weld, *Bragg Scattering as a Probe of Atomic Wave Functions and Quantum Phase Transitions in Optical Lattices*, Phys. Rev. Lett. **107**, 175302 (2011).

Bragg Scattering as a Probe of Atomic Wave Functions and Quantum Phase Transitions in Optical Lattices

Hirokazu Miyake, Georgios A. Siviloglou, Graciana Puentes, David E. Pritchard, Wolfgang Ketterle, and David M. Weld*

MIT-Harvard Center for Ultracold Atoms, Research Laboratory of Electronics, and Department of Physics, Massachusetts Institute of Technology, Cambridge, Massachusetts 02139, USA

(Received 26 August 2011; published 21 October 2011)

We have observed Bragg scattering of photons from quantum degenerate ^{87}Rb atoms in a three-dimensional optical lattice. Bragg scattered light directly probes the microscopic crystal structure and atomic wave function whose position and momentum width is Heisenberg limited. The spatial coherence of the wave function leads to revivals in the Bragg scattered light due to the atomic Talbot effect. The decay of revivals across the superfluid to Mott insulator transition indicates the loss of superfluid coherence.

DOI: 10.1103/PhysRevLett.107.175302 PACS numbers: 67.85.−d, 05.30.Rt, 37.10.Jk, 61.05.−a

Ultracold atomic gases are an ideal system in which to study many-body phenomena because of the relative ease with which parameters in the model Hamiltonian can be tuned across a wide range [1,2]. Such studies have resulted in a better understanding of various phase transitions such as the Berezinskii-Kosterlitz-Thouless transition in two-dimensional systems [3], the BEC-BCS crossover of interacting fermions [4], and the superfluid to Mott insulator transition in a three-dimensional lattice [5]. One major goal of this field is to realize spin phases such as antiferromagnetic states to explore quantum magnetism and its interplay with high-temperature superconductivity [6].

Concurrently, there are numerous efforts to develop techniques to probe and understand the atomic ensemble once a new type of ordering is achieved. One recent development is the realization of single-site resolution of atoms in two-dimensional optical lattices [7,8]. An alternative method to measure *in situ* spatial ordering is the technique of Bragg scattering, often used in a condensed matter context to determine crystal structure [9]. In particular, Bragg scattering with neutrons led to the discovery of antiferromagnetism in the solid state [10] and with x rays led to the discovery of the double helix structure of DNA [11].

Bragg scattering relies on the interference of waves scattered coherently from an ensemble of particles. In particular, when atoms are arranged in a periodic pattern in three spatial dimensions, there are certain angles of the incoming and reflected beams where scattering is dramatically enhanced compared to other angles. This has allowed crystallographers to use x rays to determine the properties of crystals such as lattice geometry at the angstrom scale. We have applied this technique to ultracold atoms in a three-dimensional optical lattice by scattering near-infrared light where the atoms are spaced almost 10^4 times farther apart than those in typical condensed matter samples.

Pioneering works on Bragg scattering from cold atoms in optical lattices were done by the Hänsch and Phillips groups by using laser cooled atoms [12]. These lattices were sparsely populated, and the atoms occupied several bands. In this Letter, we have used Bragg scattering to study bosonic atoms cooled to quantum degeneracy and placed in a three-dimensional cubic lattice where the atoms occupy the lowest band. In particular, we have measured directly the Heisenberg-limited width of both the position and momentum of the single ground state atomic wave function in an optical lattice. Furthermore, there is a revival of Bragg scattered light some time after releasing the atoms from the optical lattice, analogous to the optical Talbot effect. This signal gives a direct measure of the coherence of the superfluid component in the lattice.

The experimental apparatus has been described in detail elsewhere [13]. Briefly, laser cooling and evaporative cooling are used to achieve quantum degeneracy of ^{87}Rb atoms in the $|F = 2, m_F = -2\rangle$ state which are loaded into a crossed dipole trap whose trap frequencies range between 30 and 160 Hz. Once quantum degeneracy is achieved, the optical lattices generated by a single 1064 nm fiber laser are adiabatically ramped on. The lattices are calibrated by applying a 12.5 μs pulse and measuring the Kapitza-Dirac diffraction of the atoms and comparing this to theory. The system typically contains about 10^5 atoms, which leads to up to 5 atoms per lattice site. The Bragg reflected light is detected on a CCD camera which images along a direction which satisfies the Bragg condition.

The Bragg scattering condition for a three-dimensional cubic lattice is given by $2d\sin\theta = n\lambda_p$, where d is the spacing between lattice planes, θ is the angle between the incoming beam and the lattice planes, n is any positive integer, and λ_p is the wavelength of the probe beam. For our experiment λ_p is 780 nm and d is 532 nm. With these conditions, the only allowed angle θ is 47° where n is one and corresponds to Bragg reflection off the [1 0 0] plane or any equivalent plane. A schematic of the probe beam with respect to the atoms is shown in the inset in Fig. 1. Since the full angular width of the Bragg scattered light is small (measured to be 4.1 ± 0.4°), a precise alignment of the incident beam had to be performed at the 1/ min repetition rate of the experiment. In contrast, in one and two dimensions, diffractive light scattering occurs at any angle of incidence, as recently shown with atoms in a two-dimensional optical lattice [14].

The probe beam at the Bragg angle had a typical power of 0.3 mW and beam diameter of 300 μm, large enough to illuminate the entire atomic cloud, and was detuned from the $5^2S_{1/2}$, $F = 2 \rightarrow 5^2P_{3/2}$, $F' = 3$ cycling transition of ^{87}Rb by a few natural linewidths, where the natural linewidth Γ is 6 MHz. The detuning needs to be sufficient so that the light traverses the entire atom cloud. Although the absolute signal varies with the detuning, the conclusions reached in this Letter appear not to depend strongly on the amplitude or sign of the detuning. The probe beam was applied for a few microseconds, enough to obtain a signal but short enough to avoid heating effects.

As the lattice is increased, the Bragg reflected signal increases as expected from the crystal ordering and tighter localization of the atoms (Fig. 1). For these data, the lattice in the z direction, which is also the direction of gravity, was ramped to $15E_\text{R}$, where $E_\text{R} = h^2/(2m\lambda_L^2)$ is the recoil energy, h is the Planck constant, m is the mass of ^{87}Rb, and $\lambda_L = 1064$ nm is the lattice laser wavelength. Simultaneously, the lattices in the horizontal directions were ramped to various lattice depths. Note that for our geometry the Bragg reflected intensity is insensitive to the lattice depth in the z direction, because Bragg scattering occurs only in the horizontal xy plane, as we discuss later.

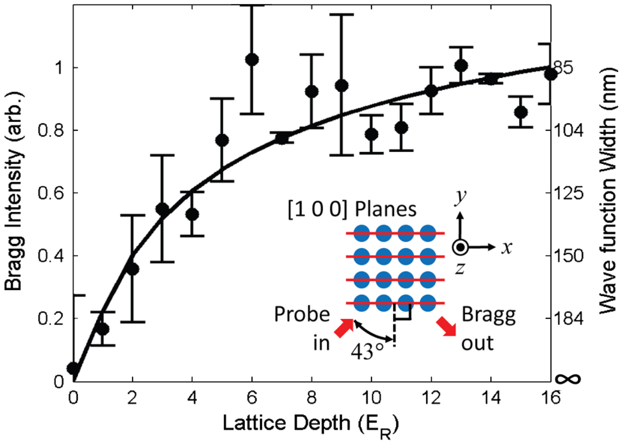

FIG. 1 (color online). Bragg scattering as a probe of the spatial wave function width. Bragg scattered intensity vs lattice depth in units of the recoil energy. The right axis gives the corresponding root-mean-square width of the wave function squared. The solid line is a no-free-parameter curve given by the Debye-Waller factor. Error bars are statistical. The inset is a schematic of the setup for Bragg scattering.

The scattering of light by a collection of atoms can be modeled in the following way. In the limit of low probe intensity and low optical density of the cloud, the Born approximation can be used. Then the scattering cross section $d\sigma/d\Omega$ can be written as a product of one-dimensional Debye-Waller factors where $d\sigma/d\Omega \propto \prod_i \exp[-(\Delta r_i)^2 K_i^2/2]$, where $i = x, y, z$ is the index for the three dimensions, K_i is the magnitude of the ith component of $\mathbf{K}$, where $\mathbf{K} = \mathbf{k}_\text{in} - \mathbf{k}_\text{out}$ is the difference between the incoming probe beam and Bragg scattered wave vectors, and $\Delta r_i = \sqrt{\hbar/(m\omega_i)}$ is the harmonic oscillator width, where $\hbar$ is the reduced Planck constant and ω_i is the trap frequency in the ith direction, which depends on the optical lattice depth. The atoms are approximated as Gaussian wave functions, which is a good approximation for sufficiently large lattice depths. However, we find that, even for low lattice depths where significant superfluid components are expected, this approximation describes the Bragg scattered signal well.

For our experimental conditions, $K_z = 0$ because Bragg scattering occurs in the horizontal xy plane. The lattice depths are controlled in a way such that they are the same in both the x and y directions which leads to $\Delta x \equiv \Delta r_x = \Delta r_y$. This simplifies the scattering cross section to $d\sigma/d\Omega \propto \exp[-(\Delta x)^2 K^2/2]$. Thus Bragg scattering allows the study of the spatial extent of the atomic wave function.

The data can be compared to a no-free-parameter theoretical line, assuming noninteracting atoms. The Bragg scattered intensity $B(N_L)$ as a function of lattice depth N_L is proportional to $\exp[-\lambda_L^2 K^2/(8\pi^2\sqrt{N_L})]$. Both the harmonic oscillator width Δx, which depends on the mass of the rubidium atom and trap frequency, and change in wave vector K are known. This theoretical line and the data are shown in Fig. 1, and we see good agreement. Thus the Bragg scattered light as a function of lattice depth can be well described by a model where the atoms are assumed to be noninteracting Gaussian atomic wave functions whose spatial width is determined by the lattice depth.

Bragg scattering can also be used to probe the momentum width of the atomic wave functions. This is done by measuring Bragg reflection as a function of the expansion time of the atoms between a rapid lattice turn-off and Bragg probe. In particular, the two horizontal lattices were turned off from $15E_\text{R}$ to $0E_\text{R}$ in less than 1 μs, and the lattice in the z direction was kept at $15E_\text{R}$. Turning off the lattices allows the atomic wave packets in each individual lattice well to expand freely in those directions. The data in Fig. 2 show that the signal has decayed in 30 μs. The time it takes to lose crystal structure is roughly the time it takes for the atoms to move over half of a lattice distance.

The Debye-Waller factor can be used to determine more precisely how the Bragg reflection should behave as a function of the expansion time with no free parameters,

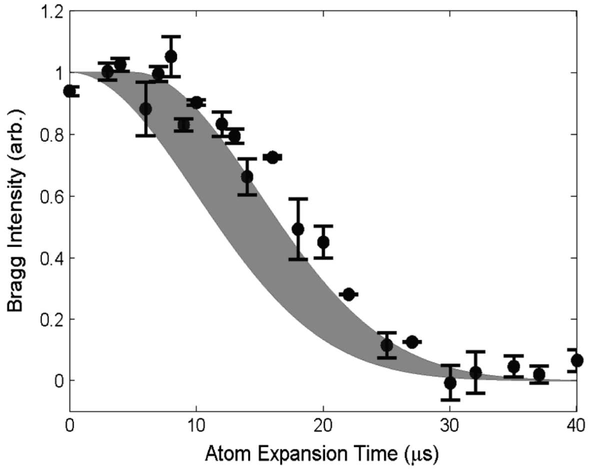

FIG. 2. Bragg scattering as a probe of the momentum wave function width. Bragg scattered intensity vs the free-expansion time of the atoms after rapidly turning off the lattices from $15E_R$. The decay in signal indicates a melting of the crystal structure or, in other words, spreading of the atomic wave packet with a given momentum uncertainty. The gray area is a no-free-parameter curve using the Debye-Waller factor taking into account the probe pulse duration of 5 μs. Error bars are statistical.

assuming Gaussian atomic wave packets. This makes use of the well-known time-dependent behavior of a Heisenberg-limited Gaussian wave packet in free space which can be written as $[\Delta x(t)]^2 = (\Delta x)^2 + (\Delta p)^2 t^2/m^2$, where Δx and Δp are the uncertainty of position and momentum, respectively, at the initial time and t is the expansion time [15]. In a previous paper where the atoms were not quantum degenerate, the momentum distribution was assumed to be determined by temperature [12]. The results in this Letter show that the momentum uncertainty is Heisenberg limited, meaning $(\Delta x)^2(\Delta p)^2 = \hbar^2/4$, so the Bragg scattered light $B(t)$ as a function of expansion time decays as $\exp[-(\Delta p)^2 K^2 t^2/(2m^2)]$. This curve is also shown in Fig. 2. The curve is broadened by taking into account the probe beam duration, which was 5 μs and shows good agreement with the data. This analysis shows that, by releasing the atoms from a lattice, we can directly probe the *in situ* time evolution of the ground state atomic wave functions with a spatial extent of tens of nanometers. Furthermore, the atomic spatial and momentum widths are seen to be Heisenberg limited.

Coherent many-body nonequilibrium dynamics can also be studied with Bragg scattering after a sudden release of the atoms from the optical lattice in three dimensions. At low lattice depths, the Bragg scattered signal shows revivals as a function of expansion time because of the rephasing of the superfluid atomic wave functions that were originally confined in the lattices. Therefore, these revival signals should give a measure of the superfluid order parameter. Furthermore, the revivals are analogous to the optical Talbot effect, whose atomic version was observed previously for a thermal beam [16] and for a quantum degenerate gas in the temporal domain [17]. Here we observe the atomic Talbot effect for an interacting quantum degenerate gas in a three-dimensional optical lattice. Revivals can be seen in Fig. 3 and become less pronounced as the lattice depth increases.

In particular, the characteristic revival time is determined by $\tau = h/[\hbar^2(2k)^2/(2m)]$ and is 123 μs for our parameters, where $2k$ corresponds to the wave vector of the matter wave. However, with Bragg scattering we expect the first revival at half that time of 61 μs, which is what we observe in Fig. 3. This can be understood by realizing that the atomic wave packets need only travel half the lattice spacing to constructively interfere with the wave packets traveling in the opposite directions from the nearest neighbor sites.

The superfluid coherence as a function of lattice depth can be studied by comparing the Bragg reflected signal when the atoms are in the optical lattice to the signal at the first revival. The revival signal as a function of lattice depth is shown in Fig. 4, where the superfluid to Mott insulator transition is expected to occur around $13E_R$ [5]. In a noninteracting system without any dissipation, one would expect complete revivals. The decrease in revival fraction as the lattice depth increases is consistent with the picture that, as interactions increase, phase fluctuations among neighboring lattice sites increase and, consequently, the superfluid fraction decreases. In the Mott insulating phase, revivals should completely disappear, except for a very

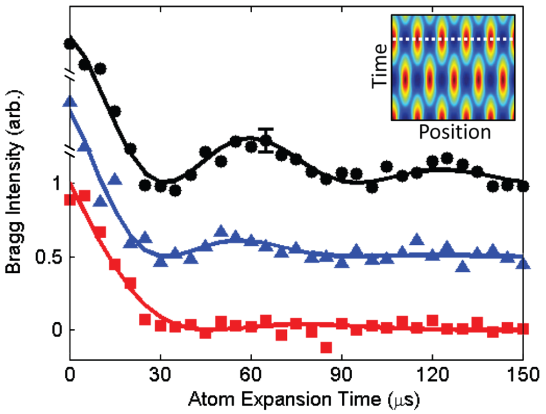

FIG. 3 (color online). Revivals of Bragg scattered light. Bragg scattered intensity vs the expansion time in three dimensions for three different initial lattice depths: $5E_R$ (circles), $8E_R$ (triangles), and $15E_R$ (squares). Each data set is normalized to the Bragg intensity at the initial time. Revivals at lower lattice depths indicate coherence of the atoms across multiple lattice sites. The lines are phenomenological fits to exponentially decaying sine waves. Different lattice depth data are offset for clarity, and the error bar is representative. The inset is a solution to the one-dimensional Gross-Pitaevskii equation with experimental parameters and an initial state of a chain of Gaussian wave functions, showing the revivals of the density distribution as a function of time. The white dotted line represents the revival time.

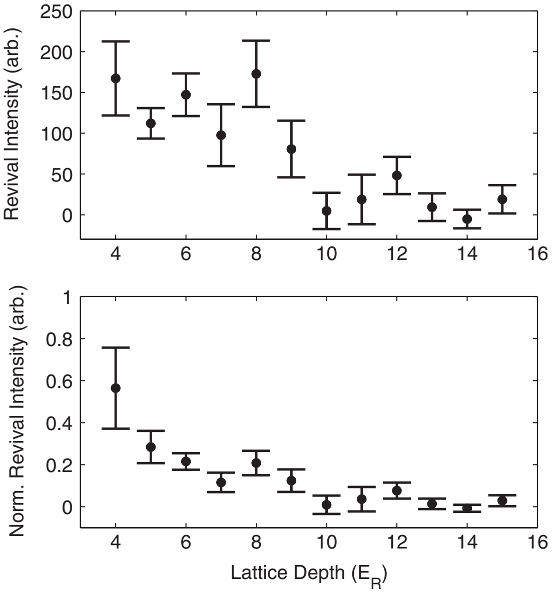

FIG. 4. Bragg scattering revival as a probe of superfluid coherence. Top: Bragg scattered revival signal at 60 μs vs lattice depth. Bottom: The top plot normalized to the Bragg scattered signal without expansion. We see a decrease in revival, and consequently superfluid coherence, as the lattice is increased. Error bars are statistical.

weak signal at intermediate lattice depths due to particle-hole correlations [18].

To understand the measured revival decay, we have numerically studied the one-dimensional Gross-Pitaevskii equation that assumes interacting matter waves at zero temperature. The simulations show that interactions and finite size effects have a negligible effect on the decay of revivals. Empirically, randomizing the phase between neighboring sites reduces the revival fraction. The loss of phase coherence across lattice sites could be due to factors such as temperature, beyond Gross-Pitaevskii equation effects, or technical factors. We have considered quantum depletion [19], but the calculated depletion fraction at $5E_R$ is 2%, too low to account for the observed decay. Future work should provide a more complete picture of the decay of revivals.

Note that Bragg scattered revivals are complementary to the observation of diffraction peaks in time-of-flight absorption images [5]. Both are based on matter-wave interference due to superfluid coherence: revivals at short expansion times and diffraction at long expansion times. Diffraction is a far-field effect possible only for finite size samples, whereas revivals are a near-field bulk effect. The order of the revival or the angular resolution of the diffraction peaks determines whether these techniques probe short-range or long-range spatial coherence. Further studies are needed to determine which technique is more sensitive to certain aspects of the superfluid to Mott insulator transition.

In this Letter, we have not focused on the effects of the occupation number on Bragg scattering. In principle, the atomic wave functions are more extended for higher occupation numbers, but this effect is small for our parameters. However, light scattering at higher occupation numbers will have an inelastic component due to colliding atoms or photoassociation [20]. The dependence of Bragg scattering on lattice depth suggests that these effects are not dominant.

After Bragg scattering has been established as a probe for Mott insulators, it can now be applied to study other types of quantum phases such as antiferromagnetic ordering in both the occupation number and spin sectors [21,22]. Although temperatures required to realize spin ordering are on the order of tens to hundreds of picokelvins, recent experimental results suggest a way forward to lower the temperature of a two-component Mott insulator [23].

In conclusion, we have observed Bragg scattering of near-resonant photons from a quantum degenerate Bose gas in a three-dimensional optical lattice. We have shown that this technique probes not only the periodic structure of the atoms but also the spatial and momentum width of the localized atomic wave functions and the superfluid coherence.

We acknowledge Ian Spielman, Eugene Demler, Igor Mekhov, Jesse Amato-Grill, Niklas Jepsen, and Ivana Dimitrova for fruitful discussions and technical support. We acknowledge Yichao Yu for experimental assistance. We thank Jonathon Gillen for a critical reading of the manuscript. H. M. acknowledges support from the NDSEG program. This work was supported by the NSF through the Center of Ultracold Atoms, by NSF Grant No. PHY-0969731, through an AFOSR MURI program, and under ARO Grant No. W911NF-07-1-0493 with funds from the DARPA OLE program.

---

*Present address: Department of Physics, University of California, Santa Barbara, CA 93106, USA.

[1] M. Lewenstein *et al.*, Adv. Phys. **56**, 243 (2007).
[2] I. Bloch, J. Dalibard, and W. Zwerger, Rev. Mod. Phys. **80**, 885 (2008).
[3] Z. Hadzibabic *et al.*, Nature (London) **441**, 1118 (2006).
[4] M. W. Zwierlein *et al.*, Nature (London) **435**, 1047 (2005).
[5] M. Greiner *et al.*, Nature (London) **415**, 39 (2002).
[6] P. A. Lee, N. Nagaosa, and X.-G. Wen, Rev. Mod. Phys. **78**, 17 (2006).
[7] W. S. Bakr *et al.*, Nature (London) **462**, 74 (2009).
[8] J. F. Sherson *et al.*, Nature (London) **467**, 68 (2010).
[9] N. W. Ashcroft and N. D. Mermin, *Solid State Physics* (Brooks Cole, Belmont, MA, 1976).
[10] C. G. Shull and J. Samuel Smart, Phys. Rev. **76**, 1256 (1949).
[11] J. D. Watson and F. H. C. Crick, Nature (London) **171**, 737 (1953).

[12] M. Weidemüller *et al.*, Phys. Rev. Lett. **75**, 4583 (1995); G. Birkl *et al.*, Phys. Rev. Lett. **75**, 2823 (1995); G. Raithel *et al.*, Phys. Rev. Lett. **78**, 630 (1997); M. Weidemüller, A. Görlitz, T. W. Hänsch, and A. Hemmerich, Phys. Rev. A **58**, 4647 (1998).
[13] E. W. Streed *et al.*, Rev. Sci. Instrum. **77**, 023106 (2006).
[14] C. Weitenberg *et al.*, Phys. Rev. Lett. **106**, 215301 (2011).
[15] L. I. Schiff, *Quantum Mechanics* (McGraw-Hill, New York, 1968).
[16] M. S. Chapman *et al.*, Phys. Rev. A **51**, R14 (1995).
[17] L. Deng *et al.*, Phys. Rev. Lett. **83**, 5407 (1999).
[18] F. Gerbier *et al.*, Phys. Rev. Lett. **95**, 050404 (2005).
[19] K. Xu *et al.*, Phys. Rev. Lett. **96**, 180405 (2006).
[20] A. Gallagher and D. E. Pritchard, Phys. Rev. Lett. **63**, 957 (1989).
[21] T. A. Corcovilos *et al.*, Phys. Rev. A **81**, 013415 (2010).
[22] J. Simon *et al.*, Nature (London) **472**, 307 (2011).
[23] P. Medley *et al.*, Phys. Rev. Lett. **106**, 195301 (2011).

Appendix D

Spin Gradient Demagnetization Cooling of Ultracold Atoms

This appendix contains a reprint of Ref. [76]: Patrick Medley, David M. Weld, Hirokazu Miyake, David E. Pritchard, and Wolfgang Ketterle, *Spin Gradient Demagnetization Cooling of Ultracold Atoms*, Phys. Rev. Lett. **106**, 195301 (2011).

Spin Gradient Demagnetization Cooling of Ultracold Atoms

Patrick Medley,* David M. Weld,† Hirokazu Miyake, David E. Pritchard, and Wolfgang Ketterle
MIT-Harvard Center for Ultracold Atoms, Research Laboratory of Electronics, and Department of Physics, Massachusetts Institute of Technology, Cambridge, Massachusetts 02139, USA

(Received 12 January 2011; revised manuscript received 16 March 2011; published 12 May 2011)

We demonstrate a new cooling method in which a time-varying magnetic field gradient is applied to an ultracold spin mixture. This enables preparation of isolated spin distributions at positive and negative effective spin temperatures of ±50 pK. The spin system can also be used to cool other degrees of freedom, and we have used this coupling to cool an apparently equilibrated Mott insulator of rubidium atoms to 350 pK. These are the lowest temperatures ever measured in any system. The entropy of the spin mixture is in the regime where magnetic ordering is expected.

DOI: 10.1103/PhysRevLett.106.195301 PACS numbers: 67.85.−d, 03.75.Mn, 05.30.Jp, 75.30.Sg

Attainment of lower temperatures has often enabled discovery of new phenomena, from superconductivity to Bose-Einstein condensation. Currently, there is much interest in the possibility of observing correlated magnetic quantum phases in lattice-trapped ultracold atoms [1–3]. The relevant critical temperatures are on the order of 200 pK, lower than any previously achieved temperature [4,5]. Realization of this temperature scale requires the development of new methods of refrigeration which can be applied to ultracold atoms. Many such techniques have been proposed [6–13] but await experimental realization. The cooling method we demonstrate here opens up a previously inaccessible temperature regime and provides a realistic path to the observation of magnetic quantum phase transitions in optical lattices.

The new cooling method is applied to an optically trapped cloud of cold atoms in a mixture of two internal states with different magnetic moments [14]. Application of a strong magnetic field gradient results in almost complete spatial segregation of the two spin components. The "mixed region" of spins between the pure-spin domains has a width which is proportional to the temperature T and inversely proportional to the applied gradient. Reducing the gradient mixes the two components, and due to the mixing entropy the temperature is dramatically reduced. Since Mott insulators can be prepared with an entropy per particle much lower than $k_B \ln 2$, our scheme is a practical way of creating a low entropy mixture in the regime where magnetic ordering is expected. This cooling scheme introduces several new concepts. It implements demagnetization cooling with spin transport instead of spin flips, allows decoupling of the spin and kinetic temperatures, and enables the realization of negative spin temperatures. Long tunneling times in the lattice allow two different implementations of our cooling scheme.

When the gradient is changed faster than the spin relaxation rate, the spin system is effectively isolated from all other degrees of freedom, and very low spin temperatures can be achieved. Contrastingly, when the gradient is changed slowly enough, the spin system is fully equilibrated and can absorb entropy from other degrees of freedom, cooling the whole sample. As shown in Fig. 1, reduction of the gradient after (before) the optical lattice has been raised realizes the regime of isolated (equilibrated) spins.

First, we discuss isolated spins, of which atoms in a Mott insulating state are an almost ideal realization. Spin distributions relax by two atoms exchanging sites through a second-order tunneling process. The time scale of this relaxation is typically 1 s, and the gradient can easily be varied much faster. The equilibrium spin distribution depends only on the ratio of the applied gradient $\nabla|\mathbf{B}|$ and temperature T. When $\nabla|\mathbf{B}|$ is changed, the effective temperature of the decoupled spin degrees of freedom (spin temperature) is rescaled proportionally. This enables the realization of spin distributions with a very low positive (or, if the sign of the gradient is changed, negative) effective temperature. Negative temperatures can occur only for systems with an upper bound on the energy and correspond

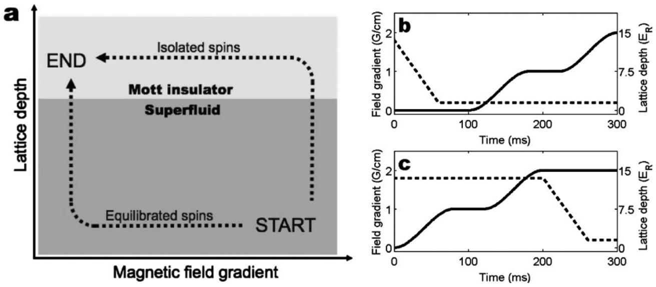

FIG. 1. Two different cooling protocols realizing the cases of isolated and equilibrated spin systems. (a) Experimental "phase diagram" of lattice depth vs applied gradient. Dashed lines show two different paths which connect the high-gradient superfluid state and the low-gradient Mott insulating state. (b) and (c) show the lattice depth (solid line) and gradient strength (dashed line) vs time for the two cases (equilibrated spins and isolated spins, respectively) in (a). The shape of the lattice ramp-up is designed to ensure maximum equilibration.

to an inverted Boltzmann distribution with the largest population in the highest-energy state [15].

Figure 2 shows the results of experiments on *isolated* spins. Fits to data on equilibrated spins indicate an initial temperature of 6.3 nK (see Figs. 3 and 4). While reduction of the gradient by a factor of 1000 would be expected to reduce the effective temperature of the isolated spins to 6.3 pK, our finite optical resolution allows us only to assert an upper bound of 50 ± 20 pK. We have held the spins for up to several seconds in the lattice. No heating is observed during a 1-s hold, but after 3 s the 50 pK distribution is observed to heat to about 70 pK. Similarly, at small negative gradients, we observe a negative-temperature distribution with a temperature closer to zero than -50 ± 20 pK. Since the total energy is monotonic in $-1/T$, these are among the most extreme thermodynamic states ever measured in any system [16,17]. Very low condensate release energies (not temperatures) have been observed previously [18]. Note that the spin temperatures we report are much lower than those attainable by magnetic trapping or optically pumping a system into a single spin state: Even for a fractional population of 10^{-6} in other spin states caused by imperfect pumping or spin-flip collisions [19], the spin temperature in a bias field of 100 mG is 500 nK, assuming a magnetic moment of one Bohr magneton. In our experiment, the energy scale is set by the product of the Bohr magneton with the magnetic field *gradient* and the lattice spacing, and it is the relative ease of achieving very small values of this parameter (corresponding to μ_B times a field of less than 1 μG) which allows us to reach such low spin temperatures.

The mixed-spin region comprises a spectrum of spin excitations, the energy of which can be tuned by adjusting the strength of the gradient [20]. A spin excitation consists of a spin-up atom swapping places with a spin-down atom on the other side of the zero-temperature spin domain boundary. Reduction of the gradient reduces the energy of spin excitations. In the regime of *equilibrated* spins, this causes entropy to flow into the mixed-spin region from other degrees of freedom. This lowers the temperature of the whole system in a manner locally analogous to standard single-shot adiabatic demagnetization refrigeration [21,22]. The kinetic excitations of a trapped Mott insulator are particle-hole excitations [4,23]. On a microscopic level, particle-hole excitations can couple directly to spin excitations if a particle and a hole on opposite sides of the spin domain boundary annihilate. Energy may be absorbed by quasiparticles in the first band or by the spin excitations themselves [24]. In the superfluid phase and during lattice ramp-up, the kinetic excitations are different and entropy transfer is expected to occur faster and in more complex ways. Experimentally, it is easier to maintain adiabaticity if most of the path along which the gradient is changed is in a regime of fast relaxation times [e.g., the lower path in Fig. 1(a)]. Thermodynamically, this adiabatic cooling method is a redistribution of entropy from the kinetic degrees of freedom to the entropy which results from partially mixing the two initially segregated spin domains.

It is easily possible for the mixed region to absorb nearly all of the entropy of the system. In a one-component harmonically trapped Mott insulator which is at a temperature low enough for the particle-hole approximation to hold, the approximate total entropy is $k_B \ln(2)$ times the volume of the "shells" between the Mott plateaus [4]. The maximum entropy of the mixed region is realized when, at low gradient, it is broadened to a substantial fraction of the total size. In that situation, the entropy per site approaches $k_B \ln(n+1)$, where n is the local number of indistinguishable bosons per site (in our samples, n varies across the trap

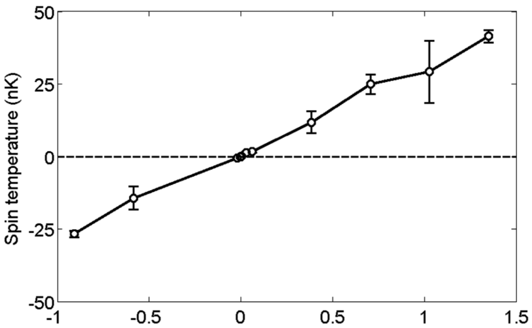

FIG. 2. Preparation of low positive and negative spin temperatures. Measured spin temperature vs final gradient, for the case of isolated spins. Error bars are statistical.

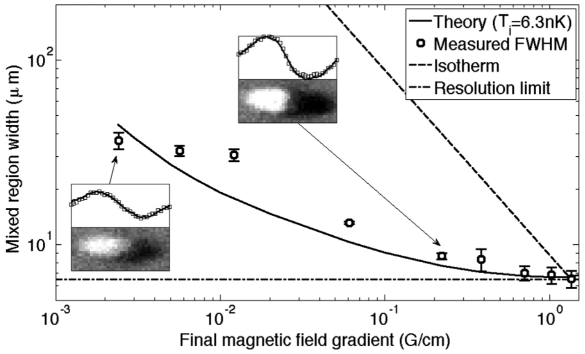

FIG. 3. Entropy transfer from other degrees of freedom to the spin system. Circles represent measured width of the mixed region vs final magnetic field gradient, for the "equilibrated spins" protocol (see Fig. 1). Error bars are statistical. The dashed line represents the expected behavior assuming no cooling. The dash-dotted line shows the minimum resolvable width. The solid curve is the theoretical prediction, assuming an initial temperature of 6.3 nK and including the effects of optical resolution (see Ref. [25] for details). Insets show spin images at the indicated points, the corresponding vertically integrated spin profiles (squares), and the fit to the expected form of a tanh function times the overall density distribution (solid line; see Ref. [20] for details). Axis units and gray scales in the two insets are arbitrary but identical.

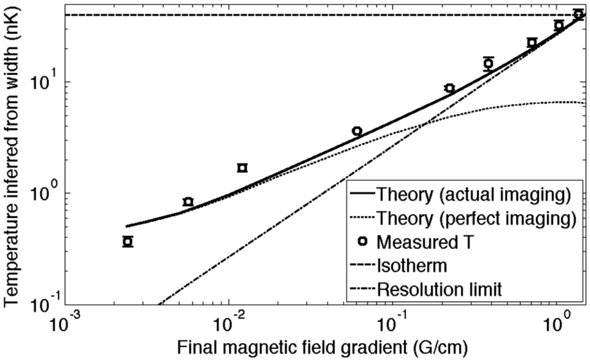

FIG. 4. Spin gradient demagnetization cooling. Circles represent measured temperature vs final magnetic field gradient, for the equilibrated spins protocol (see Fig. 1). Error bars are statistical. These measurements are the same as those shown in Fig. 3. The dashed line follows the isothermal trajectory, and the dash-dotted line shows the resolution limit. The solid line is the theoretical prediction, assuming an initial temperature of 6.3 nK and including the effects of optical resolution. The dotted line is the theoretical prediction *without* the effects of optical resolution.

between 1 and 3). The *maximum* entropy of the spin system is thus larger than the entropy of the kinetic degrees of freedom. Thus, substantial cooling of the system can be achieved with a single gradient demagnetization ramp. We have made a more quantitative analysis of spin gradient demagnetization by calculating entropy-versus-temperature curves of our system in various field gradients [25]. The results confirm the qualitative argument above and show that spin gradient demagnetization cooling is capable of cooling well below the expected Curie temperature.

Figures 3 and 4 show the results of spin gradient demagnetization cooling experiments. As the gradient is reduced, the width of the domain wall increases (see Fig. 3), indicating transfer of entropy from the kinetic degrees of freedom to the spins. The width increases much less steeply than would be expected for an isothermal sample, implying cooling. The observed domain wall width can be converted to a temperature using spin gradient thermometry. The measured temperature falls rapidly as the gradient is lowered (see Fig. 4). The lowest measured temperature is 350 ± 50 pK, making this the coldest implementation of the atomic Mott insulator. An important goal for future experiments will be to develop an additional method of thermometry to measure the temperature of the kinetic degrees of freedom at this very low temperature scale (for progress towards this goal, see Refs. [26–28]). This temperature is colder than the lowest temperature ever measured in an equilibrated kinetic system [29], and it is within a factor of 2 of the expected magnetic ordering temperature [5].

Theoretical curves in Figs. 3 and 4 (see also Ref. [25]) show reasonable agreement with the data. These curves were fitted to the measured temperatures by using only one free parameter: the initial temperature at the maximum gradient. The initial temperature inferred from this fit is 6.3 nK. In our earlier work on thermometry [20], where the lowest measured temperature was 1 nK, some adiabatic demagnetization cooling may have occurred during the preparation of the system. The flattening out observed in the measured data at low gradients could be a signal that all *accessible* entropy has been pumped into the spin system.

There are both practical and theoretical limits on the temperatures which can be attained with spin gradient demagnetization cooling. In traditional magnetic refrigeration experiments, the minimum temperature is often set by the minimum achievable magnetic field or the presence of internal fields in the refrigerant [30]. Analogues of both these limits are relevant here. Practically, the ratio between the highest and lowest attainable magnetic field gradients is an upper bound on the ratio between the initial and final temperatures. In our experiment, the maximum value of $\nabla|\mathbf{B}_i|/\nabla|\mathbf{B}_f|$ is about 1000 (limited mainly by the accuracy of determining the zero crossing of the gradient), which would give a minimum temperature below 10 pK. Another limit stems from the small difference between the interspin interaction energy $U_{\uparrow\downarrow}$ and the mean of the intraspin interaction energies $(U_{\uparrow\uparrow} + U_{\downarrow\downarrow})/2$. For ^{87}Rb, this limit is not expected to preclude cooling below the expected magnetic ordering temperature [25]. The fundamental limit is set by the total entropy of the system. A single Mott insulator has an entropy per particle much less than $k_B \ln 2$. At high gradient, the spin entropy is negligible. Lowering the gradient provides a controlled way of creating a completely mixed two-component system at the same entropy which is low enough for spin ordering to occur. This technique thus provides a specific and realistic method of realizing magnetic phase transitions in optical lattices.

Our scheme differs from single-shot adiabatic demagnetization refrigeration (including that demonstrated in a gas of chromium atoms [31]) in that the magnetic field is replaced by a magnetic field gradient and spin-flip collisions by spin transport. The chromium scheme cannot be applied to alkali atoms due to the much slower spin-flip rates, and extending it from microkelvins to picokelvins would require submicrogauss magnetic field control. In previous work [20], we suggested that adiabatic reduction of the gradient could be used for cooling, and some aspects of this proposal have recently been theoretically addressed and verified [32].

The concept behind spin gradient demagnetization cooling is compelling; if adiabaticity can be maintained, then strong cooling in a lattice will occur. Our experimental implementation was designed to allow the system to equilibrate as much as possible at low lattice depths. We have tested reversibility by replacing the single gradient ramp by a sequence of ramp down, ramp up, ramp down. This led to no detectable difference in the final measured temperature. This indicates that the gradient ramps are adiabatic. Equilibration in the Mott insulator is more difficult to demonstrate, although the previously demonstrated agreement between spin gradient thermometry and cloud size thermometry at high temperatures [20] indicates that the kinetic and spin degrees of freedom are equilibrated in that regime. The fact that the spin distribution fits well to the form expected of an equilibrated spin system is also evidence for equilibration, as is the one-parameter fit to our theoretical predictions (which assume adiabaticity). However, if the lattice is deepened, then lowered to zero, and then raised again, heating is generally observed. Thus, we cannot rule out the existence of long-lived metastable excitations in the Mott insulating state which do not couple to the spin degrees of freedom and thus do not influence our temperature measurement. Other experiments have seen evidence of long equilibration times in the Mott insulator [24,33]. For quicker equilibration, spin gradient demagnetization cooling could be implemented with lighter atomic species (e.g., ^{7}Li or ^{4}He*) and/or shorter period optical lattices.

The cooling technique using isolated spins presented here has achieved spin temperatures and entropies well below the critical values for magnetic ordering, and spin gradient demagnetization cooling of equilibrated spins has cooled to a point within reach of the critical values. This work thus opens a realistic path towards observation of superexchange-driven phase transitions in optical lattices and extends the potential of ultracold atoms trapped in optical lattices to be used as flexible quantum simulators of strongly interacting many-body systems.

We acknowledge discussions with Eugene Demler, Takuya Kitagawa, David Pekker, and Aditi Mitra. We thank Aviv Keshet for a critical reading of the manuscript. H. M. acknowledges support from the NDSEG program. This work was supported by the NSF, through a MURI program, and under ARO Grant No. W911NF-07-1-0493 with funds from the DARPA OLE program.

---

[*] Present address: Department of Physics, Stanford University, Stanford, CA 94305, USA.

[†] dweld@mit.edu

[1] M. Lewenstein *et al.*, Adv. Phys. **56**, 243 (2007).

[2] I. Bloch, J. Dalibard, and W. Zwerger, Rev. Mod. Phys. **80**, 885 (2008).

[3] L.-M. Duan, E. Demler, and M. D. Lukin, Phys. Rev. Lett. **91**, 090402 (2003).

[4] T.-L. Ho and Q. Zhou, Phys. Rev. Lett. **99**, 120404 (2007).

[5] B. Capogrosso-Sansone, Ş. G. Söyler, N. V. Prokof'ev, and B. V. Svistunov, Phys. Rev. A **81**, 053622 (2010).

[6] F. Werner, O. Parcollet, A. Georges, and S. R. Hassan, Phys. Rev. Lett. **95**, 056401 (2005).

[7] M. Popp, J.-J. Garcia-Ripoll, K. G. Vollbrecht, and J. I. Cirac, Phys. Rev. A **74**, 013622 (2006).

[8] B. Capogrosso-Sansone, Ş. G. Söyler, N. Prokof'ev, and B. Svistunov, Phys. Rev. A **77**, 015602 (2008).

[9] P. Rabl, A. J. Daley, P. O. Fedichev, J. I. Cirac, and P. Zoller, Phys. Rev. Lett. **91**, 110403 (2003).

[10] J.-S. Bernier *et al.*, Phys. Rev. A **79**, 061601 (2009).

[11] T.-L. Ho and Q. Zhou, Proc. Natl. Acad. Sci. U.S.A. **106**, 6916 (2009).

[12] T.-L. Ho and Q. Zhou, arXiv:0911.5506.

[13] J. Catani *et al.*, Phys. Rev. Lett. **103**, 140401 (2009).

[14] See supplemental material at http://link.aps.org/supplemental/10.1103/PhysRevLett.106.195301 for detailed experimental methods.

[15] F. Reif, *Fundamentals of Statistical and Thermal Physics* (McGraw-Hill, New York, 1965).

[16] P. J. Hakonen, R. T. Vuorinen, and J. E. Martikainen, Phys. Rev. Lett. **70**, 2818 (1993).

[17] J. T. Tuoriniemi *et al.*, Phys. Rev. Lett. **84**, 370 (2000).

[18] T. Kraemer *et al.*, Appl. Phys. B **79**, 1013 (2004).

[19] A part-per-million spin impurity level would, for example, be present in a 100 Hz magnetic trap with a 100-s lifetime due to dipolar relaxation.

[20] D. M. Weld *et al.*, Phys. Rev. Lett. **103**, 245301 (2009).

[21] W. F. Giauque, J. Am. Chem. Soc. **49**, 1864 (1927).

[22] P. Debye, Ann. Phys. (Leipzig) **386**, 1154 (1926).

[23] F. Gerbier, Phys. Rev. Lett. **99**, 120405 (2007).

[24] R. Sensarma *et al.*, Phys. Rev. B **82**, 224302 (2010).

[25] D. M. Weld, H. Miyake, P. Medley, D. E. Pritchard, and W. Ketterle, Phys. Rev. A **82**, 051603(R) (2010).

[26] W. S. Bakr *et al.*, Science **329**, 547 (2010).

[27] J. F. Sherson *et al.*, Nature (London) **467**, 68 (2010).

[28] N. Gemelke, X. Zhang, C.-L. Hung, and C. Chin, Nature (London) **460**, 995 (2009).

[29] A. E. Leanhardt *et al.*, Science **301**, 1513 (2003).

[30] A. S. Oja and O. V. Lounasmaa, Rev. Mod. Phys. **69**, 1 (1997).

[31] M. Fattori *et al.*, Nature Phys. **2**, 765 (2006).

[32] S. S. Natu and E. J. Mueller, Phys. Rev. A **82**, 013612 (2010).

[33] C.-L. Hung, X. Zhang, N. Gemelke, and C. Chin, Phys. Rev. Lett. **104**, 160403 (2010).

Appendix E

Thermometry and refrigeration in a two-component Mott insulator of ultracold atoms

This appendix contains a reprint of Ref. [116]: David M. Weld, Hirokazu Miyake, Patrick Medley, David E. Pritchard, and Wolfgang Ketterle, *Thermometry and refrigeration in a two-component Mott insulator of ultracold atoms*, Phys. Rev. A **82**, 051603(R) (2010).

PHYSICAL REVIEW A **82**, 051603(R) (2010)

Thermometry and refrigeration in a two-component Mott insulator of ultracold atoms

David M. Weld,[*] Hirokazu Miyake, Patrick Medley,[†] David E. Pritchard, and Wolfgang Ketterle
MIT-Harvard Center for Ultracold Atoms, Research Laboratory of Electronics, and Department of Physics,
Massachusetts Institute of Technology, Cambridge, Massachusetts 02139, USA

(Received 1 September 2010; published 18 November 2010)

Interesting spin Hamiltonians can be realized with ultracold atoms in a two-component Mott insulator (2CMI) [Adv. Phys. **56**, 243 (2007); Rev. Mod. Phys. **80**, 885 (2008)]. It was recently demonstrated that the application of a magnetic field gradient to the 2CMI enables new techniques of thermometry [Phys. Rev. Lett. **103**, 245301 (2009)] and adiabatic cooling [e-print arXiv:1006.4674]. Here we present a theoretical description which provides quantitative analysis of these two techniques. We show that adiabatic reduction of the field gradient is capable of cooling below the Curie or Néel temperature of certain spin-ordered phases.

DOI: 10.1103/PhysRevA.82.051603 PACS number(s): 03.75.Mn, 37.10.Jk, 05.30.Jp, 37.10.De

The possibility of using ultracold lattice-trapped gases as general simulators of strongly interacting many-body systems has excited increasing interest in recent years [1–3]. Spin Hamiltonians are a natural candidate for quantum simulation, especially given the relevance of doped antiferromagnetic systems to the important open problem of high-T_c superconductivity [4]. The 2CMI is the starting point for the simulation of electronic spin systems in lattices [5–9]. Spin-exchange-stabilized magnetically ordered states are expected to exist in the 2CMI [10], and observation of these states and transitions between them would open up an exciting new field at the intersection of atomic and condensed matter physics. The main obstacle which has so far prevented the observation of spin-ordered states in the 2CMI is the very low temperature scale required for spin ordering [11]. Quantum Monte Carlo calculations have predicted Curie and Néel temperatures on the order of 200 pK for the ferromagnetic and antiferromagnetic states of ^{87}Rb in a 532-nm lattice [12]. This is a lower temperature than has ever been measured in any system. Clearly, new methods of thermometry and refrigeration are required.

The recently demonstrated technique of spin gradient thermometry [13] should allow measurement of temperatures down to the spin exchange scale in the 2CMI. The related method of spin gradient demagnetization cooling is capable of cooling to the neighborhood of the critical temperature for spin ordering [14]. Together, these new techniques open a realistic prospect of preparing spin-ordered phases in the 2CMI. In order to compare experimental results with theory, we have developed a simple theoretical model of the 2CMI and used it to calculate the expected response of our system to spin gradient thermometry and spin gradient demagnetization cooling.

Our treatment of the 2CMI is similar in approach to the studies of cooling in the one-component Mott insulator presented in Refs. [11] and [15] in that it is based on calculations of entropy-versus-temperature curves for various values of control parameters. Our model neglects the effects of tunneling and treats each lattice site separately, yet is capable of qualitatively reproducing observed cooling curves using only one fit parameter (the initial temperature) [14]. Our results thus complement, and are in qualitative agreement with, the classical mean-field and Monte Carlo analysis of Natu and Mueller [16].

The inputs to the calculation are the measured trap frequencies ($\omega_x, \omega_y, \omega_z$), the total atom number N, and the applied magnetic field gradient $\nabla|\mathbf{B}|$ (along with various fixed parameters like the scattering lengths and magnetic moment of the atoms and the lattice constant). This allows direct comparison with experiment. The particular trap frequencies assumed here are $2\pi \times (40,156,141)$ Hz. We assume an atom number of 17 000, leading to an occupation number of 3 in the center of the cloud. These values were chosen because they are typical in our experiments. The scattering lengths we assumed are $a_{\uparrow\uparrow} = 100.4a_0$, $a_{\downarrow\downarrow} = 98.98a_0$, and $a_{\uparrow\downarrow} = 98.98a_0$, where a_0 is the Bohr radius and states $\uparrow$ and $\downarrow$ are the $|F = 1, m_F = -1\rangle$ and $|F = 2, m_F = -2\rangle$ hyperfine states of ^{87}Rb; these values represent the results of the most recent theoretical calculations available [17].

Detailed technical descriptions of spin gradient thermometry and spin gradient demagnetization cooling are presented in Refs. [13] and [14], respectively. Both techniques are based on the 2CMI in a magnetic field gradient. Since the two components have different magnetic moments, the gradient pulls them toward opposite sides of the trap, creating two spin domains which remain in thermal contact. At zero temperature, there will be a zero-width boundary between the two domains, but at finite temperature a mixed region composed of spin excitations will be present.

Since the total magnetization is always chosen to be zero, the average value of the magnetic field is canceled by a Lagrange multiplier and can be subtracted from the real field $\mathbf{B}(x)$. This allows us to write the field as $B_{\text{eff}} = \nabla|\mathbf{B}| \cdot \boldsymbol{x}_i$, where $\boldsymbol{x}_i$ is the vector from the trap center to lattice site i projected along the direction of the magnetic field gradient. Note that $B_{\text{eff}} = 0$ at the trap center. If tunneling is neglected, then, at a magnetic field gradient $\nabla|\mathbf{B}|$, the energy of a configuration with $n_\uparrow$ up spins and $n_\downarrow$ down spins at lattice site i is

$$\begin{aligned} E_i(n_\uparrow, n_\downarrow, \nabla|\mathbf{B}|) = {} & p\nabla|\mathbf{B}| \cdot \boldsymbol{x}_i (n_\uparrow - n_\downarrow) \\ & + \frac{1}{2}\sum_\sigma U_{\sigma\sigma} n_\sigma (n_\sigma - 1) + U_{\uparrow\downarrow} n_\uparrow n_\downarrow \\ & + V_i (n_\uparrow + n_\downarrow) - \mu_\uparrow n_\uparrow - \mu_\downarrow n_\downarrow, \end{aligned} \quad (1)$$

---

[*] dweld@mit.edu

[†] Present address: Department of Physics, Stanford University, Stanford, CA 94305, USA.

where p is the amplitude of the effective magnetic moment of the atoms, $x_i = |\boldsymbol{x}_i|$, $\sigma = \{\uparrow,\downarrow\}$, U_{ab} is the interaction energy between spin a and spin b, $V_i = (m/2)(\omega_x^2 x_i^2 + \omega_y^2 y_i^2 + \omega_z^2 z_i^2)$ is the optical trapping potential at site i, y_i and z_i are the distances of site i from the trap center in the two directions transverse to the gradient, and μ_a is the chemical potential of spin a. The chemical potential is set by the requirement that the number of atoms of each spin be equal to half the total experimentally measured number.

Equation (1) can be used in the grand canonical ensemble to infer the thermal probability of different occupation numbers of the two spins. The partition function at lattice site i is $Z_i(\nabla|\mathbf{B}|) = \sum_{\{n_\uparrow,n_\downarrow\}} \exp[-E_i(n_\uparrow,n_\downarrow,\nabla|\mathbf{B}|)/k_B T]$, where k_B is Boltzmann's constant, T is the temperature, and the summation is over all possible combinations of $n_\uparrow$ and $n_\downarrow$ (each combination is counted only once, due to indistinguishability of the atoms). The probability of having $n_\uparrow$ up spins and $n_\downarrow$ down spins at lattice site i is then

$$p_i(n_\uparrow,n_\downarrow,\nabla|\mathbf{B}|,T) = \frac{\exp[-E_i(n_\uparrow,n_\downarrow,\nabla|\mathbf{B}|)/k_B T]}{Z_i}, \qquad (2)$$

and the resulting entropy at site i is

$$S_i(\nabla|\mathbf{B}|,T) = -\sum_{\{n_\uparrow,n_\downarrow\}} p_i \ln p_i, \qquad (3)$$

where the summation is performed in the same way as for the partition function. The only additional approximation needed is a truncation of the sums over spin configurations. For our experimental parameters, configurations corresponding to a total atom number per site n greater than 4 can be neglected, and we have truncated the sums accordingly. This truncation is reminiscent of, but more general than, the particle-hole approximation [11,15]. The site entropy S_i of Eq. (3) is summed over all lattice sites to extract the total entropy as a function of temperature and field gradient. From this output one can extract column-integrated images (Fig. 1), entropy-versus-temperature curves (Fig. 2), and the predicted response to thermometry (Fig. 3) and cooling (Fig. 4).

It is instructive to compare the results of this calculation to those of the simple approximation which treats

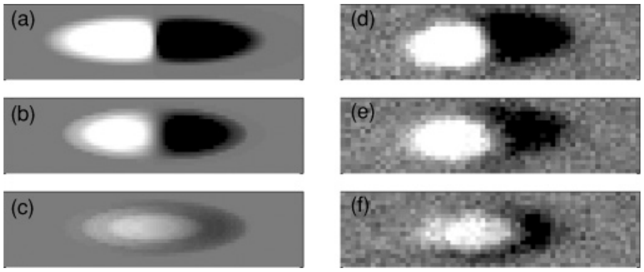

FIG. 1. Comparison of simulated and measured spin images. Simulated images are on the left. Magnetic field gradients and temperatures for simulated images are: (a) 0.7 G/cm and 6 nK, (b) 0.06 G/cm and 2 nK, and (c) 0.0024 G/cm and 0.4 nK. The gradient and fitted temperature for each measured spin image (d)–(f) are similar to the values for the simulated image in the same row. See Fig. 3 for a comparison of the temperature extracted from this fit to the real modeled temperature. Note that the total magnetization in all pictures is close to zero.

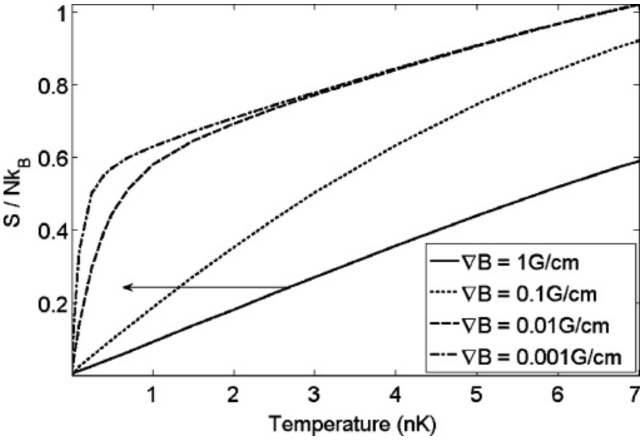

FIG. 2. Total entropy per particle versus temperature, at various gradients, for the experimental parameters described in the text. The arrow indicates a possible path followed during adiabatic spin gradient demagnetization cooling.

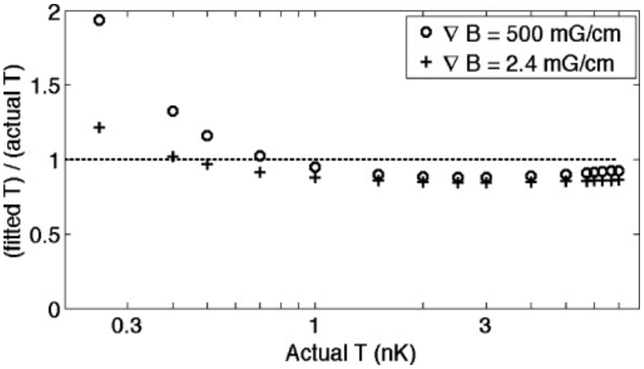

FIG. 3. Ratio between fitted temperature and actual temperature at two different gradients, assuming perfect imaging. This shows the effect of corrections due to indistinguishability and unequal scattering lengths. Finite imaging resolution will limit the range of temperature that can be measured with any given gradient, as discussed in Ref. [13].

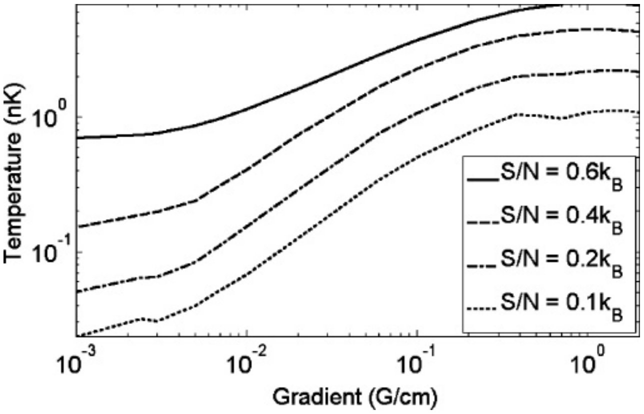

FIG. 4. Spin gradient demagnetization cooling. Predicted temperature versus final gradient, for several values of the total entropy.

the spin and particle-hole degrees of freedom separately. In this approximation, the partition function for an individual lattice site i is assumed to factorize as $Z = Z_\sigma Z_0$, where $Z_\sigma = \sum_\sigma \exp[-\beta \boldsymbol{p}_\sigma \cdot \mathbf{B}(x_i)]$, β is $1/k_B T$, $\boldsymbol{p}_\sigma$ is the magnetic moment of the spin σ, and Z_0 is the partition function of the particle-hole degrees of freedom (for which see [11,15]). This simple treatment is valid for the case of one atom per lattice site. For occupation number $n > 1$, there are corrections which are captured by our more complete model. The first correction arises from a difference ΔU between the mean of the intraspin interaction energies $\overline{U_\sigma}$ and the interspin interaction energy $U_{\uparrow\downarrow}$. $\Delta U/\overline{U_\sigma}$ is about 0.007 for our states. The leading correction changes the magnetic field gradient at the center of the sample B' to an effective gradient $B'[1 + (n-1)\Delta U/k_B T]$. This becomes important at low temperatures, and destroys the factorizability of the partition function mentioned above. The second correction is due to indistinguishability of the atoms. This arises from the quantum mechanical fact that there are three (rather than four) possible spin states for a lattice site with two pseudospin-1/2 atoms. The size of both corrections is expected to be small, but in order to treat them fully we have developed the more general model described above.

Under the assumption that $Z = Z_\sigma Z_0$, the mean spin $\langle s \rangle$ as a function of position, field gradient, and temperature has the simple form

$$\langle s \rangle = \tanh[-\beta \Delta \boldsymbol{p} \cdot \mathbf{B}(x_i)/2], \tag{4}$$

where $\Delta \boldsymbol{p}$ is the difference between the magnetic moments of the two states. Spin gradient thermometry is based on the fact that, at finite temperatures, the width of the boundary layer is proportional to the temperature and inversely proportional to the magnetic field gradient.

The spin profile of Eq. (4) is exact for a 2CMI with one particle per site. The model presented here can be used to investigate corrections to thermometry at higher filling. Figure 3 shows the temperature measured by fitting to Eq. (4) divided by the actual modeled temperature for two values of the gradient. The high-temperature correction is mainly due to indistinguishability of the atoms, and is only important for sites containing 2 or more atoms. Note that the fitted spin profile is integrated along both directions transverse to the gradient, so it includes contributions from all occupation-number domains. Although this correction is conceptually important, it changes the measured temperature by less than 15% under our experimental conditions. The correction at low temperatures is partly due to the fact that the scattering lengths $U_{\uparrow\uparrow}$, $U_{\downarrow\downarrow}$, and $U_{\uparrow\downarrow}$ are not all equal. This is expected to result in a curvature of the mixed region between the two spin domains. This curvature arises from a buoyancy effect—the species with greater intraspin repulsion will preferentially populate the outer regions of the trap. This effect causes a fit to Eq. (4) to overestimate the temperature, since a curved boundary appears wider after integration along the directions perpendicular to the gradient. Another correction at low temperatures arises if the width of the mixed region becomes much less than one lattice constant. In this case both the model and the real physical spin system will not respond measurably to small changes in the gradient, and the measured temperature will overestimate the real temperature. These corrections need to be taken into account for precision temperature measurements at extreme temperatures and field gradients, but they do not alter the conclusions of Refs. [13] or [14].

Spin gradient demagnetization cooling is based on the fact that the entropy stored in the mixed region between the two spin domains increases with decreasing magnetic field gradient. If the change of the gradient is adiabatic, then the energy and entropy which flow to the spin degrees of freedom must come from other degrees of freedom, and the sample's temperature can be reduced. Although spin gradient demagnetization cooling was inspired by (and is locally similar to) adiabatic demagnetization refrigeration in condensed or gaseous systems [18–20], there are important differences between the techniques. Most notably, spin gradient demagnetization cooling varies a magnetic field gradient rather than a homogeneous field, and relies on spin transport rather than spin flips. These differences allow the technique to be applied to lattice-trapped ultracold atomic systems. Spin gradient demagnetization cooling thus broadens and extends existing magnetic refrigeration techniques.

Entropy versus temperature curves such as those plotted in Fig. 2 can be used to calculate the response of the system to spin gradient demagnetization cooling. If the gradient is reduced perfectly adiabatically, the system will move horizontally as indicated by the arrow in Fig. 2, and the temperature will decrease. This behavior is plotted in Fig. 4 for several values of the total entropy (corresponding to different initial temperatures). These predictions can be used directly to fit experimental data, with the initial temperature being the only free parameter. Such fitting gives reasonable agreement (see Ref. [14]).

For sufficiently low initial entropy, the spin degrees of freedom will contain all the entropy in the system when the gradient is adiabatically reduced by some factor. Further reduction of the gradient below this point is expected to linearly decrease the temperature of the system until the point where interactions become important. Conversely, if the initial entropy is too high, the spins will become fully disordered at some finite value of the gradient and will no longer be able to absorb entropy. Reduction of the gradient below this point will not change the temperature. This behavior, which is essentially a finite-size effect, is apparent in the upper curve in Fig. 4. If the gradient is sufficiently high, it can pull the two spin domains so far apart that the area where they overlap is decreased in size. This effect reduces the entropy capacity of the spin degrees of freedom at high gradients, and is the origin of the slight downturn in temperatures at the highest gradients in Fig. 4.

Magnetic field gradients of 1 mG/cm are well within the range of the experimentally achievable. Assuming reduction of the gradient from 2 G/cm to 1 mG/cm, our analysis predicts that samples with an initial entropy lower than about $0.4k_B$ can be cooled below the spin-ordering temperature. Our model neglects spin correlations, so the lowest-temperature results plotted in Fig. 4 should be taken as evidence that reduction of the gradient is capable of cooling below the spin-ordering temperature rather than a prediction of the dependence of temperature on gradient below the Curie or Nèel temperature.

Figure 5 shows several images of the total entropy distribution at different final gradients during demagnetization.

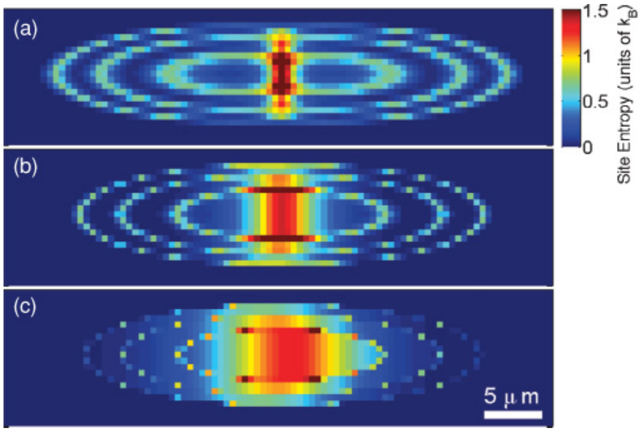

FIG. 5. (Color online) Entropy distribution during spin gradient demagnetization cooling. The images are slices of the cloud through the center. Each pixel represents one lattice site. All plots are at a total entropy per particle near $0.3k_B$, and are thus representative of the changing entropy distribution during isentropic demagnetization. Values of the gradient and temperature are as follows: (a) $\nabla B = 0.5$ G/cm and $T = 3$ nK, (b) $\nabla B = 0.1$ G/cm and $T = 1.5$ nK, (c) $\nabla B = 0.02$ G/cm and $T = 0.5$ nK. The ring-shaped structures are the mixed-occupation-number regions between Mott domains which carry particle-hole entropy. Note that these regions are narrower after reduction of the gradient. This indicates that entropy has been transferred from the mixed-occupation-number regions to the mixed-spin region, and the temperature has been reduced.

The pumping of entropy from the kinetic degrees of freedom to the spins is clearly visible.

These theoretical results help elucidate some limitations on and possible extensions to the technique of spin gradient demagnetization cooling. The technique clearly requires the use of two states with different magnetic moments—this excludes, for example, the two lowest states of ^{7}Li at very high fields. The predicted behavior is also, in principle, different for higher filling factors than it is for $n = 1$ (although, as discussed above, we find this effect to be small for the particular case of ^{87}Rb). For example, strong miscibility or immiscibility of the two species would change the response of the system to demagnetization, but only if the maximum occupation number n is greater than 1 (see also Ref. [21]). The dependence of the response to demagnetization on the trap frequencies and total atom number can also be investigated using the techniques presented here; the most important effect of varying these parameters is generally to change the maximum occupation number and the spectrum of particle-hole excitations. For best cooling performance, the initial entropy should be lower than the maximum mixing entropy ($k_B \ln 2$ per site for the $n = 1$ case). We believe that spin gradient demagnetization cooling could, in principle, be applied to fermionic mixtures as well. In fact, the technique does not even require a lattice, and could potentially be applied to the thermal fraction of a trapped two-component gas.

We have presented results of calculations based on a theoretical model of the 2CMI and its response to a varying magnetic field gradient. Our results provide quantitative support for spin gradient thermometry and spin gradient demagnetization cooling.

We thank Eugene Demler, Takuya Kitagawa, David Pekker, and Servaas Kokkelmans for useful and interesting discussions. H.M. acknowledges support from the NDSEG fellowship program. This work was supported by the NSF, through a MURI program, and under ARO Grant No. W911NF-07-1-0493 with funds from the DARPA OLE program. Correspondence and requests for materials should be addressed to D.M.W.

---

[1] R. Feynman, Int. J. Theor. Phys. **21**, 467 (1982).
[2] M. Lewenstein *et al.*, Adv. Phys. **56**, 243 (2007).
[3] I. Bloch, J. Dalibard, and W. Zwerger, Rev. Mod. Phys. **80**, 885 (2008).
[4] P. A. Lee, N. Nagaosa, and X.-G. Wen, Rev. Mod. Phys. **78**, 17 (2006).
[5] J. Catani, L. De Sarlo, G. Barontini, F. Minardi, and M. Inguscio, Phys. Rev. A **77**, 011603 (2008).
[6] U. Schneider *et al.*, Science **322**, 1520 (2008).
[7] R. Jordens, N. Strohmaier, K. Gunter, H. Moritz, and T. Esslinger, Nature (London) **455**, 204 (2008).
[8] B. Gadway, D. Pertot, R. Reimann, and D. Schneble, Phys. Rev. Lett. **105**, 045303 (2010).
[9] S. Ospelkaus *et al.*, Phys. Rev. Lett. **96**, 180403 (2006).
[10] L.-M. Duan, E. Demler, and M. D. Lukin, Phys. Rev. Lett. **91**, 090402 (2003).
[11] T.-L. Ho and Q. Zhou, Phys. Rev. Lett. **99**, 120404 (2007).
[12] B. Capogrosso-Sansone, Ş. G. Söyler, N. V. Prokof'ev, and B. V. Svistunov, Phys. Rev. A **81**, 053622 (2010).
[13] D. M. Weld *et al.*, Phys. Rev. Lett. **103**, 245301 (2009).
[14] P. Medley, D. M. Weld, H. Miyake, D. E. Pritchard, and W. Ketterle, e-print arXiv:1006.4674.
[15] F. Gerbier, Phys. Rev. Lett. **99**, 120405 (2007).
[16] S. S. Natu and E. J. Mueller, e-print arXiv:1005.3090.
[17] S. Kokkelmans (private communication).
[18] W. F. Giauque, J. Am. Chem. Soc. **49**, 1864 (1927).
[19] P. Debye, Ann. Phys. **386**, 1154 (1926).
[20] M. Fattori *et al.*, Nat. Phys. **2**, 765 (2006).
[21] E. Altman, W. Hofstetter, E. Demler, and M. Lukin, New J. Phys. **5**, 113 (2003).

Appendix F

Spin Gradient Thermometry for Ultracold Atoms in Optical Lattices

This appendix contains a reprint of Ref. [115]: David M. Weld, Patrick Medley, Hirokazu Miyake, David Hucul, David E. Pritchard, and Wolfgang Ketterle, *Spin Gradient Thermometry for Ultracold Atoms in Optical Lattices*, Phys. Rev. Lett. **103**, 245301 (2009).

Selected for a Viewpoint in *Physics*

Spin Gradient Thermometry for Ultracold Atoms in Optical Lattices

David M. Weld, Patrick Medley, Hirokazu Miyake, David Hucul, David E. Pritchard, and Wolfgang Ketterle
MIT-Harvard Center for Ultracold Atoms, Research Laboratory of Electronics, and Department of Physics, Massachusetts Institute of Technology, Cambridge, Massachusetts 02139, USA

(Received 20 August 2009; revised manuscript received 10 October 2009; published 7 December 2009)

We demonstrate spin gradient thermometry, a new general method of measuring the temperature of ultracold atoms in optical lattices. We realize a mixture of spins separated by a magnetic field gradient. Measurement of the width of the transition layer between the two spin domains serves as a new method of thermometry which is observed to work over a broad range of lattice depths and temperatures, including in the Mott insulator regime. We demonstrate the thermometry using ultracold rubidium atoms, and suggest that interesting spin physics can be realized in this system. The lowest measured temperature is 1 nK, indicating that the system has reached the quantum regime, where insulating shells are separated by superfluid layers.

DOI: 10.1103/PhysRevLett.103.245301 PACS numbers: 67.85.−d, 03.75.Mn, 05.30.Jp, 75.10.Jm

Ultracold atoms trapped in optical lattices represent a new frontier for the investigation of many-body physics [1,2]. The existence of novel physics at decreasing energy scales drives the quest for lower temperatures in the atomic Mott insulator. Insulating Mott shells form at a temperature $T \sim 0.2U$, where U is the interaction energy. At the lower temperature $T \sim zJ$, where J is the tunneling amplitude and z is the number of nearest neighbors, the conducting layers become superfluid and the system enters a quantum insulator state [3]. At the even colder temperature scale $T \sim J^2/U$, superexchange-stabilized phases can exist in the two-component Mott insulator; this is the regime of quantum magnetism [4]. Various proposals [5,6] have focused on the realization of quantum spin Hamiltonians in this regime. Detection of superexchange-driven phase transitions in these systems remains a major goal of ultracold atomic physics. Perhaps the most important barrier to experimental detection of such a phase transition is the requirement of temperatures well below 1 nK [4]. Additional cooling methods [7–10] will be needed to reach this very interesting temperature scale. However, it is clear that to assess current methods and to validate future cooling techniques, low-temperature thermometry of the Mott insulator is needed.

Thermometry of systems in the Mott insulating state has remained a challenge [3,11–14]. In this Letter, we discuss and demonstrate a simple and direct method of thermometry using a magnetic field gradient which works in the two-component Mott insulator.

The theory behind this method of thermometry is straightforward. The system under consideration is an ensemble of atoms in a mixture of two hyperfine states loaded into a three-dimensional optical lattice in the presence of a weak magnetic field gradient. The two states have different magnetic moments, and are thus pulled towards opposite sides of the trapped sample by the gradient. At zero temperature, the spins will segregate completely, and a sharp domain wall will exist between the two spin domains (a small width due to superexchange coupling is typically negligible). This system has the same bulk physics as the single-component Mott insulator, but includes additional degrees of freedom in the form of spin excitations in the domain wall. At finite temperature, spin excitations will increase the width of the domain wall. This width will depend in a simple way on the field gradient, the differential Zeeman shift, and the temperature, and can thus be used as a thermometer.

For an incoherent mixture of two spins, the partition function for an individual lattice site can be approximately factorized as $Z = Z_\sigma Z_0$, where $Z_\sigma = \sum_\sigma \exp(-\beta \boldsymbol{\mu}_\sigma \cdot \mathbf{B}(x))$, β is $1/k_B T$, $\boldsymbol{\mu}_\sigma$ is the magnetic moment of the spin σ, $\mathbf{B}(x)$ is the spatially varying magnetic field, and Z_0 is the partition function of the particle-hole degrees of freedom (for which see [3]). This approximation is generally valid for the case of one atom per lattice site; for occupation number $n > 1$, it is valid when the mean of the intraspin interaction energies $\bar{U}_\sigma$ is equal to the interspin interaction energy $U_{\uparrow\downarrow}$, which is a good approximation in ^{87}Rb [15]. Since the total magnetization is fixed, the average value of the magnetic field is canceled by the corresponding Lagrange multiplier; we include this in the definition of $\mathbf{B}(x)$. We are free to treat the two states as having pseudospin $+1$ and -1; making that identification, the mean spin $\langle s \rangle$ as a function of position, gradient strength, and temperature has the simple form

$$\langle s \rangle = \tanh(-\beta \cdot \Delta\boldsymbol{\mu} \cdot \mathbf{B}(x)/2), \tag{1}$$

where $\Delta\boldsymbol{\mu}$ is the difference between the magnetic moments of the two states. A fit of the measured spin distribution with a function of this form will give the temperature of the system. When the Zeeman shift due to the magnetic field gradient is a linear function of position, imaging of the spin distribution essentially corresponds to direct imaging of the Boltzmann distribution.

The apparatus used to produce ultracold ^{87}Rb atoms is described in Ref. [16]. After cooling, approximately 10^5 atoms are held in a far-red-detuned crossed optical dipole trap with trap frequencies between 100 and 200 Hz. A three-dimensional cubic optical lattice, formed by three retroreflected beams each of radius ~150 μm, overlaps the trapping region. Since spin gradient thermometry does not depend on the number of atoms per lattice site n, we perform measurements at a range of n values between 1 and 4. The trapping and lattice beams are all derived from one fiber laser, with a wavelength λ of 1064 nm. Magnetic field gradients up to a few G/cm can be applied with external coils, and calibrated using Stern-Gerlach separation of the different spin states after release from the trap. The gradient is applied along the x direction, which is the weakest axis of the crossed dipole trap. Absorptive imaging of the atoms is performed with a camera pointing down along the vertical z axis.

The sequence of steps used to measure temperature is as follows. First, a sample of ^{87}Rb atoms in the $|F = 1, m_F = -1\rangle$ state is prepared by evaporation in the optical trap. Here F and m_F are the quantum numbers for the total spin and its projection on the z axis, respectively. The atoms are then placed into a mixture of the $|1, -1\rangle$ and $|2, -2\rangle$ states by a nonadiabatic magnetic field sweep through the microwave transition between the two states. This pair of states was chosen in order to avoid spin-exchange collisions. A magnetic field gradient of 2 G/cm is applied along the weak axis of the trap and results in additional evaporation, which is intended to remove the entropy created by the state preparation [17]. At this point, the field gradient is changed to the value to be used for measurement; lower gradients are used for lower-temperature measurements to keep the domain wall width larger than the imaging resolution. The optical lattice is then adiabatically ramped up, typically to a depth of $14.5E_R$, where $E_R = h^2/2m\lambda^2$ is the recoil energy and m is the atomic mass. The transition to the Mott insulator occurs at $13.5E_R$. At this point, the spin structure depends on the temperature as discussed above.

There are several ways to measure the resulting spin distribution. One way is to first take an image of the $F = 2$ atoms in the $14.5E_R$ lattice, then in a second run to illuminate the atoms with an optical repumper beam resonant with the $F = 1$ to $F' = 2$ transition for a few μs prior to imaging. This method gives an image of all atoms and an image of just the $F = 2$ atoms; appropriate subtraction can provide the spin distribution. It is possible to determine the temperature from a single image of one spin, but the data in this Letter were all taken using pairs of images to guard against systematic errors.

The temperature can then be measured by fitting the spin distribution to the hyperbolic tangent form. The resulting thermometer has high dynamic range and variable sensitivity, works at all accessible temperatures of interest, and requires only the simplest fitting procedures.

Figure 1 shows data of the type used for spin gradient thermometry. An image of the total atom density and an image of the spin density are obtained as discussed above. Both images are then integrated along the y direction, which is transverse to the gradient. The spin distribution is then fit by a function of the form $\rho(x)\tanh(\frac{3}{4}\beta\mu_B\frac{d|\mathbf{B}|}{dx}x)$, where $\rho(x)$ is the total density distribution. The only free parameters in this fit are a horizontal and vertical offset and the temperature $T = 1/k_B\beta$.

Figures 2 and 3 show the results of this thermometry on ultracold ^{87}Rb atoms in an optical lattice. Figure 2 shows the linear scaling of the inverse width of the domain wall as the magnetic field gradient is varied while holding the temperature constant. For widths larger than the optical resolution, the scaling is as predicted by Eq. (1). The two data sets plotted in Fig. 2 were taken at two different temperatures: 7 and 123 nK, according to the best-fit theoretical lines. Finite optical resolution or motion of the atoms during imaging will blur the measured spin profile and result in an overestimate of the domain wall width at high gradients. This effect was modeled by applying a Gaussian blur of radius 4 μm to the theoretical 7 nK spin profile at various gradients. The resulting curve, plotted as a dash-dotted line in Fig. 2, reproduces the saturation of measured width observed in the experimental data. The effect of finite resolution is always to overestimate the temperature.

Figure 3 shows the measured temperature plotted as a function of the power in the dipole trapping beam which confines the atoms in the direction of the magnetic field gradient (the x direction). Higher powers in this beam lead to less effective evaporation, and thus higher final tempera-

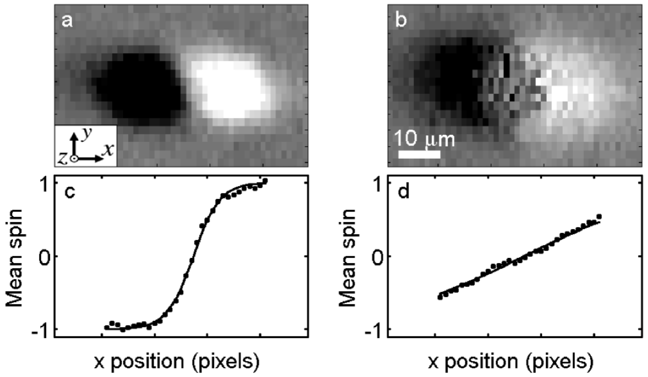

FIG. 1. Images used for spin gradient thermometry. Data on the left were taken at a lower optical trap power than data on the right. Panels (a) and (b) are images of the spin distribution. Panels (c) and (d) show the mean spin versus x position. The fit to (c) gives a temperature of 52 nK; the fit to (d) gives a temperature of 296 nK. The inset of (a) shows the axes referred to in the text. The bar in (b) is a size scale.

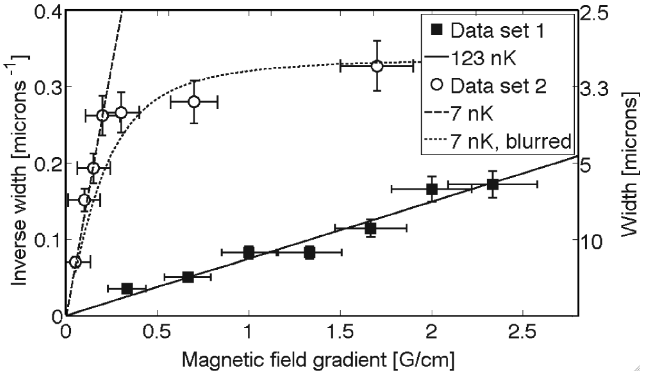

FIG. 2. Independence of the measured temperature on the applied field gradient. The inverse of the width of the spin profile is plotted as a function of magnetic field gradient for two data sets at two different temperatures. For constant temperature, a linear curve is expected. The width is defined as the distance from the center to the position where the mean spin is $1/2$. The solid (dashed) line assumes a temperature of 123 nK (7 nK) and perfect imaging. The measured width of the colder data set saturates at high gradient because of finite imaging resolution. The dotted line assumes a temperature of 7 nK and an imaging resolution of 4 μm.

tures. As a check of the new method of thermometry, Fig. 3 also presents an analysis of the same data using an existing method of thermometry, based on measurement of the in-trap width of the atomic cloud along the direction perpendicular to the gradient. This second method is based on the well-known relation $\sigma^2 = k_B T/m\omega^2$, where σ is the $1/e^2$ half-width of the atomic cloud and ω is the trap frequency in the direction along which the width is measured [12]. The width is determined by a fit to the wings of the trapped cloud. Trap width thermometry is based on a noninteracting approximation, and will fail at temperatures less than U when the system starts to become incompressible. As in Ref. [12], all points on this plot are in the high-temperature single-band regime (T is less than the band gap but greater than the bandwidth). For the temperatures plotted in Fig. 3, the agreement between the two methods is reasonably good, and gives confidence in the use of spin gradient thermometry in regions of parameter space where no other thermometer exists.

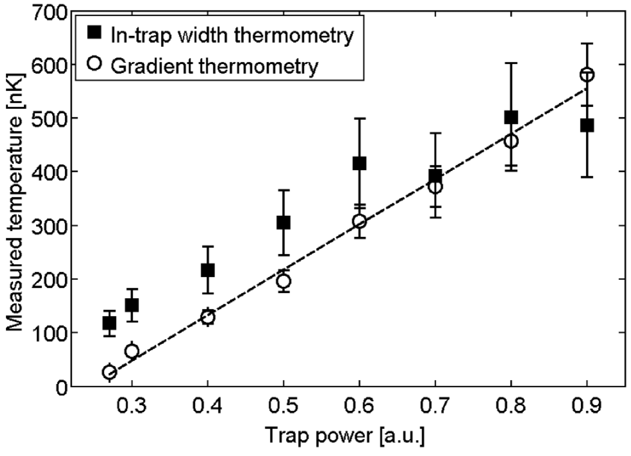

FIG. 3. Validation of spin gradient thermometry. Comparison of two measured temperatures versus final power in one of the optical trapping beams. Squares represent the results of in-trap cloud width thermometry, and circles represent the results of spin gradient thermometry (see text for details). Error bars represent estimated uncertainties. The dashed line is a linear fit to the spin gradient thermometry data. The closeness of this fit suggests that the temperature reached is proportional to the trap depth.

The large dynamic range of spin gradient thermometry is evident in Fig. 3. Thermometry can be performed at temperatures so high that no condensate exists before lattice ramp-up. The lowest temperature we have measured was achieved by using the new thermometry as a feedback signal, enabling adjustment of experimental parameters for optimization of the final temperature in the Mott insulator. This method allowed us to achieve a measured temperature as low as 1 nK. At the lattice depth used here, U is 37 nK, and zJ is 6 nK. The measured temperature is thus well below $T_c = zJ$, the predicted critical temperature for the superfluid layer between the $n = 1$ and $n = 0$ Mott domains. According to the treatment of Ref. [3], at 1 nK the system should be well inside the quantum regime, with concentric quantum insulator shells separated by superfluid layers. This represents the first direct demonstration that this temperature regime has been achieved in the Mott insulator.

At a given value of the magnetic field gradient, very low temperatures will result in a width of the transition region smaller than the imaging optics can resolve (see Fig. 2). However, the width can be increased by decreasing the magnetic field gradient. The lowest measurable temperature will then depend on the minimum achievable gradient as well as the optical resolution, which are technical rather than fundamental limitations. In our apparatus, background gradients with all coils turned off are of order 10^{-3} G/cm, which, given our imaging resolution of a few μm, would in principle allow measurement of temperatures down to $\sim$50 pK or the superexchange scale, whichever is higher.

It is instructive to compare the useful range of this new method of thermometry with that of existing methods. To facilitate meaningful comparison with non-lattice-based methods, we discuss the range of entropy per particle S/Nk_B at which a given thermometer works, rather than the range of temperature. Condensate fraction thermometry works for $0.35 < S/Nk_B < 3.5$, where the lower limit is set by the difficulty of detecting a thermal fraction less than 10%, and the upper limit is set by disappearance of the condensate. Thermometry based on the thermal cloud size has a similar lower bound, but extends to arbitrarily high values of S/Nk_B. Quantitative thermometry based on the visibility of interference peaks upon release from the lattice requires state-of-the-art quantum Monte Carlo calculations fitted to the data. This technique was recently used to measure temperatures as low as $0.08U$ in the superfluid phase near the Mott insulator transition [18]. This method cannot be applied deep in the Mott insulating state [11]. Measurement of the width of the conducting layers between the Mott shells is the only previously proposed method which works directly in the Mott insulating state [3,4,19]. However, this method requires tomographic techniques, and the useful range of entropy is rather narrow: $0.4 < S/Nk_B < \ln(2)$, where the upper limit is set by the melting of the Mott shells, and the lower limit is an estimate based on typical trapping parameters and optical resolution. Counting only spin excitations, the range of *spin* entropy per particle at which spin gradient thermometry works in our system is $0.1 < S_\sigma/Nk_B < \ln(2)$, where the lower limit is a function of optical resolution and sample size and the upper limit corresponds to the point at which the domain wall becomes as wide as the sample. It is important to note that spin gradient thermometry can work even if the entropy of the particle-hole excitations lies outside of this range in either direction. For example, spin gradient thermometry can work at arbitrarily high values of the total entropy per particle S/Nk_B, assuming the field gradient is increased to the point where $S_\sigma/Nk_B < \ln(2)$.

The method of thermometry presented here works because the two-component Mott insulator in a field gradient has a spectrum of soft and easily measurable spin excitations. The wide dynamic range of this method is a result of the fact that, in contrast to the gapped spectrum of the bulk one-component Mott insulator, the energy of the spin excitations can be tuned by adjusting the strength of the magnetic field gradient. The addition of a field gradient and a second spin component does not change the bulk properties of the Mott insulator and can be regarded as "attaching" a general thermometer to the first component.

The two-component Mott insulator in a field gradient is a rich system which can provide experimental access to novel spin physics as well as thermometry. In the work presented here, we have always allowed the spin distribution to equilibrate in the gradient before ramping up the optical lattice. However, changing the gradient after the atoms were already loaded into the lattice should open up several interesting scientific opportunities, in which the gradient is used to manipulate or perturb the atoms rather than as a diagnostic tool. If, for example, the gradient were suddenly changed after lattice ramp-up, one could probe nonequilibrium spin dynamics in a many-body quantum system. If the gradient were instead lowered adiabatically after ramp-up, adiabatic cooling of the Mott insulator could potentially be performed which, in contrast to [20], would not involve spin-flip collisions.

In conclusion, we have proposed and demonstrated a new method of thermometry for ultracold atoms in optical lattices. We have used the new method to measure temperatures in the Mott insulator as low as 1 nK. This temperature is to the best of our knowledge the lowest ever measured in a lattice, and it indicates that the system is deep in the quantum Mott regime.

The authors thank Eugene Demler, Takuya Kitagawa, David Pekker, and Lode Pollet for helpful discussions. This work was supported by the NSF, through a MURI program, and under ARO Grant No. W911NF-07-1-0493 with funds from the DARPA OLE program. H. M. acknowledges support from the NSF.

[1] I. Bloch, J. Dalibard, and W. Zwerger, Rev. Mod. Phys. **80**, 885 (2008).
[2] M. Lewenstein *et al.*, Adv. Phys. **56**, 243 (2007).
[3] F. Gerbier, Phys. Rev. Lett. **99**, 120405 (2007).
[4] T.-L. Ho and Q. Zhou, Phys. Rev. Lett. **99**, 120404 (2007).
[5] L. Duan, E. Demler, and M. Lukin, Phys. Rev. Lett. **91**, 090402 (2003).
[6] E. Altman, W. Hofstetter, E. Demler, and M. Lukin, New J. Phys. **5**, 113 (2003).
[7] M. Popp, J.-J. Garcia-Ripoll, K. G. Vollbrecht, and J. I. Cirac, Phys. Rev. A **74**, 013622 (2006).
[8] P. Rabl, A. J. Daley, P. O. Fedichev, J. I. Cirac, and P. Zoller, Phys. Rev. Lett. **91**, 110403 (2003).
[9] J.-S. Bernier *et al.*, Phys. Rev. A **79**, 061601 (2009).
[10] T.-L. Ho and Q. Zhou, Proc. Natl. Acad. Sci. U.S.A. **106**, 6916 (2009).
[11] L. Pollet, C. Kollath, K. V. Houcke, and M. Troyer, New J. Phys. **10**, 065001 (2008).
[12] D. McKay, M. White, and B. DeMarco, Phys. Rev. A **79**, 063605 (2009).
[13] A. Hoffmann and A. Pelster, Phys. Rev. A **79**, 053623 (2009).
[14] B. Capogrosso-Sansone, E. Kozik, N. Prokof'ev, and B. Svistunov, Phys. Rev. A **75**, 013619 (2007).
[15] For other atomic species, this treatment can readily be extended to include effects of finite $\Delta U = \bar{U}_\sigma - U_{\uparrow\downarrow}$. The leading correction changes the magnetic field gradient at the center of the sample B' to an effective gradient $B'(1 + (n-1)\Delta U/k_B T)$.
[16] E. W. Streed *et al.*, Rev. Sci. Instrum. **77**, 023106 (2006).
[17] C.-L. Hung, X. Zhang, N. Gemelke, and C. Chin, Phys. Rev. A **78**, 011604 (2008).
[18] S. Trotzky *et al.*, arXiv:0905.4882.
[19] S. Fölling, A. Widera, T. Müller, F. Gerbier, and I. Bloch, Phys. Rev. Lett. **97**, 060403 (2006).
[20] M. Fattori *et al.*, Nature Phys. **2**, 765 (2006).

Bibliography

[1] J. R. Abo-Shaeer, C. Raman, J. M. Vogels, and W. Ketterle. Observation of vortex lattices in bose-einstein condensates. *Science*, 292(5516):476–479, 2001.

[2] Y. Aharonov and D. Bohm. Significance of electromagnetic potentials in the quantum theory. *Phys. Rev.*, 115:485–491, Aug 1959.

[3] M. Aidelsburger, M. Atala, S. Nascimbène, S. Trotzky, Y.-A. Chen, and I. Bloch. Experimental realization of strong effective magnetic fields in an optical lattice. *Phys. Rev. Lett.*, 107:255301, Dec 2011.

[4] K. Aikawa, A. Frisch, M. Mark, S. Baier, A. Rietzler, R. Grimm, and F. Ferlaino. Bose-einstein condensation of erbium. *Phys. Rev. Lett.*, 108:210401, May 2012.

[5] A. Alberti, G. Ferrari, V. V. Ivanov, M. L. Chiofalo, and G. M. Tino. Atomic wave packets in amplitude-modulated vertical optical lattices. *New J. Phys.*, 12(6):065037, 2010.

[6] A. Alberti, V. V. Ivanov, G. M. Tino, and G. Ferrari. Engineering the quantum transport of atomic wavefunctions over macroscopic distances. *Nat Phys*, 5:547, August 2009.

[7] M. H. Anderson, J. R. Ensher, M. R. Matthews, C. E. Wieman, and E. A. Cornell. Observation of bose-einstein condensation in a dilute atomic vapor. *Science*, 269(5221):198–201, 1995.

[8] M. R. Andrews, C. G. Townsend, H.-J. Miesner, D. S. Durfee, D. M. Kurn, and W. Ketterle. Observation of interference between two bose condensates. *Science*, 275(5300):637–641, 1997.

[9] N. Ashcroft and N. D. Mermin. *Solid State Physics*. Brooks Cole, Belmont, Massachusetts, 1976.

[10] A. Auerbach. *Interacting Electrons and Quantum Magnetism*. Springer-Verlag, New York City, New York, 1994.

[11] Waseem S. Bakr, Jonathon I. Gillen, Amy Peng, Simon Folling, and Markus Greiner. A quantum gas microscope for detecting single atoms in a hubbard-regime optical lattice. *Nature*, 462:74, November 2009.

[12] G. Birkl, M. Gatzke, I. H. Deutsch, S. L. Rolston, and W. D. Phillips. Bragg scattering from atoms in optical lattices. *Phys. Rev. Lett.*, 75:2823–2826, Oct 1995.

[13] Immanuel Bloch, Jean Dalibard, and Wilhelm Zwerger. Many-body physics with ultracold gases. *Rev. Mod. Phys.*, 80:885–964, Jul 2008.

[14] B. N. Brockhouse. Scattering of neutrons by spin waves in magnetite. *Phys. Rev.*, 106:859–864, Jun 1957.

[15] B. Capogrosso-Sansone, Ş. G. Söyler, N. V. Prokof'ev, and B. V. Svistunov. Critical entropies for magnetic ordering in bosonic mixtures on a lattice. *Phys. Rev. A*, 81:053622, May 2010.

[16] Michael S. Chapman, Christopher R. Ekstrom, Troy D. Hammond, Jörg Schmiedmayer, Bridget E. Tannian, Stefan Wehinger, and David E. Pritchard. Near-field imaging of atom diffraction gratings: The atomic talbot effect. *Phys. Rev. A*, 51:R14–R17, Jan 1995.

[17] Lawrence W. Cheuk, Ariel T. Sommer, Zoran Hadzibabic, Tarik Yefsah, Waseem S. Bakr, and Martin W. Zwierlein. Spin-injection spectroscopy of a spin-orbit coupled fermi gas. *Phys. Rev. Lett.*, 109:095302, Aug 2012.

[18] Adrian Cho. The mad dash to make light crystals. *Science*, 320(5874):312–313, 2008.

[19] Steven Chu, J. E. Bjorkholm, A. Ashkin, and A. Cable. Experimental observation of optically trapped atoms. *Phys. Rev. Lett.*, 57:314–317, Jul 1986.

[20] Leon N. Cooper. Bound electron pairs in a degenerate fermi gas. *Phys. Rev.*, 104:1189–1190, Nov 1956.

[21] T. A. Corcovilos, S. K. Baur, J. M. Hitchcock, E. J. Mueller, and R. G. Hulet. Detecting antiferromagnetism of atoms in an optical lattice via optical bragg scattering. *Phys. Rev. A*, 81:013415, Jan 2010.

[22] Jean Dalibard, Fabrice Gerbier, Gediminas Juzeliūnas, and Patrik Öhberg. *Colloquium*: Artificial gauge potentials for neutral atoms. *Rev. Mod. Phys.*, 83:1523–1543, Nov 2011.

[23] K. B. Davis, M. O. Mewes, M. R. Andrews, N. J. van Druten, D. S. Durfee, D. M. Kurn, and W. Ketterle. Bose-einstein condensation in a gas of sodium atoms. *Phys. Rev. Lett.*, 75:3969–3973, Nov 1995.

[24] J. H. de Boer and E. J. W. Verwey. Semi-conductors with partially and with completely filled 3 d -lattice bands. *Proceedings of the Physical Society*, 49(4S):59, 1937.

[25] Y. N. Martinez de Escobar, P. G. Mickelson, M. Yan, B. J. DeSalvo, S. B. Nagel, and T. C. Killian. Bose-einstein condensation of ^{84}Sr. *Phys. Rev. Lett.*, 103:200402, Nov 2009.

[26] C. R. Dean, L. Wang, P. Maher, C. Forsythe, F. Ghahari, Y. Gao, J. Katoch, M. Ishigami, P. Moon, M. Koshino, T. Taniguchi, K. Watanabe, K. L. Shepard, J. Hone, and P. Kim. Hofstadter's butterfly in moire superlattices: A fractal quantum Hall effect, arXiv:1212.4783 [cond-mat.mes-hall], December 2012.

[27] B. DeMarco and D. S. Jin. Onset of fermi degeneracy in a trapped atomic gas. *Science*, 285(5434):1703–1706, 1999.

[28] L. Deng, E. W. Hagley, J. Denschlag, J. E. Simsarian, Mark Edwards, Charles W. Clark, K. Helmerson, S. L. Rolston, and W. D. Phillips. Temporal, matter-wave-dispersion talbot effect. *Phys. Rev. Lett.*, 83:5407–5411, Dec 1999.

[29] L.-M. Duan, E. Demler, and M. D. Lukin. Controlling spin exchange interactions of ultracold atoms in optical lattices. *Phys. Rev. Lett.*, 91:090402, Aug 2003.

[30] W. Ehrenberg and R. E. Siday. The refractive index in electron optics and the principles of dynamics. *Proc. Phys. Soc. Lond.*, 62(1):8, 1949.

[31] Manuel Endres, Takeshi Fukuhara, David Pekker, Marc Cheneau, Peter Schauß, Christian Gross, Eugene Demler, Stefan Kuhr, and Immanuel Bloch. The 'higgs' amplitude mode at the two-dimensional superfluid/mott insulator transition. *Nature*, 487:454, July 2012.

[32] R. P. Feynman. Simulating physics with computers. *International Journal of Theoretical Physics*, 21:467, 1982.

[33] Matthew P. A. Fisher, Peter B. Weichman, G. Grinstein, and Daniel S. Fisher. Boson localization and the superfluid-insulator transition. *Phys. Rev. B*, 40:546–570, Jul 1989.

[34] Alan Gallagher and David E. Pritchard. Exoergic collisions of cold na*-na. *Phys. Rev. Lett.*, 63:957–960, Aug 1989.

[35] Thomas R. Gentile, Barbara J. Hughey, Daniel Kleppner, and Theodore W. Ducas. Experimental study of one- and two-photon rabi oscillations. *Phys. Rev. A*, 40:5103–5115, Nov 1989.

[36] Fabrice Gerbier. Boson mott insulators at finite temperatures. *Phys. Rev. Lett.*, 99:120405, Sep 2007.

[37] Fabrice Gerbier and Jean Dalibard. Gauge fields for ultracold atoms in optical superlattices. *New Journal of Physics*, 12:033007, March 2010.

[38] Fabrice Gerbier, Artur Widera, Simon Fölling, Olaf Mandel, Tatjana Gericke, and Immanuel Bloch. Phase coherence of an atomic mott insulator. *Phys. Rev. Lett.*, 95:050404, Jul 2005.

[39] Thierry Giamarchi, Christian Ruegg, and Oleg Tchernyshyov. Bose-einstein condensation in magnetic insulators. *Nat Phys*, 4:198, March 2008.

[40] Markus Glück, Andrey R. Kolovsky, and Hans Jürgen Korsch. Wannier-stark resonances in optical and semiconductor superlattices. *Physics Reports*, 366(3):103 – 182, 2002.

[41] A. Görlitz, J. M. Vogels, A. E. Leanhardt, C. Raman, T. L. Gustavson, J. R. Abo-Shaeer, A. P. Chikkatur, S. Gupta, S. Inouye, T. Rosenband, and W. Ketterle. Realization of bose-einstein condensates in lower dimensions. *Phys. Rev. Lett.*, 87:130402, Sep 2001.

[42] Markus Greiner, Olaf Mandel, Tilman Esslinger, Theodor W. Hansch, and Immanuel Bloch. Quantum phase transition from a superfluid to a mott insulator in a gas of ultracold atoms. *Nature*, 415:39, January 2002.

[43] Axel Griesmaier, Jörg Werner, Sven Hensler, Jürgen Stuhler, and Tilman Pfau. Bose-einstein condensation of chromium. *Phys. Rev. Lett.*, 94:160401, Apr 2005.

[44] D. J. Griffiths. *Introduction to Quantum Mechanics*. Pearson Prentice Hall, Upper Saddle River, NJ, 2005.

[45] Milena Grifoni and Peter Hänggi. Driven quantum tunneling. *Physics Reports*, 304(5 - 6):229 – 354, 1998.

[46] Subhadeep Gupta, Aaron E. Leanhardt, Alexander D. Cronin, and David E. Pritchard. Coherent manipulation of atoms with standing light waves. *Comptes Rendus de l'Académie des Sciences - Series IV - Physics*, 2(3):479 – 495, 2001.

[47] Zoran Hadzibabic, Peter Kruger, Marc Cheneau, Baptiste Battelier, and Jean Dalibard. Berezinskii-kosterlitz-thouless crossover in a trapped atomic gas. *Nature*, 441:1118, June 2006.

[48] M. Hafezi, A. S. Sørensen, E. Demler, and M. D. Lukin. Fractional quantum hall effect in optical lattices. *Phys. Rev. A*, 76:023613, Aug 2007.

[49] P. G. Harper. Single band motion of conduction electrons in a uniform magnetic field. *Proc. Phys. Soc. A*, 68:874–878, Oct 1955.

[50] A. C. Hewson. *The Kondo Problem to Heavy Fermions*. Cambridge University Press, Cambridge, England, 1997.

[51] Tin-Lun Ho and Qi Zhou. Intrinsic heating and cooling in adiabatic processes for bosons in optical lattices. *Phys. Rev. Lett.*, 99:120404, Sep 2007.

[52] Douglas R. Hofstadter. Energy levels and wave functions of bloch electrons in rational and irrational magnetic fields. *Phys. Rev. B*, 14:2239–2249, Sep 1976.

[53] J. Hubbard. Electron correlations in narrow energy bands. *Proceedings of the Royal Society of London. Series A. Mathematical and Physical Sciences*, 276(1365):238–257, 1963.

[54] B. Hunt, J. D. Sanchez-Yamagishi, A. F. Young, K. Watanabe, T. Taniguchi, P. Moon, M. Koshino, P. Jarillo-Herrero, and R. C. Ashoori. Massive Dirac fermions and Hofstadter butterfly in a van der Waals heterostructure, arXiv:1303.6942 [cond-mat.mes-hall], March 2013.

[55] S. Inouye, M. R. Andrews, J. Stenger, H.-J. Miesner, D. M. Stamper-Kurn, and W. Ketterle. Observation of feshbach resonances in a bose-einstein condensate. *Nature*, 392:151, March 1998.

[56] V. V. Ivanov, A. Alberti, M. Schioppo, G. Ferrari, M. Artoni, M. L. Chiofalo, and G. M. Tino. Coherent delocalization of atomic wave packets in driven lattice potentials. *Phys. Rev. Lett.*, 100:043602, Jan 2008.

[57] J. D. Jackson. From lorenz to coulomb and other explicit gauge transformations. *American Journal of Physics*, 70(9):917–928, 2002.

[58] D. Jaksch, C. Bruder, J. I. Cirac, C. W. Gardiner, and P. Zoller. Cold bosonic atoms in optical lattices. *Phys. Rev. Lett.*, 81:3108–3111, Oct 1998.

[59] D. Jaksch and P. Zoller. Creation of effective magnetic fields in optical lattices: the hofstadter butterfly for cold neutral atoms. *New J. Phys.*, 5:56, May 2003.

[60] K. Jiménez-García, L. J. LeBlanc, R. A. Williams, M. C. Beeler, A. R. Perry, and I. B. Spielman. Peierls substitution in an engineered lattice potential. *Phys. Rev. Lett.*, 108:225303, May 2012.

[61] Robert Jordens, Niels Strohmaier, Kenneth Gunter, Henning Moritz, and Tilman Esslinger. A mott insulator of fermionic atoms in an optical lattice. *Nature*, 455:204, September 2008.

[62] W Ketterle. Bose-einstein condensation in dilute atomic gases: atomic physics meets condensed matter physics. *Physica B: Condensed Matter*, 280(1-4):11 – 19, 2000.

[63] D. I. Khomskii. *Basic Aspects of the Quantum Theory of Solids.* Cambridge University Press, Cambridge, England, 2010.

[64] A.Yu. Kitaev. Fault-tolerant quantum computation by anyons. *Annals of Physics*, 303(1):2 – 30, 2003.

[65] W. Kohn. Analytic properties of bloch waves and wannier functions. *Phys. Rev.*, 115:809–821, Aug 1959.

[66] Sebastian Kraft, Felix Vogt, Oliver Appel, Fritz Riehle, and Uwe Sterr. Bose-einstein condensation of alkaline earth atoms: ^{40}Ca. *Phys. Rev. Lett.*, 103:130401, Sep 2009.

[67] A. B. Kuklov and B. V. Svistunov. Counterflow superfluidity of two-species ultracold atoms in a commensurate optical lattice. *Phys. Rev. Lett.*, 90:100401, Mar 2003.

[68] R. B. Laughlin. Anomalous quantum hall effect: An incompressible quantum fluid with fractionally charged excitations. *Phys. Rev. Lett.*, 50:1395–1398, May 1983.

[69] Patrick A. Lee, Naoto Nagaosa, and Xiao-Gang Wen. Doping a mott insulator: Physics of high-temperature superconductivity. *Rev. Mod. Phys.*, 78:17–85, Jan 2006.

[70] Maciej Lewenstein, Anna Sanpera, Veronica Ahufinger, Bogdan Damski, Aditi Sen(De), and Ujjwal Sen. Ultracold atomic gases in optical lattices: mimicking condensed matter physics and beyond. *Advances in Physics*, 56(2):243–379, 2007.

[71] H. Lignier, C. Sias, D. Ciampini, Y. Singh, A. Zenesini, O. Morsch, and E. Arimondo. Dynamical control of matter-wave tunneling in periodic potentials. *Phys. Rev. Lett.*, 99:220403, Nov 2007.

[72] Y.-J. Lin, R. L. Compton, K. Jimenez-Garcia, J. V. Porto, and I. B. Spielman. Synthetic magnetic fields for ultracold neutral atoms. *Nature*, 462:628, December 2009.

[73] Mingwu Lu, Nathaniel Q. Burdick, Seo Ho Youn, and Benjamin L. Lev. Strongly dipolar bose-einstein condensate of dysprosium. *Phys. Rev. Lett.*, 107:190401, Oct 2011.

[74] K. W. Madison, F. Chevy, W. Wohlleben, and J. Dalibard. Vortex formation in a stirred bose-einstein condensate. *Phys. Rev. Lett.*, 84:806–809, Jan 2000.

[75] K. W. Madison, M. C. Fischer, R. B. Diener, Qian Niu, and M. G. Raizen. Dynamical bloch band suppression in an optical lattice. *Phys. Rev. Lett.*, 81:5093–5096, Dec 1998.

[76] Patrick Medley, David M. Weld, Hirokazu Miyake, David E. Pritchard, and Wolfgang Ketterle. Spin gradient demagnetization cooling of ultracold atoms. *Phys. Rev. Lett.*, 106:195301, May 2011.

[77] Hirokazu Miyake, Georgios A. Siviloglou, Graciana Puentes, David E. Pritchard, Wolfgang Ketterle, and David M. Weld. Bragg scattering as a probe of atomic wave functions and quantum phase transitions in optical lattices. *Phys. Rev. Lett.*, 107:175302, Oct 2011.

[78] G. Möller and N. R. Cooper. Condensed ground states of frustrated bose-hubbard models. *Phys. Rev. A*, 82:063625, Dec 2010.

[79] N. F. Mott. The basis of the electron theory of metals, with special reference to the transition metals. *Proceedings of the Physical Society. Section A*, 62(7):416, 1949.

[80] Yu. B. Ovchinnikov, J. H. Müller, M. R. Doery, E. J. D. Vredenbregt, K. Helmerson, S. L. Rolston, and W. D. Phillips. Diffraction of a released bose-einstein condensate by a pulsed standing light wave. *Phys. Rev. Lett.*, 83:284–287, Jul 1999.

[81] M. E. Peskin and D. V. Schroeder. *An Introduction to Quantum Field Theory.* Westview Press, 1995.

[82] T. P. Polak and T. A. Zaleski. Time-of-flight patterns of ultracold bosons in optical lattices in various abelian artificial magnetic field gauges. *Phys. Rev. A*, 87:033614, Mar 2013.

[83] Stephen Powell, Ryan Barnett, Rajdeep Sensarma, and Sankar Das Sarma. Bogoliubov theory of interacting bosons on a lattice in a synthetic magnetic field. *Phys. Rev. A*, 83:013612, Jan 2011.

[84] G. Raithel, G. Birkl, A. Kastberg, W. D. Phillips, and S. L. Rolston. Cooling and localization dynamics in optical lattices. *Phys. Rev. Lett.*, 78:630–633, Jan 1997.

[85] Subir Sachdev. Quantum magnetism and criticality. *Nat Phys*, 4:173, March 2008.

[86] J. J. Sakurai. *Modern Quantum Mechanics.* Addison-Wesley Publishing Company, Reading, MA, 1994.

[87] L. I. Schiff. *Quantum Mechanics.* McGraw-Hill, New York, 1968.

[88] U. Schneider, L. Hackermller, S. Will, Th. Best, I. Bloch, T. A. Costi, R. W. Helmes, D. Rasch, and A. Rosch. Metallic and insulating phases of repulsively interacting fermions in a 3d optical lattice. *Science*, 322(5907):1520–1525, 2008.

[89] J. R. Schrieffer and P. A. Wolff. Relation between the anderson and kondo hamiltonians. *Phys. Rev.*, 149:491–492, Sep 1966.

[90] Jacob F. Sherson, Christof Weitenberg, Manuel Endres, Marc Cheneau, Immanuel Bloch, and Stefan Kuhr. Single-atom-resolved fluorescence imaging of an atomic mott insulator. *Nature*, 467:68, September 2010.

[91] C. G. Shull and J. Samuel Smart. Detection of antiferromagnetism by neutron diffraction. *Phys. Rev.*, 76:1256–1257, Oct 1949.

[92] C. Sias, H. Lignier, Y. P. Singh, A. Zenesini, D. Ciampini, O. Morsch, and E. Arimondo. Observation of photon-assisted tunneling in optical lattices. *Phys. Rev. Lett.*, 100:040404, Feb 2008.

[93] Jonathan Simon, Waseem S. Bakr, Ruichao Ma, M. Eric Tai, Philipp M. Preiss, and Markus Greiner. Quantum simulation of antiferromagnetic spin chains in an optical lattice. *Nature*, 472:307, April 2011.

[94] Anders S. Sørensen, Eugene Demler, and Mikhail D. Lukin. Fractional quantum hall states of atoms in optical lattices. *Phys. Rev. Lett.*, 94:086803, Mar 2005.

[95] D. M. Stamper-Kurn, M. R. Andrews, A. P. Chikkatur, S. Inouye, H.-J. Miesner, J. Stenger, and W. Ketterle. Optical confinement of a bose-einstein condensate. *Phys. Rev. Lett.*, 80:2027–2030, Mar 1998.

[96] D. M. Stamper-Kurn, M. R. Andrews, A. P. Chikkatur, S. Inouye, H.-J. Miesner, J. Stenger, and W. Ketterle. Optical confinement of a bose-einstein condensate. *Phys. Rev. Lett.*, 80:2027–2030, Mar 1998.

[97] Daniel A. Steck. “Rubidium 87 D Line Data”, available online at `http://steck.us/alkalidata` (revision 2.1.4, 23 December 2010).

[98] Simon Stellmer, Meng Khoon Tey, Bo Huang, Rudolf Grimm, and Florian Schreck. Bose-einstein condensation of strontium. *Phys. Rev. Lett.*, 103:200401, Nov 2009.

[99] J. Stenger, S. Inouye, D. M. Stamper-Kurn, H.-J. Miesner, A. P. Chikkatur, and W. Ketterle. Spin domains in ground-state bose-einstein condensates. *Nature*, 396:345, November 1998.

[100] Erik W. Streed, Ananth P. Chikkatur, Todd L. Gustavson, Micah Boyd, Yoshio Torii, Dominik Schneble, Gretchen K. Campbell, David E. Pritchard, and Wolfgang Ketterle. Large atom number bose-einstein condensate machines. *Review of Scientific Instruments*, 77(2):023106, 2006.

[101] J. Struck, C. Ölschläger, M. Weinberg, P. Hauke, J. Simonet, A. Eckardt, M. Lewenstein, K. Sengstock, and P. Windpassinger. Tunable gauge potential for neutral and spinless particles in driven optical lattices. *Phys. Rev. Lett.*, 108:225304, May 2012.

[102] Yosuke Takasu, Kenichi Maki, Kaduki Komori, Tetsushi Takano, Kazuhito Honda, Mitsutaka Kumakura, Tsutomu Yabuzaki, and Yoshiro Takahashi. Spin-singlet bose-einstein condensation of two-electron atoms. *Phys. Rev. Lett.*, 91:040404, Jul 2003.

[103] M. G. Tarallo, A. Alberti, N. Poli, M. L. Chiofalo, F.-Y. Wang, and G. M. Tino. Delocalization-enhanced bloch oscillations and driven resonant tunneling in optical lattices for precision force measurements. *Phys. Rev. A*, 86:033615, Sep 2012.

[104] Leticia Tarruell, Daniel Greif, Thomas Uehlinger, Gregor Jotzu, and Tilman Esslinger. Creating, moving and merging dirac points with a fermi gas in a tunable honeycomb lattice. *Nature*, 483:302, March 2012.

[105] D. J. Thouless, M. Kohmoto, M. P. Nightingale, and M. den Nijs. Quantized hall conductance in a two-dimensional periodic potential. *Phys. Rev. Lett.*, 49:405–408, Aug 1982.

[106] S. Trotzky, L. Pollet, F. Gerbier, U. Schnorrberger, I. Bloch, N. V. Prokof/'ev, B. Svistunov, and M. Troyer. Suppression of the critical temperature for superfluidity near the mott transition. *Nat Phys*, 6:998, December 2010.

[107] D. C. Tsui, H. L. Stormer, and A. C. Gossard. Two-dimensional magnetotransport in the extreme quantum limit. *Phys. Rev. Lett.*, 48:1559–1562, May 1982.

[108] D. van Oosten, P. van der Straten, and H. T. C. Stoof. Quantum phases in an optical lattice. *Phys. Rev. A*, 63:053601, Apr 2001.

[109] A. Wachter and H. Hoeber. *Compendium of Theoretical Physics*. Springer, New York, 2006.

[110] Pengjun Wang, Zeng-Qiang Yu, Zhengkun Fu, Jiao Miao, Lianghui Huang, Shijie Chai, Hui Zhai, and Jing Zhang. Spin-orbit coupled degenerate fermi gases. *Phys. Rev. Lett.*, 109:095301, Aug 2012.

[111] J. D. Watson and F. H. C. Crick. Molecular structure of nucleic acids: A structure for deoxyribose nucleic acid. *Nature*, 171:737, April 1953.

[112] Matthias Weidemüller, Axel Görlitz, Theodor W. Hänsch, and Andreas Hemmerich. Local and global properties of light-bound atomic lattices investigated by bragg diffraction. *Phys. Rev. A*, 58:4647–4661, Dec 1998.

[113] Matthias Weidemüller, Andreas Hemmerich, Axel Görlitz, Tilman Esslinger, and Theodor W. Hänsch. Bragg diffraction in an atomic lattice bound by light. *Phys. Rev. Lett.*, 75:4583–4586, Dec 1995.

[114] Christof Weitenberg, Peter Schauß, Takeshi Fukuhara, Marc Cheneau, Manuel Endres, Immanuel Bloch, and Stefan Kuhr. Coherent light scattering from a two-dimensional mott insulator. *Phys. Rev. Lett.*, 106:215301, May 2011.

[115] David M. Weld, Patrick Medley, Hirokazu Miyake, David Hucul, David E. Pritchard, and Wolfgang Ketterle. Spin gradient thermometry for ultracold atoms in optical lattices. *Phys. Rev. Lett.*, 103:245301, Dec 2009.

[116] David M. Weld, Hirokazu Miyake, Patrick Medley, David E. Pritchard, and Wolfgang Ketterle. Thermometry and refrigeration in a two-component mott insulator of ultracold atoms. *Phys. Rev. A*, 82:051603, Nov 2010.

[117] K. C. Wright, R. B. Blakestad, C. J. Lobb, W. D. Phillips, and G. K. Campbell. Driving phase slips in a superfluid atom circuit with a rotating weak link. *Phys. Rev. Lett.*, 110:025302, Jan 2013.

[118] K. Xu, Y. Liu, D. E. Miller, J. K. Chin, W. Setiawan, and W. Ketterle. Observation of strong quantum depletion in a gaseous bose-einstein condensate. *Phys. Rev. Lett.*, 96:180405, May 2006.

[119] Sen Yang, A. T. Hammack, M. M. Fogler, L. V. Butov, and A. C. Gossard. Coherence length of cold exciton gases in coupled quantum wells. *Phys. Rev. Lett.*, 97:187402, Oct 2006.

[120] D. R. Yennie. Integral quantum hall effect for nonspecialists. *Rev. Mod. Phys.*, 59:781–824, Jul 1987.

[121] J. Zak. Magnetic translation group. *Phys. Rev.*, 134:A1602–A1606, Jun 1964.

[122] J. Zak. Magnetic translation group. ii. irreducible representations. *Phys. Rev.*, 134:A1607–A1611, Jun 1964.

[123] M. W. Zwierlein, J. R. Abo-Shaeer, A. Schirotzek, C. H. Schunck, and W. Ketterle. Vortices and superfluidity in a strongly interacting fermi gas. *Nature*, 435:1047, June 2005.